European MSc in
Marine Environment
and Resources
UPV/EHU–SOTON–UB-ULg

Erasmus
Mundus

REF: 2013-0237

MASTER THESIS PROJECT

A case study of sea ice concentration retrieval near Dibble Glacier, East Antarctica:

Contradicting observations between passive microwave remote sensing and optical satellites

BY
LAM Hoi Ming

**August 2016
Bremen, Germany**

université de BORDEAUX

UNIVERSITY OF Southampton

eman ta zabal zazu
Universidad del País Vasco   Euskal Herriko Unibertsitatea

Université de Liège

Dr Manu Soto
as teaching staff of the MER Master of the University of the Basque Country

CERTIFIES:

That the research work entitled "**A case study of sea ice concentration retrieval near Dibble Glacier, East Antarctica: Contradiction between passive microwave remote sensing and optical satellite observations**"

has been carried out by LAM Hoi Ming
in the Institute of Environmental Physics, University of Bremen

under the supervision of Dr Gunnar Spreen
from the of the University of Bremen

in order to achieve 30 ECTS as a part of the MER Master program.

In   September 2016

Signed:

Supervisor

Abstract

In East Antarctica, around 136°E 66°S, spurious appearance of polynya (open water area within an ice pack) is observed on ice concentration maps derived from the ASI (ARTIST Sea Ice) algorithm during the period of February to April 2014, using satellite data from the Advanced Microwave Scanning Radiometer 2 (AMSR-2). This contradicts with the visual images obtained by the Moderate Resolution Imaging Spectroradiometer (MODIS), which show the area to be ice covered during the period. In this study, data of ice concentration, brightness temperature, air temperature, snowfall, bathymetry, and wind in the area were analysed to identify possible explanations for the occurrence of such phenomenon, hereafter referred to as the artefact. We find that the weather filters (Bootstrap filter and GR(36.5/18.7) filter) in the ASI algorithm have caused the error, and surface wetting could be the reason that the results were erroneously interpreted. A method to replace the erroneous pixels at the location with uncorrupted data, created by removing the weather filters at the specific pixels, was implemented. Furthermore, a general method to detect and remove possible erroneous pixels at other locations is proposed.

Resumen

En un región circa de 136°E 66°S en la Antártida Oriental, la apariencia falsa de polynya (zona de aguas abiertas dentro de una bolsa de hielo) que se observa en los mapas de concentración de hielo derivados del algoritmo de ASI (ARTIST Sea Ice) durante el período de febrero al abril de 2014, a partir de datos del satélite del Advanced Microwave Scanning Radiometer 2 (AMSR-2). Esto contradice con las imágenes visuales obtenidos por el Moderate Resolution Imaging Spectroradiometer (MODIS), que muestran que el área es cubierta de hielo durante el período. En este estudio, se analizaron los datos de concentración de hielo, la temperatura de brillo, temperatura del aire, nevadas, batimetría, y el viento de la zona para identificar posibles explicaciones para la aparición de este fenómeno, en lo sucesivo, el artefacto. Nos encontramos con que los filtros de tiempo (filtro Bootstrap y GR(36.5/18.7) filtro) en el algoritmo de ASI han provocado el error, y la humectación de la superficie podría ser la razón de que los filtros se aplican erróneamente. Un método para reemplazar los píxeles erróneos en el lugar con los datos no corrompidos, creado mediante la eliminación de los filtros de tiempo en los píxeles específicos, se implementó. Además, se propone un método general para detectar y eliminar posibles píxeles erróneos en otros lugares.

TABLE OF CONTENTS

1   Introduction

Sea ice plays various roles in local weather events and the global climate system. It acts as a physical barrier between the ocean and the atmosphere, regulating the exchange of heat, mass, and momentum. During winter, when there is a large temperature difference between a cold atmosphere and a relatively warm ocean, heat loss from the ocean over thin ice is one to two orders of magnitude greater than that over thick ice (Maykut, 1978), and the ocean-atmospheric heat exchange is mostly limited to areas of open water and thin ice, often referred to as polynyas, within the ice pack. Polynyas can be categorized by their mechanism of ice removal and by location. A sensible-heat (open-ocean) polynya, often found in mid-ocean areas, could form when there is an upwelling of above-freezing water. Heat transferred from the warmer water body to the ice, providing the heat source for melting the ice and preventing new ice formation. In contrast, a latent-heat (coastal) polynya is located in ocean water at its freezing point. It is formed when there is a wind-driven and/or oceanic current-driven ice divergence from a barrier, such as the coast or an ice shelf. Due to the low water temperature, new ice grows within the polynya, and is carried away by wind and currents. The continuous export of ice keeps the polynya ice-free. In some cases, sensible-heat exchange also occurs at coastal polynyas, when the water temperature is higher than that of the air above. Thus the distribution of polynyas affects the regional heat balance. In particular, coastal polynyas are a major site of ice production, due to the enhanced heat lost in the area. During the formation and growth of sea ice, salt is rejected into the underlying ocean, increasing the salinity and the density of the water body, thereby inducing convection and in some cases the formation of deep water. This convection is an important driver to thermohaline circulation in the ocean. Another notable effect of sea ice is its high albedo relative to water, reflecting a considerable amount of insolation, particularly in summer when solar heating is high. Furthermore, ice monitoring is crucial for marine operations and transport in the polar regions. Accurate ice maps are essential for the safety of ship navigations and offshore operations. Finally, accurate sea ice concentration is required in climate monitoring and modelling. Misclassification of ice as open water, or vice versa, particularly in the marginal ice zone and in polynya regions, would significantly affect estimations of heat balance, ice production, and other air-ice-ocean processes in climate studies.

Remote sensing by satellite is a practical tool for sea ice monitoring. It enables the collection of spatially extensive and temporally continuous data of the polar regions, which is not easily achieved through other means due to the difficulties in reaching these remote locations and in covering such large areas. Surface properties of sea ice are monitored by the numerous sensors on

different satellites and retrieved by algorithm derived by individuals and research groups at various institutes. One of these properties is the ice concentration, which is defined as the relative area covered by ice with respect to some referenced area. The Institute of Environmental Physics at the University of Bremen issues daily sea ice concentration maps of the entire Arctic and Antarctica, together with regional maps at selected locations. It is retrieved by the ARTIST (Arctic Radiation and Turbulence Interaction STudy) Sea Ice (ASI) algorithm, using data from AMSR-2 (Advanced Microwave Scanning Radiometer 2) onboard of the satellite Global Change Observation Mission-Water "Shizuku" (GCOM-W1), and its predecessor AMSR-E (Advanced Microwave Scanning Radiometer for Earth Observing System) onboard of the satellite Aqua.

Contradictions between sea ice concentration maps produced from the ASI algorithm and visual images from the Moderate Resolution Imaging Spectrometer (MODIS) in a region around 136°E 66°S, near the Dibble Iceberg Tongue in East Antarctica, have been noticed by Mr. Neal Young of the Australian Antarctic Division, Department of the Environment and Energy, Australia (Personal communication, February 11, 2014). The observation has motivated this thesis. In the investigated area, fast ice (sea ice that is attached to the shore) usually prevails for several years, while polynyas have been observed within the drifting ice zone. However, the ASI algorithm produced images that show episodes of spurious occurrence of polynya (in this essay referred to as "the artefact") between February and April 2014. This study aims to find out the reasons for the occurrence of such phenomenon, and to provide possible solutions.

Following this introduction, a discussion of the basic physics related to the project is given in Chapter 2, including an brief description of the investigated area (Section 2.1), the principles of passive microwave remote sensing (Section 2.2), the physics of sea ice (Section 2.3) and a discussion on the ASI algorithm used for ice concentration retrieval (Section 2.4). Chapter 3 begins with the motivation of this study (Section 3.1), followed by an introduction to the data used in this study (Section 3.2); an investigation into the artefact using ice concentration (Section 3.3) and environmental parameters (Section 3.4), and a discussion on the investigations (Section 3.5). Chapter 4 provides a solution to mitigate the specific artefact investigated and proposes a more general solution that could prevent similar occurrence of the artefact in other locations (Section 4.1). Further work derived from the investigations in this thesis is also proposed (Section 4.2). Finally, Chapter 5 gives a summary and conclusion to the study.

2   Fundamentals

2.1   Investigated area and its characteristics

This thesis looks into a region at around 136°E 66°S, near the Dibble Iceberg Tongue in East Antarctica (Figure 2.1). From previous observations, fast ice that prevails for several years dominates the region, while polynyas have been observed along the ice edge, within the drifting ice zone.
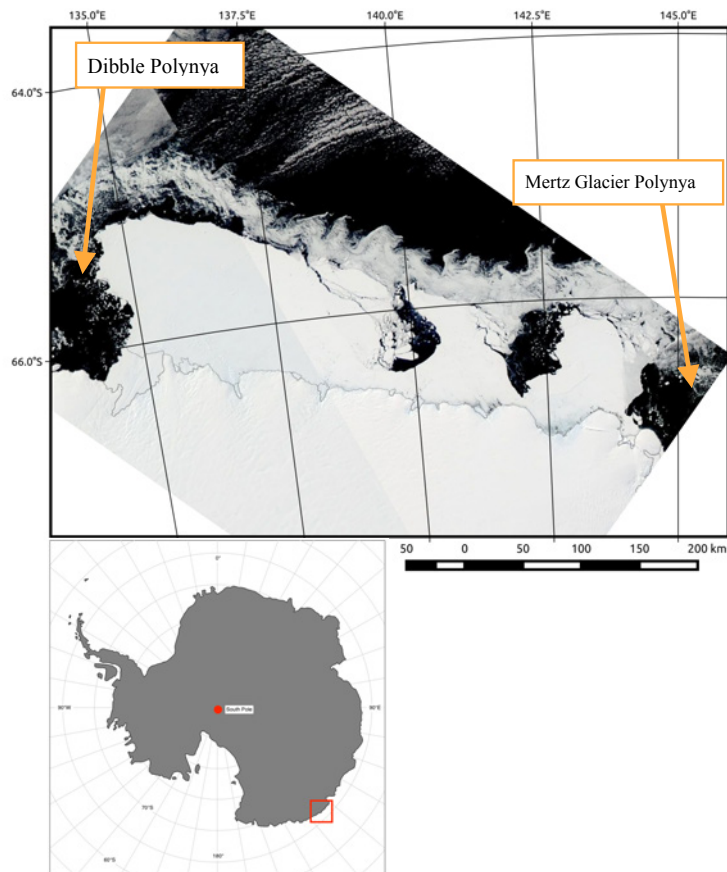
Figure 2.1   Studied area (136°E 66°S) and its vicinity. Red square box in the inset map indicates its location in Antarctica.

Antarctica coastal polynyas are major ice production sites; they produce up to 10% of sea ice in the Southern Ocean, even though the total area of the polynyas only makes up about 1% of the maximum sea ice area (Tamura et al. 2008). They are also linked to the formation of Antarctic bottom water (AABW), through brine rejection during new ice formation (Williams et al., 2008). The sinking of the dense water drives thermohaline circulation (Killworth, 1983) and biogeochemical cycles between the atmosphere and deep ocean (Miller and DiTullio, 2007).

3

Polynyas may also be the location of high biological activities, particularly during the spring and summer seasons, when primary production is enhanced by increased insolation (Arrigo and van Dijken, 2003).

Some polynyas reoccur at fixed locations, due to a combination of geographical factors (bathymetry, shoreline geometry, and coastal orography), atmospheric and oceanic features (properties of winds and currents, and distribution of air and water masses), and air-ice-water interactions (heat, moisture, momentum, and salt transfers at interfaces). Favourable conditions for the occurrence of polynyas may happen seasonally or annually, and only at specific locations. (Morales Maqueda et al., 2004).

Near the studied area, two reoccurring polynyas can be found, namely Dibble Polynya and Mertz Glacier Polynya (Figure 2.1). Nihashi and Ohshima (2015) estimated that their average area during wintertime (May to August) for the period 2003-2011 are $(5.5 \pm 2.3) \times 10^3$ km^2 and $(9.7 \pm 4.4) \times 10^3$ km^2, respectively; while their respective mean annual ice production during the freezing period (March to October) for the period 2003-2010 are 57 ± 9 km^3 and 132 ± 19 km^3.

2.2 Principles of passive microwave remote sensing

Passive microwave remote sensing is a technique that measures the microwave radiation (3 to 300 GHz) emitted by a source (e.g., the surface of the Earth) using remote sensors. The term "passive" refers to the fact that the radiation detected by the sensor is naturally emitted from the source, as opposed to "active" sensing in which the sensor itself emits radiation to the target and detects its reflection. The radiative transfer equation is the backbone of remote sensing (Section 2.2.1). For microwave remote sensing, the commonly measured parameter is the brightness temperature (Section 2.2.2). The measurements are done by a sensor, typically mounted on a satellite or an aircraft (Section 2.2.3). This grants mobility to the measuring sensor, which is particularly useful in the polar regions, although there are limitations (Section 2.2.4).
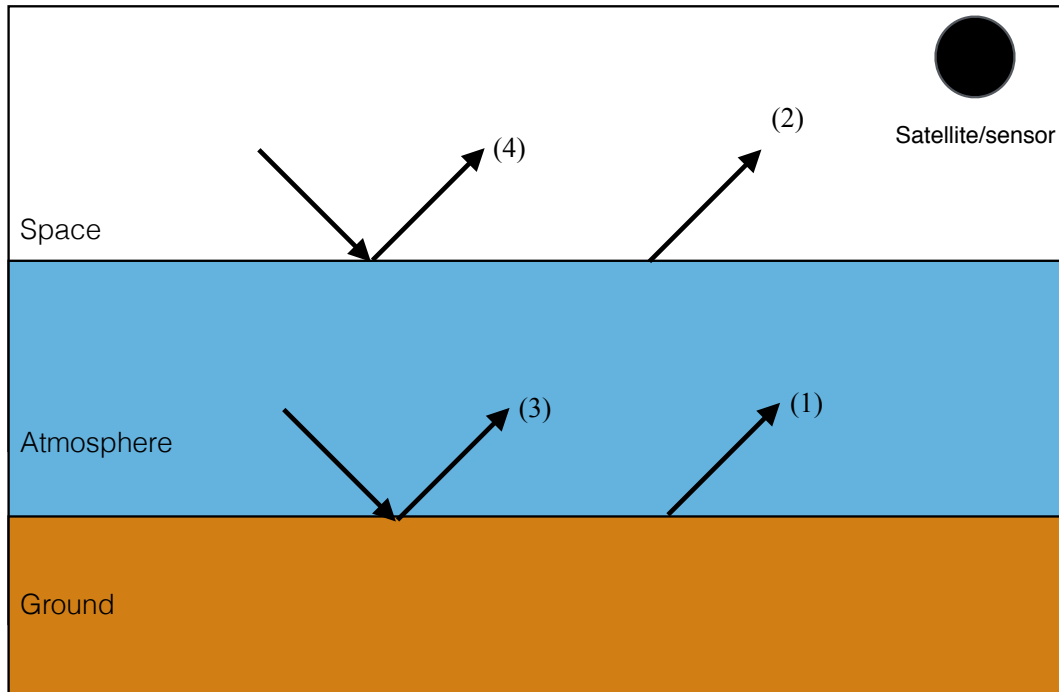
2.2.1 Radiative transfer equation

In typical passive remote sensing model of the Earth, the sources contributing to the radiation detected by a satellite sensor are (Figure 2.2):

(1) surface emission;

(2) upward atmospheric emission;

(3) reflection from downward atmospheric emission; and

(4) reflection of cosmic radiation.

As the radiation passes the Earth's atmosphere, its intensity drops due to the transparency of the atmosphere that depends on the wavelength, resulting in the following relation,

Radiation detected = surface emission × atmospheric transmission

+ upward atmospheric emission

+ reflection from downward atmospheric emission × atmospheric transmission

+ reflection of cosmic radiation × atmospheric transmission

Figure 2.2   Radiative transfer model for passive microwave remote sensing. (1) surface emission; (2) upward atmospheric emission; (3) reflection from downward atmospheric emission; and (4) reflection of cosmic radiation.

2.2.2   Brightness temperature

Brightness temperature is a common parameter used to represent the intensity of the signal received by a passive microwave sensor. It is defined as the temperature of a blackbody that emits the same intensity as measured, where a blackbody is an object that absorbs all incident radiation and re-radiate energy with characteristics unique to the object only. Brightness temperature is derived from Planck's function

$$L_v = \frac{2hv^3}{c^2}\left(e^{\frac{hv}{kT}} - 1\right)^{-1}$$

(2.1)

where L_v is the intensity of radiation as a function of frequency v, h is the Planck's constant, c is the speed of light, k is the Boltzmann's constant, and T is the temperature.

Using Rayleigh-Jeans Approximation ($kT >> hv$), which is valid for typical temperatures (200-300 K) and frequencies (3-300 GHz) encountered in microwave remote sensing of sea ice, Equation (2.1) can be simplified as

$$L_v = \frac{2v^2kT}{c^2} \tag{2.2}$$

Rearranging the terms gives the brightness temperature T_B of a blackbody, which also equals its physical temperature $T_{physical}$:

$$T_B = \frac{c^2}{2v^2k}L_v = T_{physical} \tag{2.3}$$

For non-blackbody objects, the brightness temperature would depend on its emissivity ε, which is defined as the ratio between the brightness of an object at temperature T to that of a blackbody at the same temperature, at a certain frequency v (Woodhouse, 2006):

$$\varepsilon \equiv \frac{\text{brightness of an object at temperature } T}{\text{brightness of a blackbody at temperature } T} \tag{2.4}$$

As such, the brightness temperature of a non-blackbody object is

$$T_B = \varepsilon T_{physical} \tag{2.5}$$

From the radiative transfer equation in Section 2.2.1, the following relation can be obtained:

$$T_B = \varepsilon T_s e^{-\tau} + T_{B,up} + (1-\varepsilon)T_{B,down}e^{-\tau} + (1-\varepsilon)T_{cosmic}e^{-2\tau} \tag{2.6}$$

where T_B is the brightness temperature measured, ε is the surface emissivity, T_s is the surface temperature, $T_{B,up}$ is the brightness temperature of the upward atmospheric emission, $T_{B,down}$ is the brightness temperature of the downward atmospheric emission, T_{cosmic} is cosmic temperature, τ is the optical depth of the atmosphere and $e^{-\tau}$ is the atmospheric transmittance.

2.2.3 Satellite and Sensor

A sensor is an instrumental element, usually mounted on a satellite or an aircraft for the purpose of remote sensing, that receives radiation signal from an emitter. The main data analysed in this study are products of the Advanced Microwave Scanning Radiometer 2 (AMSR-2) sensor. AMSR-2 is mounted on the Global Change Observation Mission-Water "SHIZUKU" (GCOM-W1) satellite and measures weak microwave emission from the surface and the atmosphere of the Earth. The satellite has been launched on 18 May 2012, and has been delivering data since August 2012.

Since 25 January 2013, the calibrated brightness temperature data have been available for public access. The Institute of Environmental Physics (IUP: Institut für Umweltphysik) at the University of Bremen have been producing daily sea ice concentration maps from these data since 26 January 2013.

The AMSR-2 instrument is a conically-scanning passive microwave radiometer system that measures in seven frequency bands ranging between 6.925 GHz and 89.0 GHz at both horizontal and vertical polarization. It orbits at about 700 km above the Earth at an inclination angle of 98.2°. Due to the slight inclination, the satellite does not pass directly over the two poles. The feedhorns of the antenna, which rotates one per 1.5 seconds, scan at an incidence angle of 55° and acquires data over a 1450 km swath on the Earth's surface. The conical scan mechanism allows AMSR-2 to obtain a set of daytime and nighttime data with more than 99% coverage of the Earth every 2 days, with less than 1% loss due to the missing data at the poles.

2.2.4   Advantages and disadvantages

Two main advantages of using passive microwave remote sensing in the polar regions are as follows. First, microwaves are emitted independent of the solar source, contrary to visible light. This enables us to make continuous measurements in spite of darkness, which lasts for a prolonged period in the poles in their respective winters. Second, microwaves, at low frequencies, are largely unaffected by atmospheric conditions. They are able to penetrate clouds and precipitations, which occurs commonly in the polar regions due to variations in local weather. Low frequency microwave measurements can be used to remove weather effects from the ice concentration measurements at higher frequencies, which has the advantage of having higher resolutions but are prone to atmospheric influence (Section 2.4.2).

Compared to visible light measurements, a major disadvantage of microwave sensing is its low spatial resolution on the ground surface, which can be approximated by the product of the frequency v and the opening aperture of the sensor system. Spatial resolution increases with the frequency of the radiation detected. Microwaves (3×10^9 to 3×10^{11} Hz) has frequencies five orders of magnitude lower than visible light (3×10^{14} to 3×10^{16} Hz). In terms of spatial resolution, microwave remote sensing (in kilometre scale) has much lower resolving ability than optical measurements (in metre scale).

2.3   Sea ice physics

Sea ice makes up a large part of the cryosphere, the frozen water part of the Earth's surface, on land and in water. It is the only part of the cryosphere that originates from seawater instead of fresh water. Globally, sea ice properties is one of the proxy to monitor climate change. Regionally, sea ice plays the particular role as a barrier between the ocean and the atmosphere. It regulates heat flow between the ocean and the atmosphere, and can thereby exerts effects on local weather and thermohaline circulation, and ultimately on climate. Sea ice monitoring is also a prime subject in ship navigation in the polar regions, to ensure safe passage.

Monitoring the formation and growth of sea ice (Section 2.3.1), as well as its surface snow cover (Section 2.3.2), are essential for polar studies. Each surface type (seawater, ice, snow) has its distinct microwave signature (Section 2.3.3). It is the principle behind most of the ice concentration retrieval algorithm, including the ASI algorithm used in this study (Section 2.3.4).

2.3.1   Formation and growth of sea ice

When the temperature of seawater drops below its freezing point (-1.8°C at salinity of 35), sea ice begins to form. Figure 2.3 depicts schematically the stages of development in sea ice formation. The terms for classification follow the Sea Ice Nomenclature published by World Meteorological Organization (WMO, 1989). At the first stage, seawater freezes to form fine crystals or plates of ice, typically of 3 to 4 mm in diameter, named frazil ice. Depending on the ocean conditions, frazil ice will develop into ice sheet via different pathways. In calm oceans, the ice crystals will conglomerate and develop into a soupy layer on the surface, referred to as grease ice. Grease ice will then coagulate to form a coherent thin sheet of ice called nilas. In rough waters, frazil ice groups together in circular disks called pancake ice, referring to their shape. Pancake ice disks collide with each other and eventually consolidate into a continuous ice sheet. All the ice types mentioned above can be collectively referred to as new ice, with thickness up to 10 cm. Once sea ice forms into sheets of ice, it continues to grow during the winter into young ice (thickness of 10 to 30 cm) and eventually into first-year ice if the growth is not more than one winter's time. Ice that has survived one summer's melt, meaning that it only thins during summer but not completely melts, is called second-year ice while those that has survived at least two summer's melt is called multiyear ice. Their thickness can exceed 2 to 3 m.

8
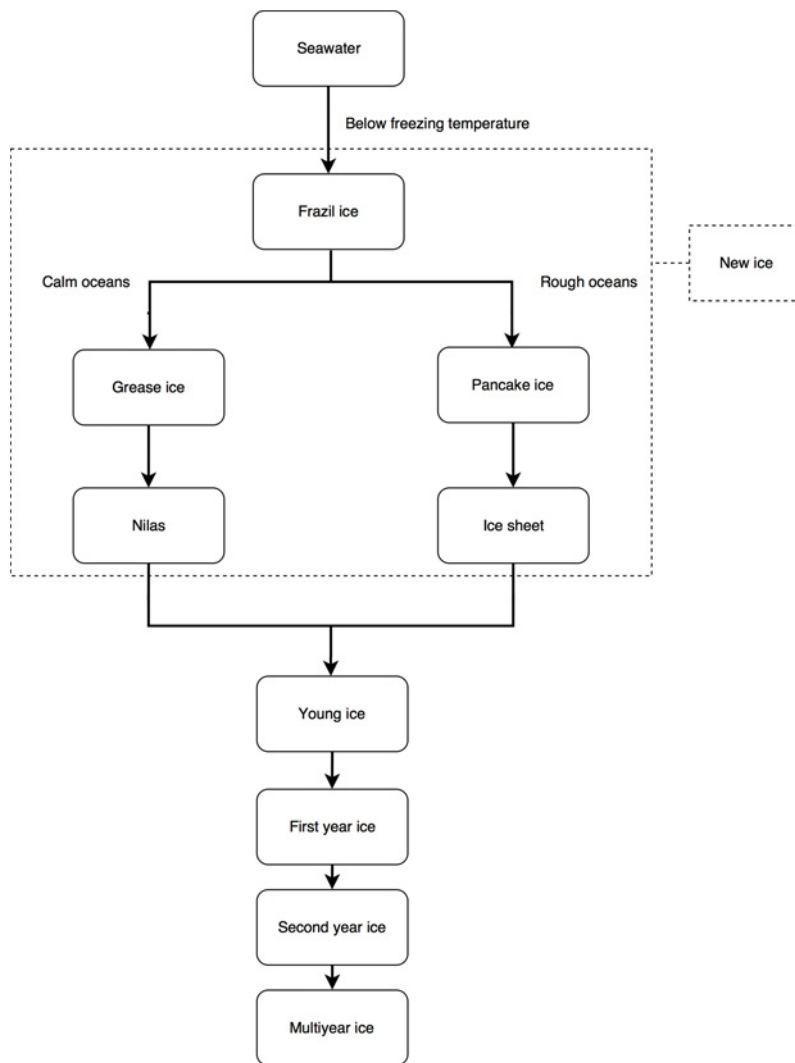
Figure 2.3   Stages of development in sea ice formation and growth.

2.3.2   Ice-ocean interaction

Upon freezing, salt is expelled from the newly formed sea ice, a process known as brine rejection. Since freezing is a rather rapid process, pockets of salty water (brine) are trapped with the ice, before reaching the ice bottom. Under gravity, brine will move from the pockets towards the ice bottom (brine drainage). However, Untersteiner (1968) suggested that gravity could not be the sole mechanism of brine drainage in floating sea ice, as the only force exerted on the brine is the effective gravity due to the small difference in specific gravity between brine and seawater. Another important mechanism, flushing, refers to the percolation of fresh water through miniature tubes within sea ice, which could happen when surface melting occurs and when the ice becomes more

porous. These would be enhanced by the higher temperature in summer. Therefore, the salinity of sea ice decreases with its age.

Brine drainage creates dense water of high salinity in the vicinity of newly-formed ice, and is one of the contributing sources of Antarctic bottom water (AABW; Ohshima et al., 2013). Dense, saline water from brine drainage accumulates below the ice shelf, collectively referred to as High Salinity Shelf Water, which has been in contact with the atmosphere recently, helps deliver oxygen to the deep ocean. This dense water sinks down the Antarctic continental margin and flow northward along the bottom, eventually forming AABW. Whether a region is favourable for AABW formation depends on various factors: the shape of the coastline, the bathymetry of the basin, and a polynya system.

2.3.3   Snow on sea ice

Snow cover on sea ice is an important part of the climate system due to its effects in modifying energy and freshwater fluxes between atmosphere, ice and ocean. Similar to sea ice, snow cover and thickness display a large seasonal cycle. Nicolaus et al (2006) noted that the seasonal cycles of snow thinning are very different in the two poles. In contrast to the Arctic snow cover, in Antarctica the snow cover rarely melts completely in the summer. Often, an intact or highly metamorphosed snow cover remains during the summer (Massom et al., 2001). Snow cover on ice is subjected to rapid changes and metamorphosis due to weather conditions, and would subsequently lead to variations in microwave signature of the surface (Anderson, 1997; Abdalafi and Steffen, 1995; Markus and Cavalieri, 1998).

2.3.4   Microwave signatures of seawater, ice, and snow

A microwave radiometer measures the brightness temperature, which is linearly proportional to emissivity (Section 2.2.2). Different types of surface have their characteristic ranges of emissivity, depending on the incidence angle θ, frequency v, and the polarization (subscript V for vertical; H for horizontal) of the radiation. These dependences can be summarized by the Fresnel equations for a specular surface (Meissner and Wentz, 2012):

$$\varepsilon_H(v,\theta) = 1 - \left| \frac{\cos\theta - \sqrt{D(v) - \sin^2\theta}}{\cos\theta + \sqrt{D(v) - \sin^2\theta}} \right|^2 \tag{2.7}$$

$$\varepsilon_V(v,\theta) = 1 - \left| \frac{D(v)\cos\theta - \sqrt{D(v) - \sin^2\theta}}{D(v)\cos\theta + \sqrt{D(v) - \sin^2\theta}} \right|^2 \qquad (2.8)$$

where $D(v)$ is the dielectric constant of the surface. D is a function of the frequency v, and is dependent on temperature and salinity. As seen in Section 2.3.1, salinity of sea ice differs from that of sea water and changes as it forms and grows. Therefore it is possible to separate the surface types by emissivity. Roughness and vertical profile of the surface (e.g., whether there is snow cover) would also influence D.

Figure 2.4 shows the dependence of emissivity of a specular surface on the incidence angle θ at three frequencies used in the ASI and Bootstrap algorithms (Section 2.4). At $\theta = 0°$, the emissivity for both polarizations are identical for each frequency. As θ increases, the emissivities in horizontal polarization decrease monotonically, while those in vertical polarization increase and reach their maximum in the range of 70° to 80°. Thus the emissivity difference of the two polarizations increase with θ until around 80° and reduces beyond. Note that the actual curves for ice surface may differ, as small-scale roughness on sea ice may exert slight effect on its microwave emission. The AMSR-2 radiometer measures constantly with an incidence angle of 55° to ensure consistent measurements of the polarization differences.

Figure 2.5 shows the emissivity of sea water and various types of sea ice as a function of frequency, at an incidence angle of 50°. At 89.0 GHz, which is primarily used by the ASI algorithm (Section 2.4.1), the emissivity differences for the three sea ice types are similar and are smaller that for sea water. This contrast is also valid for the polarization difference in brightness temperature, since emissivity and brightness temperature are linearly related, and the physical temperature is independent of the polarization (Section 2.2.2). This distinction in polarization difference between sea ice and water is utilized in the ASI algorithm for ice concentration retrieval.

2.4   Ice concentration retrieval by the ASI algorithm

2.4.1   The algorithm

Based on a retrieval model of ice concentration from dual-polarized microwave radiation near 90 GHz developed by Svendsen et al. (1987), modifications on the original Svendsen et al. algorithm (SVA) has been done by Kaleschke et al. (2001) to formulate the ASI algorithm. SVA was designed to benefit from the highest frequency channels (85 GHz) of the radiometer SSM/I (The Special Sensor Microwave Imager) to determine total ice concentration at high resolution. It is

based on the difference in polarization between water and sea ice. Figure 2.5 shows that the emissivity difference between vertically and horizontally polarized channels at various frequencies is larger for open water than for several types of sea ice, where emissivity difference is defined as

$$\Delta\varepsilon = \varepsilon_V - \varepsilon_H \tag{2.9}$$
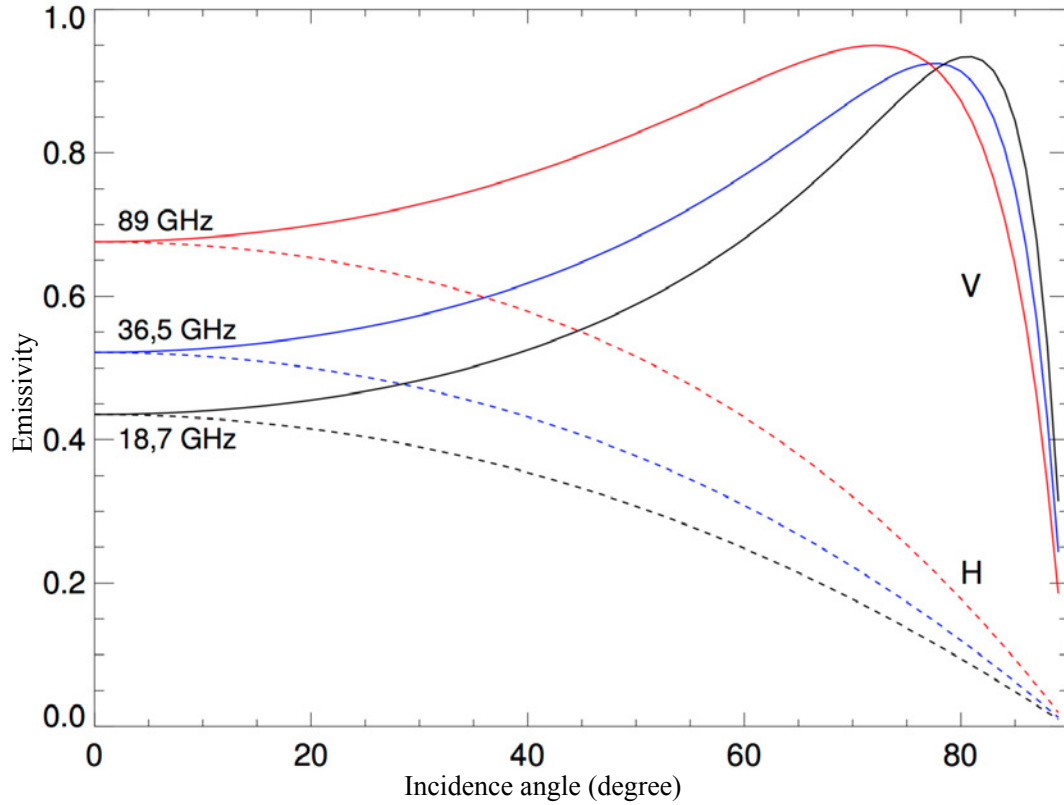
Figure 2.4   Dependence of emissivity of a specular surface on the incidence angle θ at 18.7, 36.5, and 89.0 GHz. Adapted from "Meereisfernerkundung mit dem satellitengestützten Mikrowellenradiometer AMSR(-E) – Bestimmung der Eiskonzentration und Eiskante unter Verwendung der 89 GHz-Kanäle" by G. Spreen, 2004, diploma thesis (comp. master's thesis), University of Hamburg, Hamburg, Germany, prepared at the University of Bremen, Dept. of Physics and Electrical Engineering.

From Equation (2.5), the difference in emissivity will result in difference in brightness temperature. With this relation, the polarization difference at a surface at a certain frequency can be defined as

$$P_s = T_{B_{s,V}} - T_{B_{s,H}} = \Delta\varepsilon T_s \tag{2.10}$$

where the subscript *s* denotes parameters at surface, T_B is the brightness temperature and subscripts *V* and *H* refer to vertical and horizontal polarization respectively, and T_s is the physical temperature of the surface. Note that the physical temperature is always identical in both vertical and horizontal polarization. As such it is possible to distinguish between ice and open water by brightness temperature measurements and subsequent calculations for P_s.
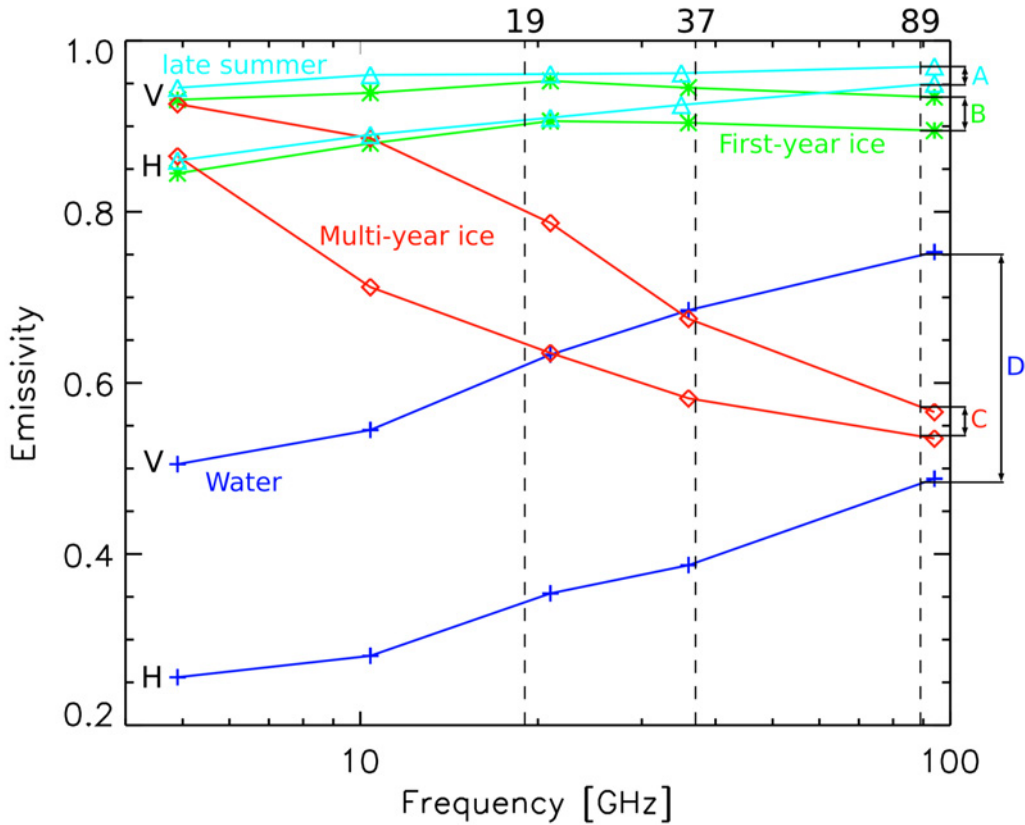
Figure 2.5   Emissivity of sea water and sea ice types as a function of frequency, measured at an incidence angle of 50°. Adapted from "Sea ice remote sensing using AMSR-E 89-GHz channels" by G. Spreen, L. Kaleschke, and G. Heygster, 2008, *J. Geophys. Res.*, 113.

To calculate the ice concentration in a pixel, the following scheme is used. Brightness temperature T_B of a surface *s* has contributions from both open water and ice

$$T_{B_{s,p}} = C T_{B_{i,p}} + (1 - C) T_{B_{w,p}} \tag{2.11}$$

where *C* is the ice concentration and the subscript *p* represents vertical (*V*) or horizontal (*H*) polarization.

Substituting Equation (2.11) into Equation (2.10) and rearrange,

$$P_s = CP_{s,i} + (1-C)P_{s,w} \tag{2.12}$$

$$P_s = C(P_{s,i} - P_{s,w}) + P_{s,w} \tag{2.13}$$

where $P_{s,i}$ and $P_{s,w}$ are the polarization difference of ice and water, respectively, at the surface.

Taking into account the atmospheric influence a_c on the polarization difference, the polarization difference actually measured by an airborne sensor will be

$$P = P_s \, e^{-\tau}(1.1e^{-\tau} - 0.11) = P_s \, a_c \tag{2.14}$$

where τ is the atmospheric opacity. Following Svendsen et al. (1987), Equation (2.14) assumes that the atmosphere is horizontally stratified under Arctic conditions, with the vertical temperature profile replaced by an effective temperature, and a diffusely reflecting surface viewed under an incidence angle of approximately 50°. Atmospheric influence a_c is a function of ice concentration C (Svendsen et al. 1983, 1987); for instance, water vapour content and cloud liquid water decrease with increasing ice cover, because reduced open water areas lowers evaporation.

Combining Equations (2.13) and (2.14), the polarization difference detected by the sensor as a function of ice concentration C can be written as

$$P = a_c \left[C(P_{s,i} - P_{s,w}) + P_{s,w} \right] \tag{2.15}$$

Setting C to 0 (open water) and to 1 (ice-covered) in Equation (2.15), we obtain the following two equations for polarization difference at 0% (2.16) and at 100% (2.17) ice concentration respectively.

$$P_0 = a_0 P_{s,w} \tag{2.16}$$

$$P_1 = a_1 P_{s,i} \tag{2.17}$$

Applying Taylor expansion to Equation (2.15), neglecting higher order terms, results in

$$P = a_0 C(P_{s,i} - P_{s,w}) + P_0 \qquad \text{for } C \to 0 \tag{2.18}$$

$$P = a_1 (C-1)(P_{s,i} - P_{s,w}) + P_1 \qquad \text{for } C \to 1 \tag{2.19}$$

Assuming that the variation of the atmospheric influence is small for totally ice covered ($C = 1$) or open water areas ($C = 0$), the derivatives of the atmospheric influence a_0' for $C = 0$ and a_1' for $C = 1$ are taken as zero.

Substituting Equations (2.16) and (2.17) into Equations (2.18) and (2.19), rearranging such that the atmospheric influence terms a_c are replaced and solving for C

$$C = \left(\frac{P}{P_0} - 1\right)\left(\frac{P_{s,w}}{P_{s,i} - P_{s,w}}\right) \qquad \text{for } C \to 0 \tag{2.20}$$

$$C = \frac{P}{P_1} + (\frac{P}{P_1} - 1)(\frac{P_{s,w}}{P_{s,i} - P_{s,w}}) \qquad\qquad \text{for } C \to 1 \qquad\qquad (2.21)$$

Svendsen et al. (1987) pointed out that $P_{s,w}/(P_{s,i} - P_{s,w}) = -1.14$ is a common value for sea ice signatures in Arctic conditions. Retrieving ice concentration between 0 % and 100% is done by interpolation by a third-order polynomial

$$C = d_3 P^3 + d P_2^2 + d_1 P + d_0 \qquad\qquad (2.22)$$

Using Equations (2.20) and (2.21) and their partial derivatives with respect to P, the following system of linear equations is obtained

$$\begin{bmatrix} P_0^3 & P_0^2 & P_0 & 1 \\ P_1^3 & P_1^2 & P_1 & 1 \\ 3P_0^3 & 2P_0^2 & P_0 & 0 \\ 3P_1^3 & 2P_1^2 & P_1 & 0 \end{bmatrix} \begin{bmatrix} d_3 \\ d_2 \\ d_1 \\ d_0 \end{bmatrix} = \begin{bmatrix} 0 \\ 1 \\ -1.14 \\ -0.14 \end{bmatrix} \qquad (2.23)$$

If P_0 and P_1, called the tie points, are known, then solving (2.23) for the coefficients d_i, the ice concentration can be calculated by Equation (2.22). C is set to zero for $P > P_0$ and to one for $P < P_1$. In the original SVA, the tie points P_0 and P_1 are selected by the maxima and minima of the polarization difference of the corresponding swath (Svendsen et al., 1987). However, the values found are often not representative for open water and fully ice covered cases, due to varying atmospheric influence within one swath. Moreover, nonphysical steps occur when the swaths are combined (Lomax et al., 1995; Kaleschke et al., 2001). In the ASI algorithm, two constant tie points P_0 and P_1 are selected by comparison with other well validated reference data (Spreen et al., 2008).

2.4.2   Weather filters

High frequency microwave channels are sensitive to atmospheric influences, such as cloud liquid water and water vapor. Spreen et al. (2008) noted that polarization difference of water can be reduced to values close to the typical values of sea ice if there are cyclones present over open water, which will result in spurious ice concentration reported in open water areas. Therefore the ASI algorithm contains three weather filters using lower frequency channels that are less affected by atmospheric conditions.

1. Following Gloersen and Cavalieri (1986), the first weather filter uses the gradient ratio (GR) of the 36.5 GHz and 18.7 GHz channels

15

$$GR(36.5/18.7) = \frac{T_B(36.5,V) - T_B(18.7,V)}{T_B(36.5,V) + T_B(18.7,V)}$$

GR(36.5/18.7) is positive for water but close to zero or negative for ice. It mainly filters high cloud liquid water cases.

$$GR(36.5/18.7) \geq 0.045 \Rightarrow C(ASI) = 0\%$$

Data points with GR(36.5/18.7) greater than 0.045 are set to C = 0 in the ASI algorithm (Spreen, 2004).

2. To filter out cases of high water vapor above open water, the second filter uses the gradient ratio $GR(23.8/18.7)$ (Cavalieri et al., 1995).

$$GR(23.8/18.7) = \frac{T_B(23.8,V) - T_B(18.7,V)}{T_B(23.8,V) + T_B(18.7,V)}$$

Similar to the first filter, a threshold of 0.04 is set such that data points with GR(23.8/18.7) greater than 0.04 are set to C = 0.

$$GR(23.8/18.7) \geq 0.04 \Rightarrow C(ASI) = 0\%$$

3. The final filter makes reference to the Bootstrap algorithm (Section 2.4.2.1), which is an ice concentration retrieval algorithm using lower frequency channels and contains its own weather filters. Data points with ice concentration derived from the Bootstrap algorithm less than 5% are set to C = 0 in the ASI algorithm.

$$C(Bootstrap) \leq 5\% \Rightarrow C(ASI) = 0\%$$

2.4.2.1 The Bootstrap algorithm

Details of the implementation of the Bootstrap algorithm can be found in Comiso (1995). For the Antarctic, the Bootstrap algorithm retrieves ice concentration using brightness temperature data from the 18/19 GHz and 36/37 GHz channels in their vertical polarization, and contains its own weather filters. The Bootstrap algorithm offers lower resolution than the ASI algorithm, because of the lower frequency channels used; but the advantage is that these channels are less affected by atmospheric effect compared to the 89.0 GHz channel used in the ASI algorithm. Comiso (1995) noted that the Bootstrap algorithm is subjected to error due to new ice formation, spatial changes in physical temperature and in emissivity. Emissivity changes could be due to variations of the snow cover on ice such as surface wetting and flooding. This is supported by the observations by Mätzler et al. (1984) that the emissivity of sea ice at vertical and horizontal polarizations response distinctly to ice layering, roughness effects, snow wetness and flooding.

16

3   Investigation into the occurrence of the artefact

3.1   Motivation

Passive microwave remote sensing has enabled us to monitor sea ice in polar regions extensively in spatial scale and continuously in temporal scale. Over the past years, many efforts have been made by individuals and groups to validate sea ice data with optical observations from ships or aircrafts (e.g., Cavalieri et al., 1991; Comiso et al., 1997; Ivanova et al., 2014). These studies have raised our confidence in the accuracy of satellite data products. Nonetheless, numerous factors such as atmospheric conditions, surface properties, snow cover and metamorphosis, and geographic locations, could both individually and interdependently affect the results obtained from satellite remote sensing. To complicate matters, not all of these factors are thoroughly modelled or investigated, therefore despite various attempts in algorithm validations, many of which show general agreement among the algorithms, there exists mismatch of results in individual cases.

This study focuses on one of these mismatch in ice concentration. Contradictions between sea ice concentration maps produced from ARTIST (Arctic Radiation and Turbulence Interaction STudy) Sea Ice (ASI) algorithm and MODIS (Moderate Resolution Imaging Spectrometer) images in a region around 136°E 66°S, near the Dibble Iceberg Tongue in East Antarctica (Figure 3.1), have been observed (N. Young, personal communication, February 11, 2014). In the investigated area, fast ice usually prevails for several years; polynyas have been observed along the ice edge within the ice pack. However, the ASI algorithm shows episodes of spurious occurrence of polynya (in this essay referred to as "the artefact") that are not observed in the optical images from MODIS.

Figure 3.1 shows an example of the mismatch on 20 February 2014. At 137.5°E 66°S, an open water area that resembles a polynya ("the artefact") can be seen on the image derived from the ASI algorithm. However, on the MODIS image of the same date (selected because of its cloud-free condition on the MODIS image), the same location is observed to be ice-covered, and the image is largely cloud-free. As we will see in the coming sections, such mismatch has occurred for many days from February to April 2014, during which the size of the artefact has varied and at times has disappeared. This study aims to find out the reasons for the occurrence of such phenomenon, and to provide viable solutions to mitigate its occurrence.
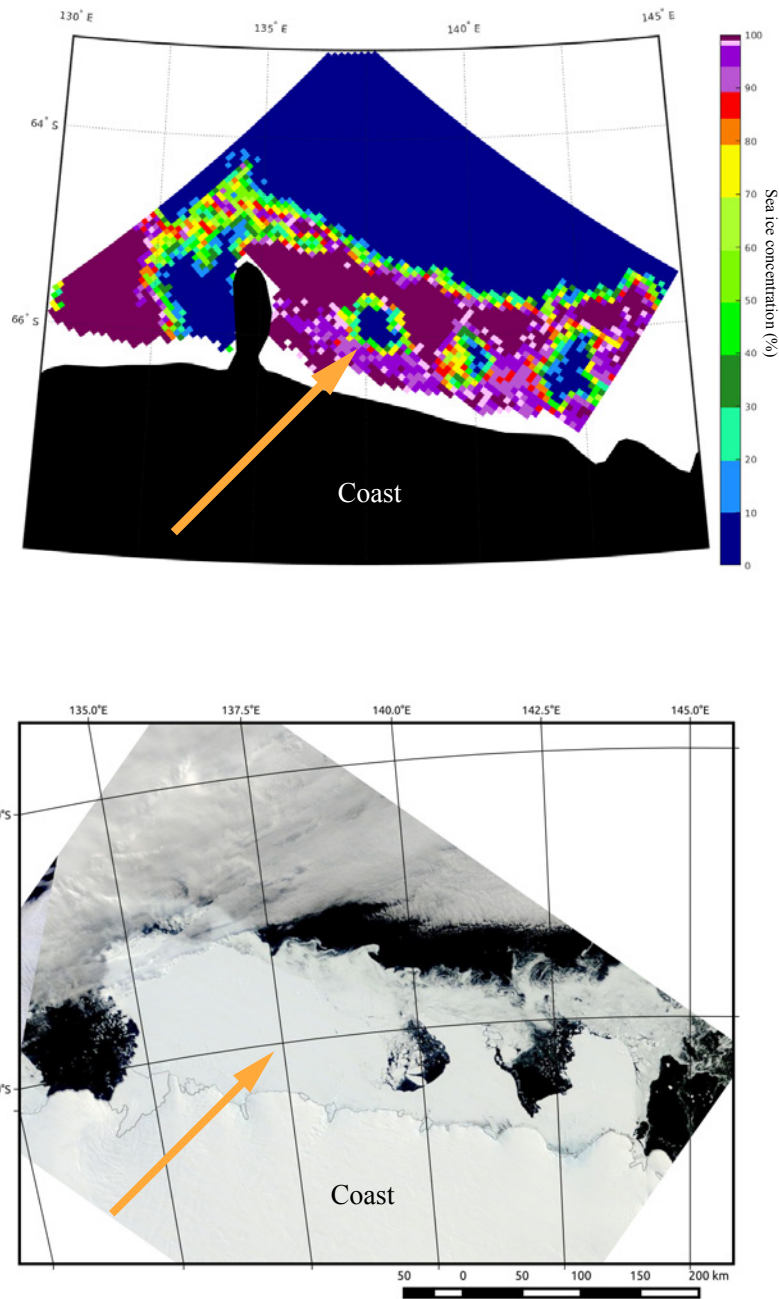
Figure 3.1 (a) Ice concentration map of retrieved by the ASI algorithm and; (b) Visual image from MODIS, available at http://go.nasa.gov/29igHUo; of the studied area on 20 February 2014. Orange arrows indicate the same location on both maps.

3.2   Data investigated

Regarding ice concentration, data derived by the ASI algorithm and by the Bootstrap algorithm using data from AMSR-2 were analysed. They are available in HDF format on the IUP server (http://seaice.uni-bremen.de/amsr2data/; accessed on 1 February 2016). Since AMSR-2 data only extends back to August 2012, data from its predecessor, the Advanced Microwave Scanning Radiometer-Earth Observing System (AMSR-E; available at http://seaice.uni-bremen.de/amsredata/; accessed on 1 February 2016), were also analysed, which covers temporally from June 2002 to October 2011. The same ASI algorithm has been used to retrieve ice concentration values from the AMSR-E dataset. Both datasets are provided in the polar stereographic projection at a grid cell size of 6.25×6.25 km. A list of some important parameters of AMSR-2 and AMSR-E can be found in Table 3.1. Furthermore, brightness temperature data from AMSR-2 were analysed, also available from the mentioned server.

Table 3.1 Sensor characteristics of AMSR-2 and AMSR-E

Sensor	AMSR-2			AMSR-E		
Satellite Platform	GCOM-W1			AQUA		
Altitude	700 km			705 km		
Equator Crossing Time (Local time zone)	1:30 PM Ascending 1:30 AM Descending			1:30 PM Ascending 1:30 AM Descending		
Antenna Size	2 m			1.6 m		
Swath Width	1450 km			1450 km		
	Band (GHz)	Polarization*	Spatial Resolution (km x km)	Band (GHz)	Polarization	Spatial Resolution (km x km)
	6.93		62 x 35	6.93	V,H	75 x 43
	7.3		62 x 35	-	-	-
	10.65		42 x 24	10.65	V,H	51 x 29
	18.7	V,H	22 x 14	18.7	V,H	27 x 16
	23.8		19 x 11	23.8	V	32 x 18
	36.5		12 x 7	36.5	V,H	14 x 8
	89.0		5 x 3	89.0	V,H	6 x 4
	*V: Vertical H: Horizontal					

Alternative ice concentration data from other sources were also studied (Section 3.3.2). These include ice concentration using measurements from the Scanning Multichannel Microwave Radiometer (SMMR) on the Nimbus-7 satellite and from the Special Sensor Microwave/ Imager (SSM/I) sensors on the Defense Meteorological Satellite Program's (DMSP) -F8, -F11, and -F13 satellites , derived by the Bootstrap algorithm (http://nsidc.org/data/NSIDC-0079; accessed on 15 March 2016); those using the same measurements and derived by the revised NASA Team algorithm (NTA; data available at http://nsidc.org/data/NSIDC-0051; accessed on 3 August 2016); as well as those derived by the the Ocean and Sea Ice Satellite Application Facility (OSISAF) Bristol/Bootstrap hybrid algorithm (ftp://osisaf.met.no/reprocessed/ice/conc/v1p2; accessed on 3 August 2016). Further descriptions of the latter two algorithms can be found in Brucker et al (2014) and Tonboe et al. (2016) respectively.

Environmental parameters are also taken into account (Section 3.4). The 2 metre temperature and snowfall data, available as a part of the ECMWF Reanalysis (ERA)-Interim reanalysis dataset (Dee et al., 2011) on the European Centre for Medium-Range Weather Forecasts (ECMWF) Public Datasets web interface (http://apps.ecmwf.int/datasets/data/interim-full-daily/levtype=sfc/; accessed on 1 March 2016), were studied. The downloaded NetCDF files report the air temperature at the level of 2 metre above the surface and the snowfall in metres, respectively, at 1200 UTC. The 10 metre wind data from the same dataset (Dee et al., 2011) were also obtained as an NetCDF file containing the U component (Positive from west to east) and the V component (Positive from south to north), with latitude and longitude included, at 1200 UTC. They are all downloaded at a grid size of $0.75° \times 0.75°$. For these data, since one grid ($0.75° \times 0.75°$) is sufficient to cover the area of the artefact, the grid overlapping the artefact was identified and the values in that grid were used for further analyses. Finally, the bathymetry of the area was studied using data from Bedmap2 (Fretwell et al., 2013) and the Antarctic Mapping Tools by Chad Greene, available on the File Exchange platform (https://www.mathworks.com/matlabcentral/fileexchange/47638-antarctic-mapping-tools/content/AntarcticMappingTools/Documentation/html/coord_documentation.html; accessed on 10 June 2016) of MATLAB (MATLAB and Statistics Toolbox Release 2016a, The MathWorks, Inc., Natick, Massachusetts, United States).

3.3   Identifying the artefact using ice concentration data

3.3.1   ASI ice concentration

Locating the artefact

An area of 81.25 km×175 km (13×28 pixels on the ASI grid; Orange box in Figure 3.2) was selected to represent the location of the artefact observed on ice concentration maps derived from the ASI algorithm during the study period from February to April 2014. The selection is based on the ASI image on 9 February 2014, which shows one of the largest extent of the artefact during the study period based on visual inspection (Appendix A.1). The images within the studied period were inspected to ensure that the artefact is always included in this area.
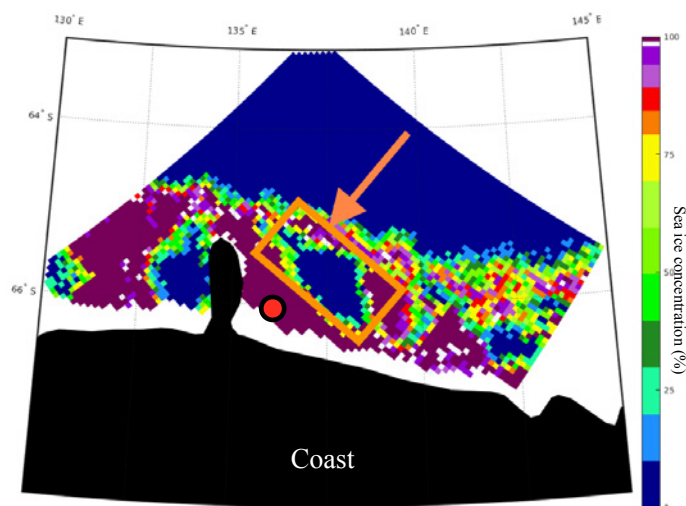
Figure 3.2   Ice concentration map of the studied area retrieved by the ASI algorithm on 9 February 2014, when the artefact has one of the largest extent during the studied period. Orange arrow indicates the box of 13×28 pixels (81.25 km×175 km) used in the calculation of the "box-to-frame" ratio (Section 3.3.1). Red dot with black outline indicates the approximate location of the reference area used in the brightness temperature analysis (Section 3.4.1).

Identifying other occurrence

In order to identify whether similar artefact has occurred at the location in other years, a parameter called the "box-to-frame ratio" was defined to characterise the artefact. The definition is as follows, with reference to Figure 3.3. Within the aforementioned studied area of 13×28 pixels, a concentric rectangular box of 9×20 pixels (on the ASI grid) is outlined. The blue rectangle represents the inner box and the orange frame (corresponding to the orange frame in Figure 3.2) represents the outer frame in Figure 3.3. Thus,

21

$$\text{Box-to-frame ratio} = \frac{\text{Average ice concentration in the inner box}}{\text{Average ice concentration in the outer frame}}$$

Furthermore, a filter is set to discard the cases when the average sea ice concentration in the outer frame is lower than 40%, as in such cases summer melt is presumed to dominate. In principle, when the whole area is fully covered with ice, the ratio will tend to unity. If there is an open water area surrounded by ice in the region, the ratio will be below 1. The drops of the ratio from unity due to summer melt should be filtered out by the 40% threshold mentioned.
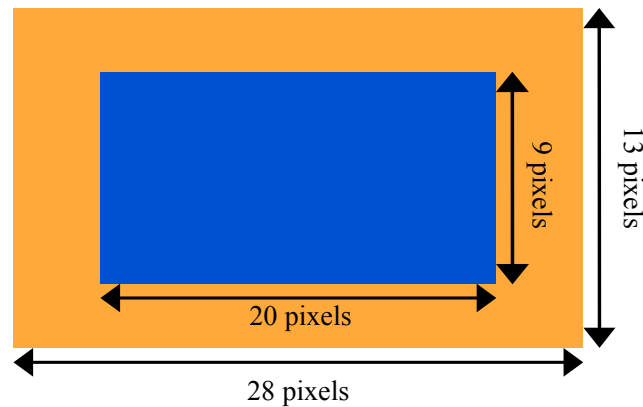
Figure 3.3   Definition of the "box" and the "frame" used in the box-to-frame ratio.

The results for the ASI ice concentration data are shown in Figure 3.4, the horizontal axis shows the time from the year 2003 to 2016, and the vertical axis shows the box-to-frame ratio. Note that there exists a significant data gap from late 2011 to mid 2012, during the time when AMSR-E has stopped working and AMSR-2 has not been in full operation. We can see that when the 40% filter is applied, the seasonal drops (presumed to be due to summer melts) are eliminated from the time series. Only the drop of the ratio in early 2014, when the artefact is observed in the studied area, remains unaffected by the filter. From these time series, we can conclude that similar occurrence of the artefact has not occurred at the location on the ASI ice concentration maps before 2014. In addition, the ASI ice concentration maps from 2015 to 2016 were visually inspected in comparison to the corresponding MODIS images, and no discrepancies was found at the location. Thus, we will focus on the period of February to April 2014.
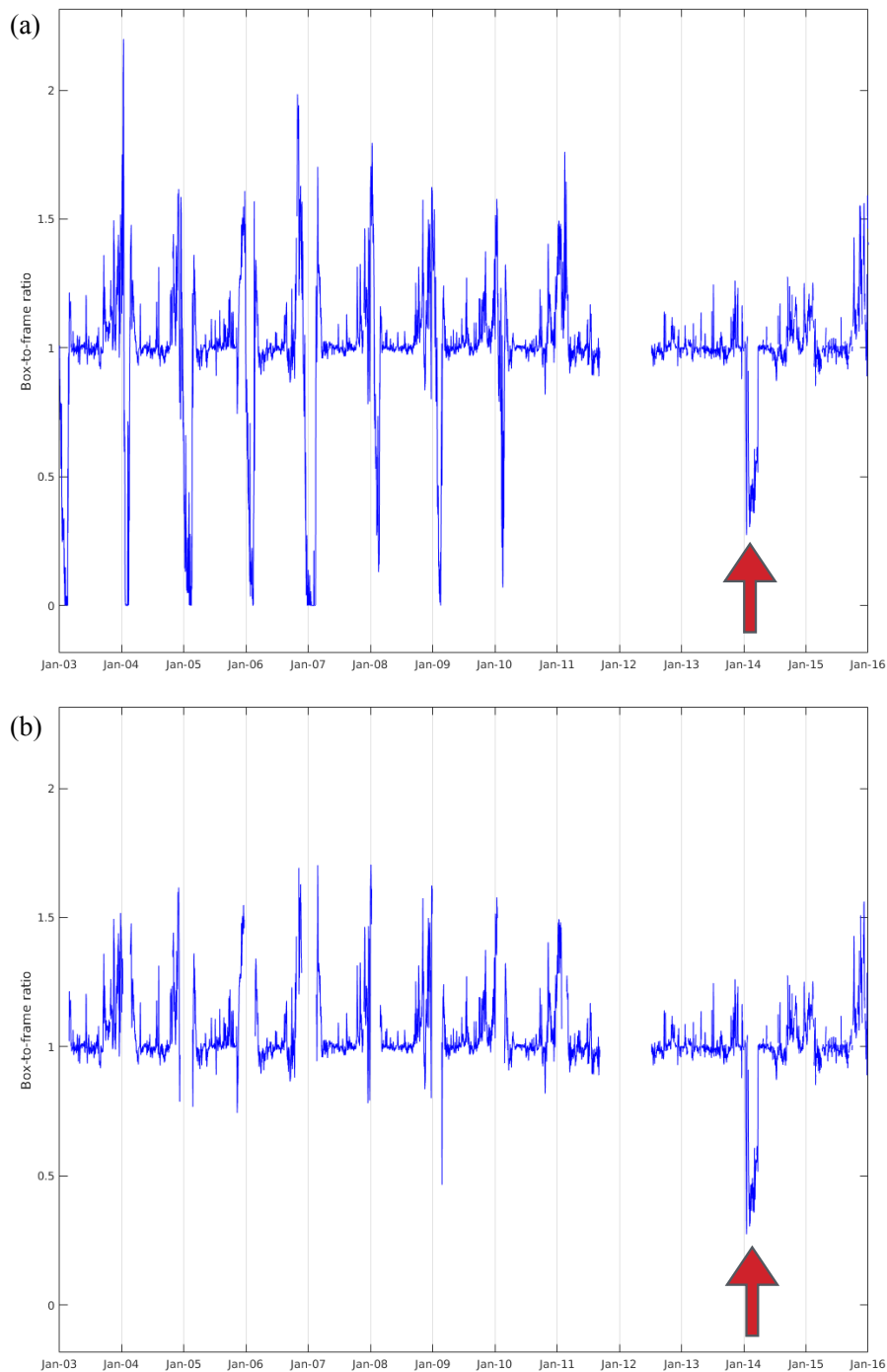
Figure 3.4 Time series of the ASI box-to-frame ratio at the artefact during 2003 to 2016 (a) with all data available and (b) with a 40% ice concentration threshold set for the outer frame such that the data during summer melt are masked. Red arrows indicate the period of the occurrence of the artefact.

23

Occurrence of the artefact

Figure 3.5 is a zoom-in of Figure 3.4(b) during the study period. We observe that there is a sudden drop in the box-to-frame ratio at the start of February 2014, followed by an immediate return to unity for several days, and then a substantial drop that lasts until mid-April, after which the value fluctuates around unity. This echoes visual inspection on the ice concentration maps derived from ASI algorithm, which found that the artefact first appeared on 2 February, and grew in size gradually; on 12 February it disappeared and the location remained ice-covered until 18 February; from 19 February the artefact appeared again and remained until 17 April, during which its size varied. Starting from 18 April 2014, we do not see such artefact again on the ASI ice concentration maps (Figure 3.6 and Appendix A.1). A list of the key dates can be found on Table 3.2.

Table 3.2 Key events regarding the occurrence of the artefact

Date	Event
2 February 2014	First appearance of the artefact on ASI ice concentration map
12 February 2014	Artefact disappeared; the location is ice-covered as reported by both the ASI algorithm and MODIS images
19 February 2014	Artefact reappeared at the location on the ASI ice concentration maps and remained, while varying in size
18 April 2014	Artefact disappeared and was not observed again at the location on the ASI ice concentration maps

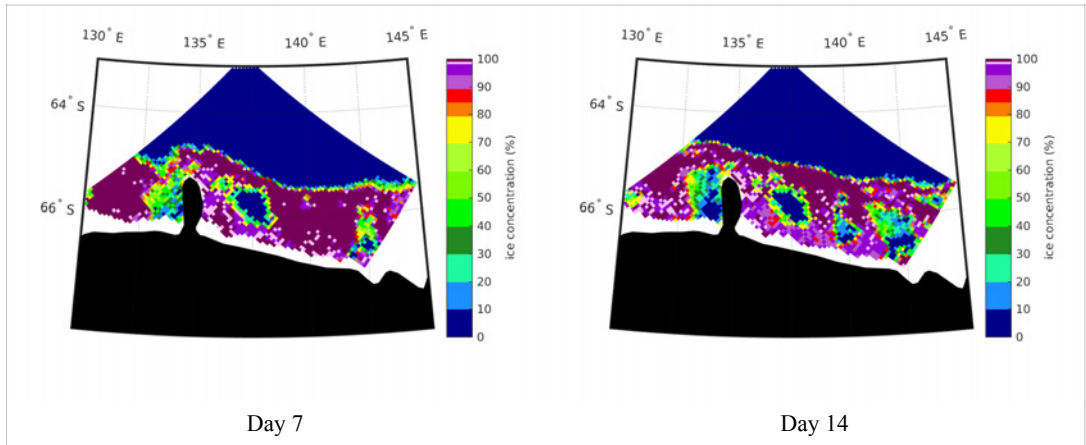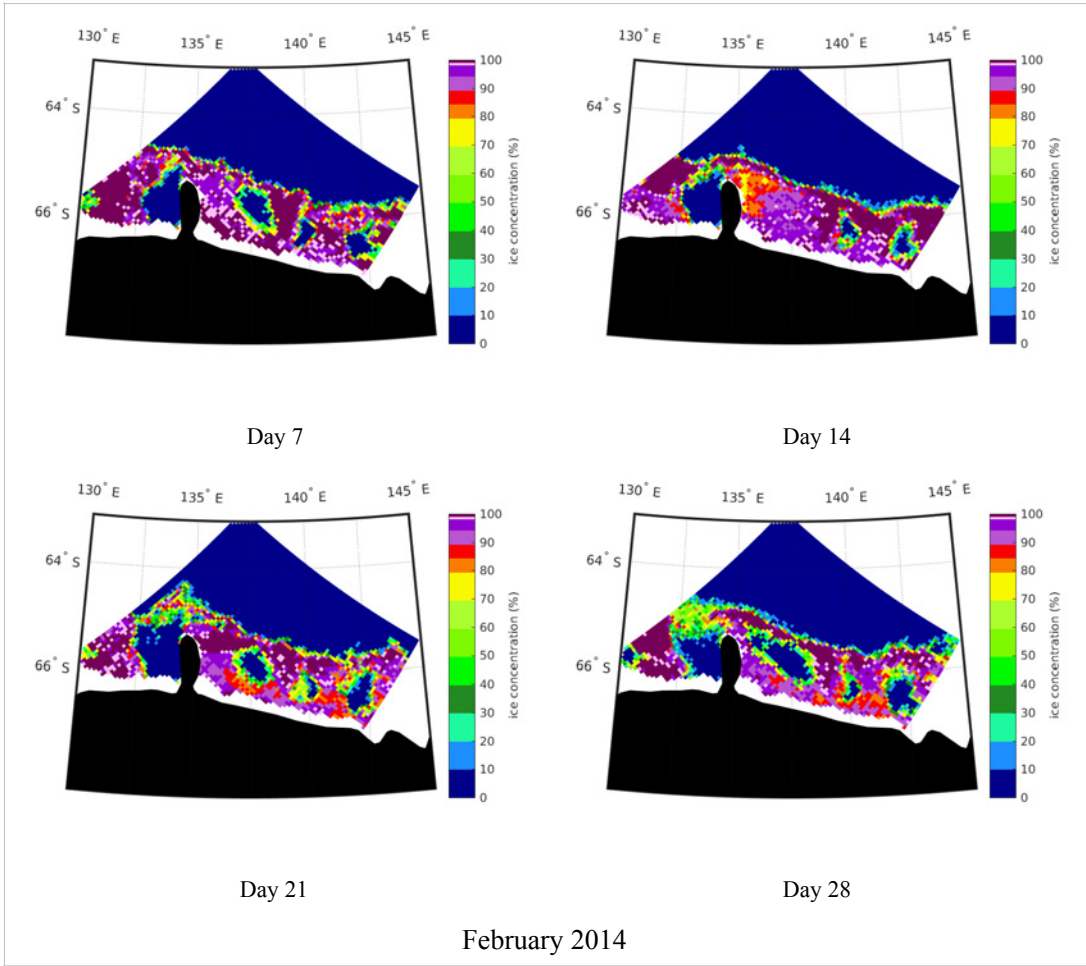3.3.2   Alternative ice concentrations

The Bootstrap algorithm is one of the widely used ice retrieval methods. Since it is included in the ASI algorithm as one of the weather filters, ice concentration maps retrieved by the Bootstrap algorithm during January to April 2014 were also created to determine the presence of the artefact (Figure 3.8 and Appendix A.2). We can see that at the location where the artefact appeared on the ASI ice concentration maps (around 137.5°E 66°S), an artefact also appears on the Bootstrap maps. This is the main factor contributing to the occurrence of the artefact on the ASI maps, due to the effect of the Bootstrap filter in the ASI algorithm, which will set pixels of low ice concentration (< 5%) to 0% (Section 2.4.2). We also note that over the pack ice region proximate to the artefact (from 130°E to 145°E and from 65°S to 67°S), there is a large underestimation of ice concentration
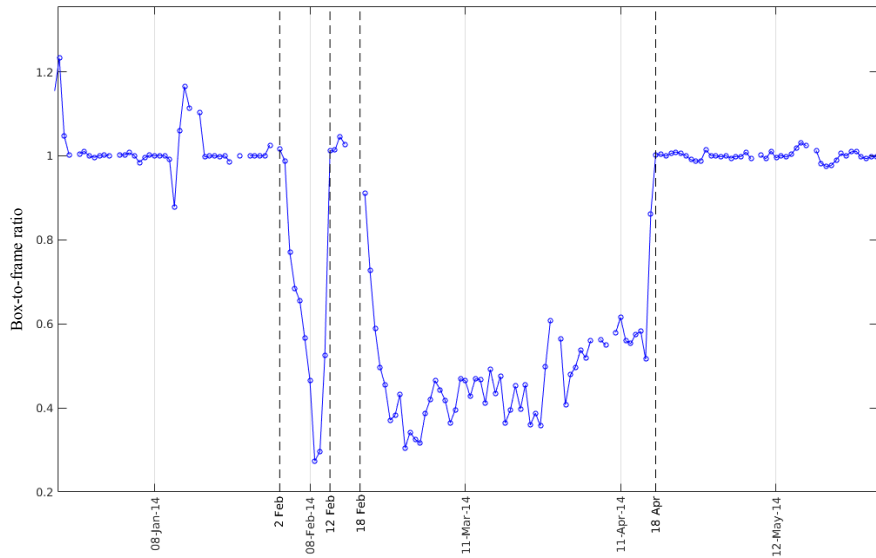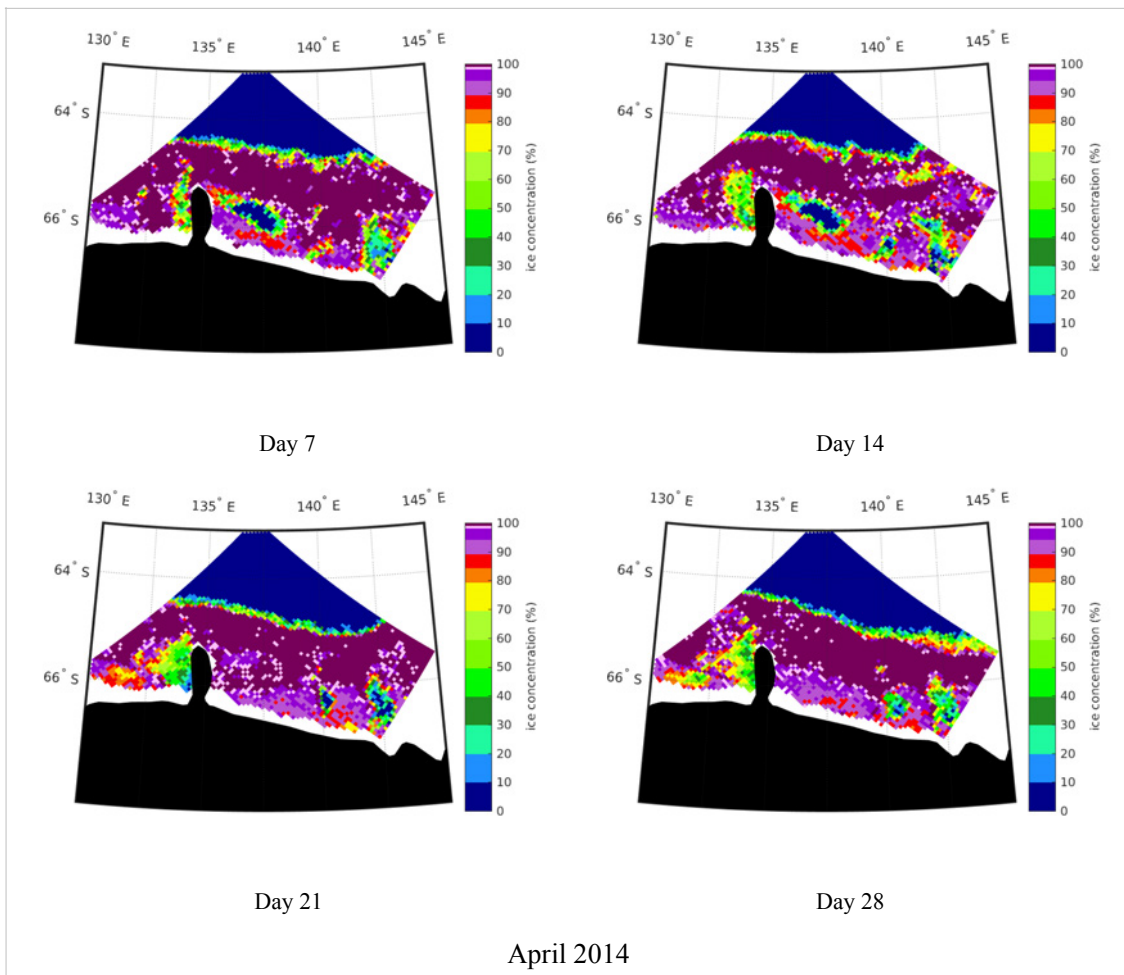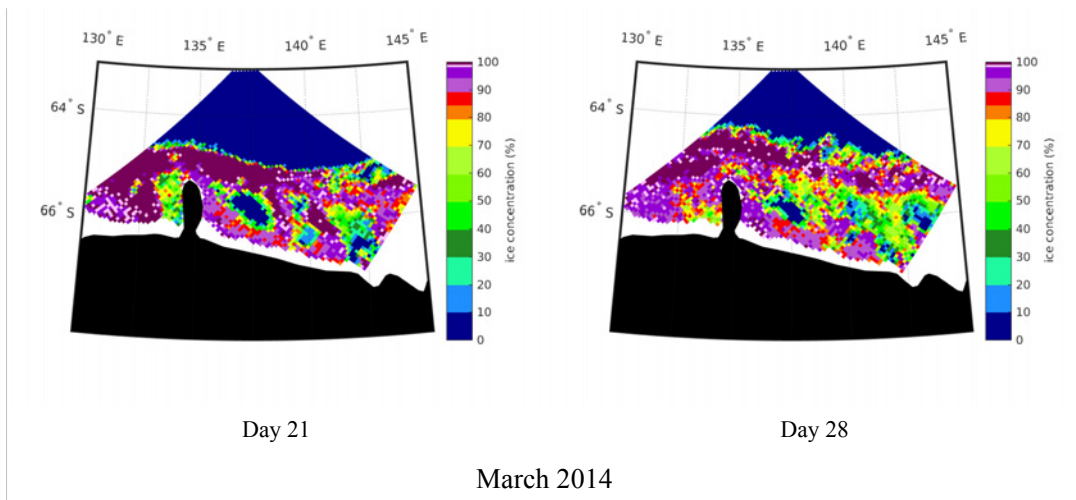
Figure 3.5 A zoom-in of Figure 3.4(b) during January to May 2014. Vertical dashed lines indicate the key dates listed in Table 3.2.

by the Bootstrap algorithm in February, and a slight underestimation in March, when compared to the ASI ice concentration maps.

There is an exception during 12 to 18 February, when the agreement between the ASI and the Bootstrap ice concentrations is high. This would explain the disappearance of the artefact from the ASI maps, as the Bootstrap filter was not triggered at the location of the artefact during this period. The extent of these underestimations by the Bootstrap algorithm is not a localized event, but is apparent over a larger region. We will see later that the periods of underestimation coincide with fluctuations of air temperature below the melting point of sea ice, while during the period of agreement the air temperature was above the melting point (Section 3.4.3).
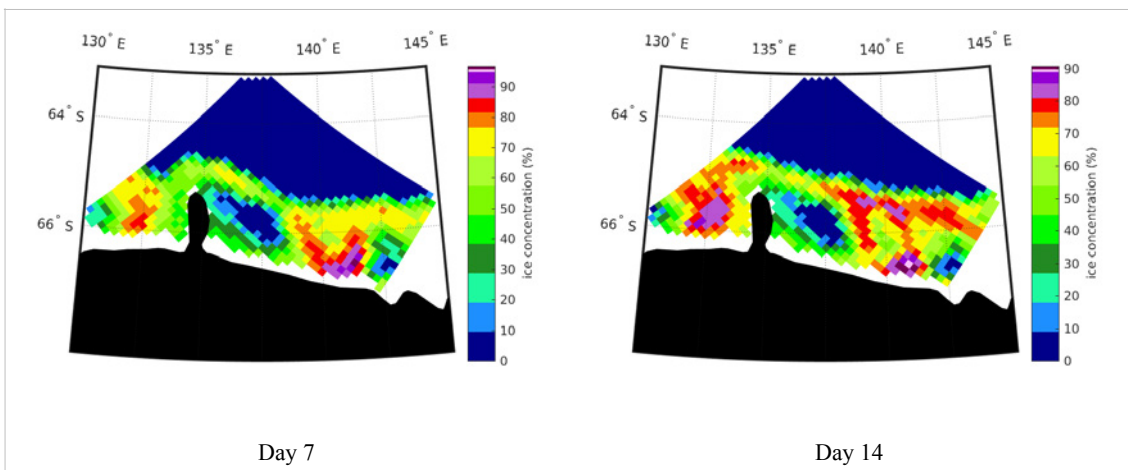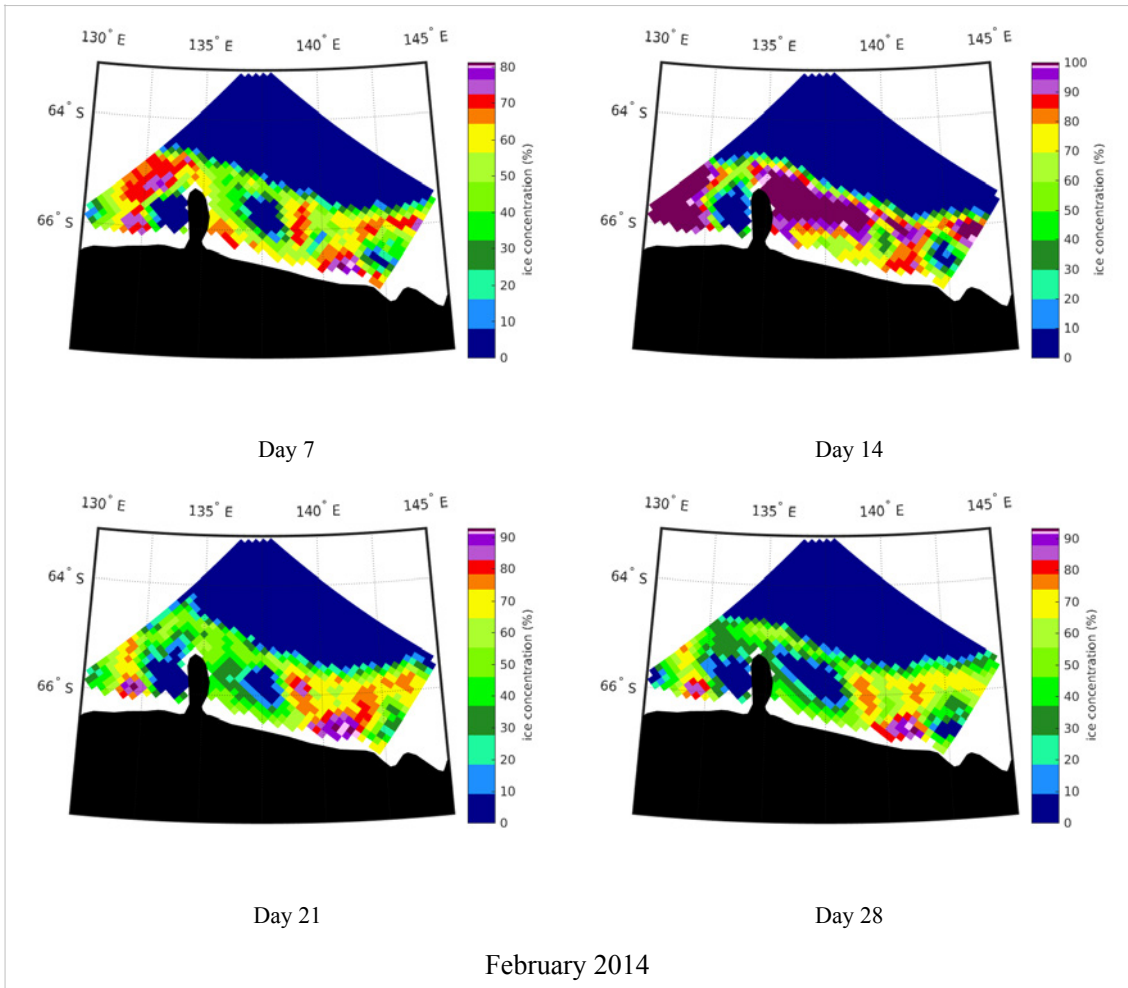
25

Day 7

Day 14

Day 21

Day 28

February 2014

Day 7

Day 14

Day 21   **Day 28**

March 2014

Day 7   **Day 14**

Day 21   **Day 28**

April 2014

Figure 3.6   Weekly ASI ice concentration maps from February to April 2014.

27

We can also conclude from the time series of the Bootstrap box-to-frame ratio (Figure 3.7) that there is no previous occurrence of the artefact at the studied location in the Bootstrap ice concentration maps from 2003 to 2011. In 2013 there is a slight drop of the ratio, with a trend similar to that in 2014. The Bootstrap ice concentration maps from 2013 were inspected, and it is found that February to May there has been underestimation of ice concentration by the Bootstrap algorithm at the location of the artefact when compared to the respective ASI ice concentration maps (Figure 3.9). However, in 2013, the Bootstrap ice concentration at the location fluctuates between 40 to 75%, which is not low enough to trigger the Bootstrap filter. Hence the artefact did not appear on the ASI ice concentration maps in 2013.
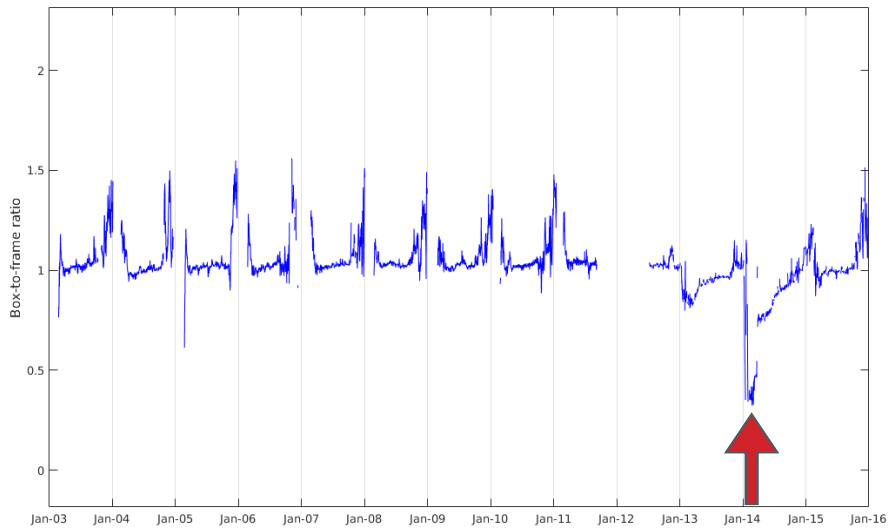
Figure 3.7   Time series of the Bootstrap box-to-frame ratio at the artefact during 2003 to 2016, with the 40% ice concentration threshold set to eliminate summer melts. Red arrows indicate the period of the occurrence of the artefact in 2014.
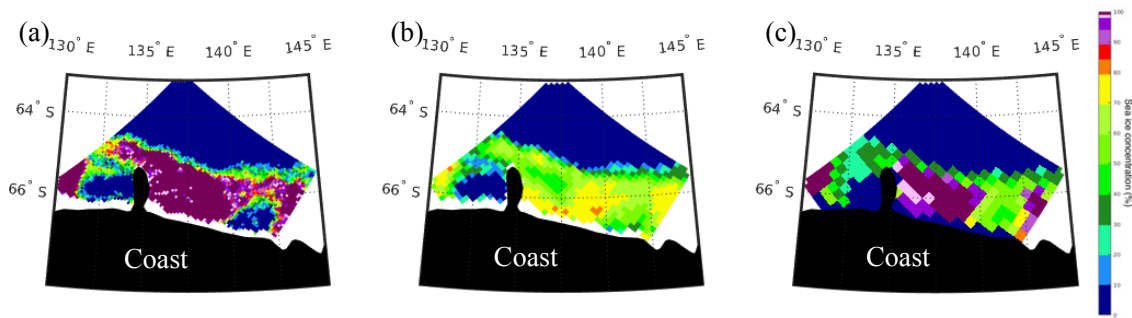
In addition, ice concentration maps derived by the Bootstrap algorithm using the SSMR and SSM/I datasets during the studied period were inspected. It is found that at the location of the artefact, there is also an open water area in these maps (Figure 3.10(a)). This indicates that the occurrence of the artefact is not limited to the AMSR-2 sensor, but is evident in the measurement by other sensors as well. However, an inspection of the maps derived by the revised NASA Team algorithm (NTA; Figure 3.10(b)) and the OSISAF hybrid algorithm (Figure 3.10(c)) shows that the artefact was absent. A possible explanation is that NTA uses gradient ratio (GR) of various channel

Day 7

Day 14

Day 21

Day 28

February 2014

Day 7

Day 14

Day 21   Day 28

March 2014

Day 7   Day 14

Day 21   Day 28
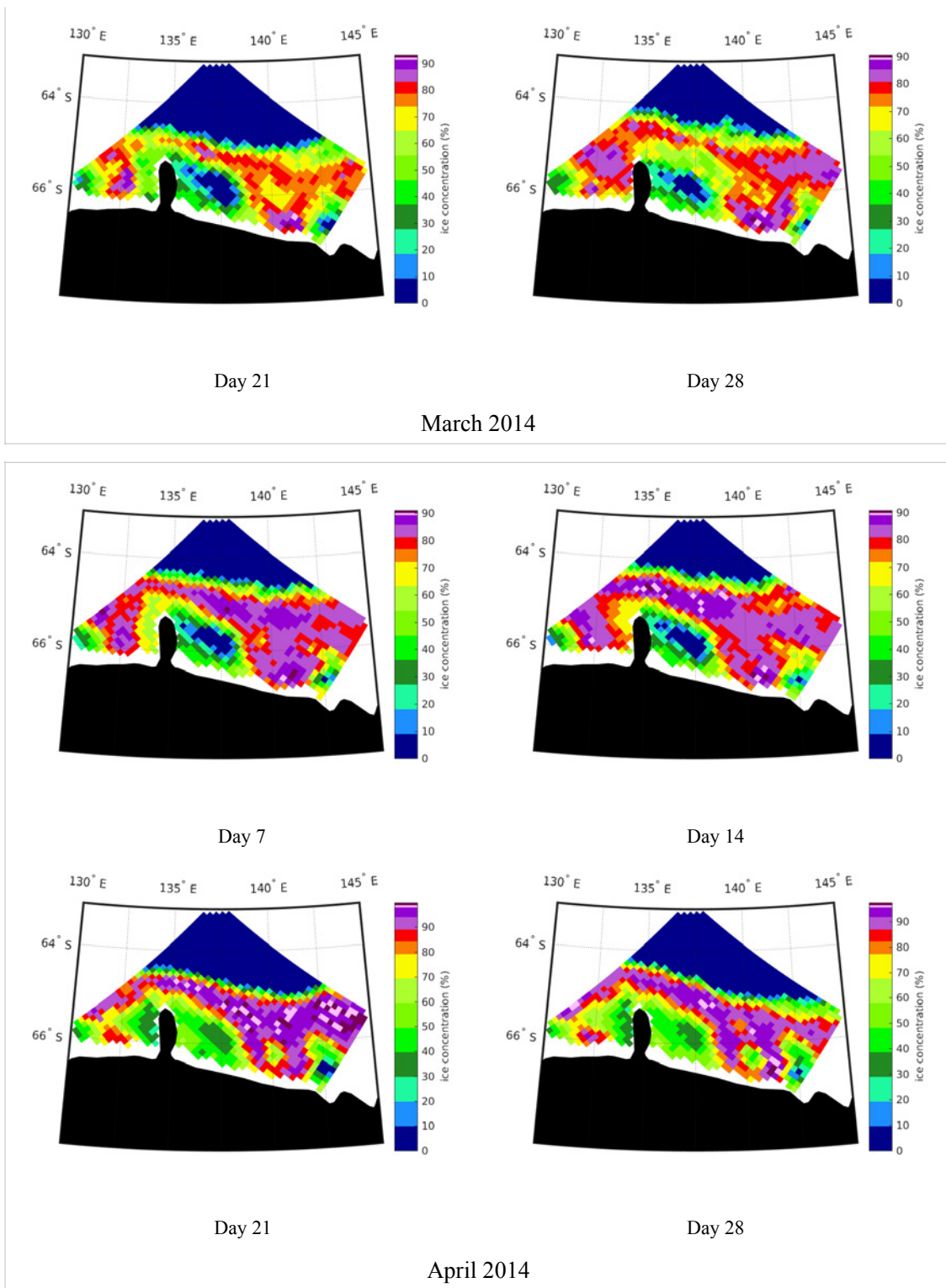
April 2014

Figure 3.8   Weekly Bootstrap ice concentration maps from February to April 2014.

Figure 3.9   Ice concentration maps of 20 February 2013, using (a) ASI algorithm, (b) Bootstrap algorithm with AMSR-2 dataset, and (c) NSIDC Bootstrap algorithm with SSM/I dataset.

combinations to better estimate low ice concentrations; and the OSISAF hybrid algorithm, for ice concentration below 40%, calculates a weighted value using both Bootstrap and Bristol algorithm, such that any erroneous open water pixels interpreted by the Bootstrap algorithm is partly compensated by the Bristol concentration. We also note that when compared to the ASI ice concentration and the MODIS image, which show close to 100% concentration at most of the ice-covered pixels, ice concentrations retrieved by the other algorithms show general underestimation by 40 to 60% (Figure 3.10). The difference is significant and spatially wide-spread. The reason for this remains unclear and would require further investigations.
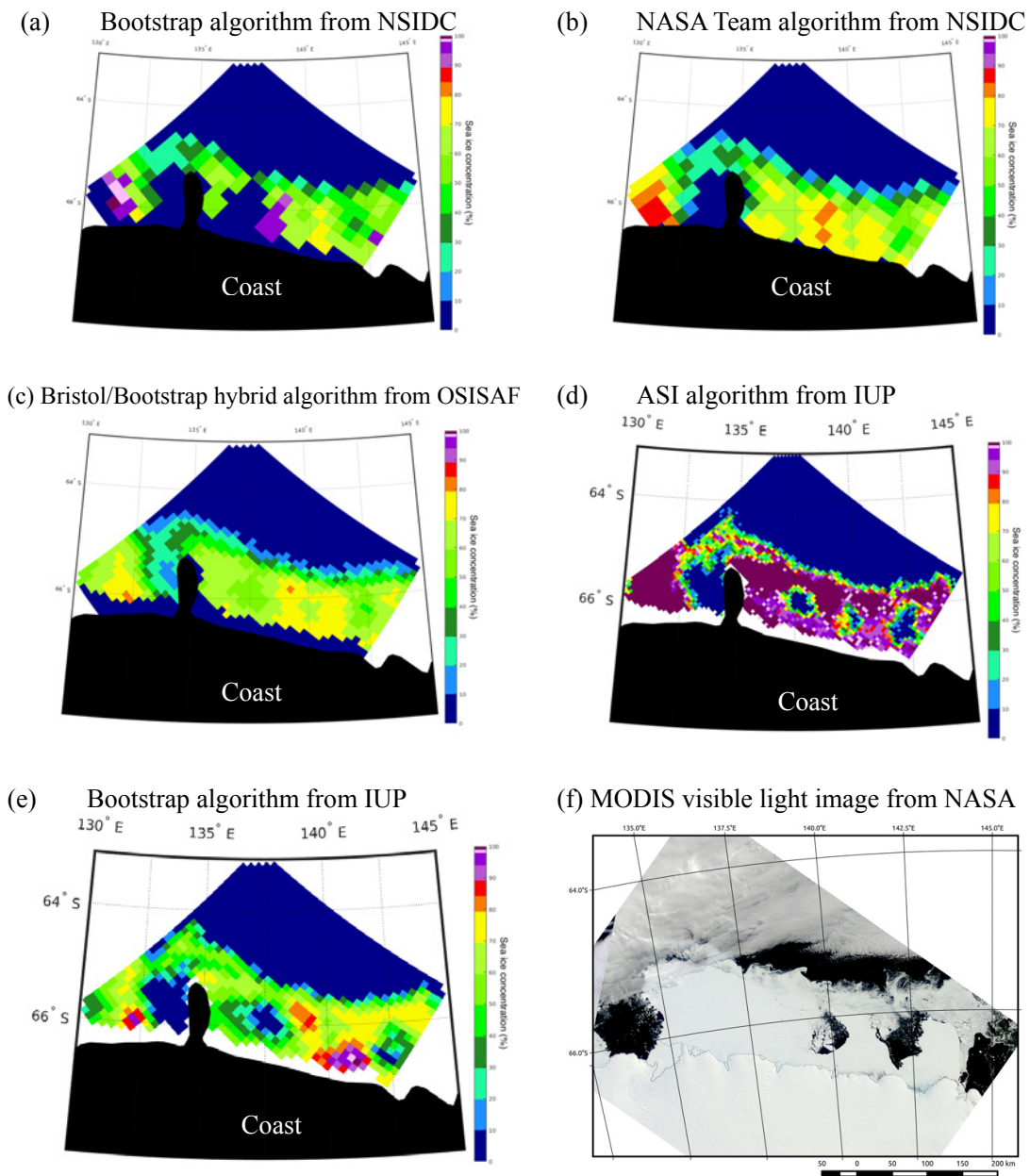
Overall, the analysis of the alternative ice concentration maps suggests that the artefact is related to the retrieval by the Bootstrap algorithm, but not of the dataset. Certain phenomena have caused misinterpretations in ice concentration retrieval in the form of the artefact and as an underestimation of ice concentration as compared to the ASI retrieval.

3.4   Investigation into the artefact using environmental proxies

In an attempt to account for the occurrence of the artefact and to hypothesize the mechanisms behind, several physical parameters in the area, namely brightness temperature, air temperature, snowfall events, bathymetry, and wind velocity, were inspected.

3.4.1   Brightness temperatures

Since brightness temperature is the underlying parameter used by the ASI algorithm to retrieve ice concentrations and to filter out weather effects, the changes in brightness temperature at 18.7, 36.5, and 89.0 GHz in both vertical and horizontal polarization at the location of the artefact were examined.

(a) Bootstrap algorithm from NSIDC

(b) NASA Team algorithm from NSIDC

(c) Bristol/Bootstrap hybrid algorithm from OSISAF

(d) ASI algorithm from IUP

(e) Bootstrap algorithm from IUP

(f) MODIS visible light image from NASA

Figure 3.10 A comparison of ice concentration maps on 20 February 2014 by various algorithms. (a) to (c) use SSM/I dataset; (d) and (e) use AMSR-2 dataset; and (f) is a MODIS visible light image.

To evaluate any changes in brightness temperatures in connection to the artefact, a nearby area, where the artefact has not been observed, is defined as a reference area. This area (2×5 pixels on the ASI grid, 390.625 km^2 in ground spatial size) is centred at 135°45'27''E 66°40'25''S, east of Dibble Iceberg Tongue and near to the coast (Figure 3.2).
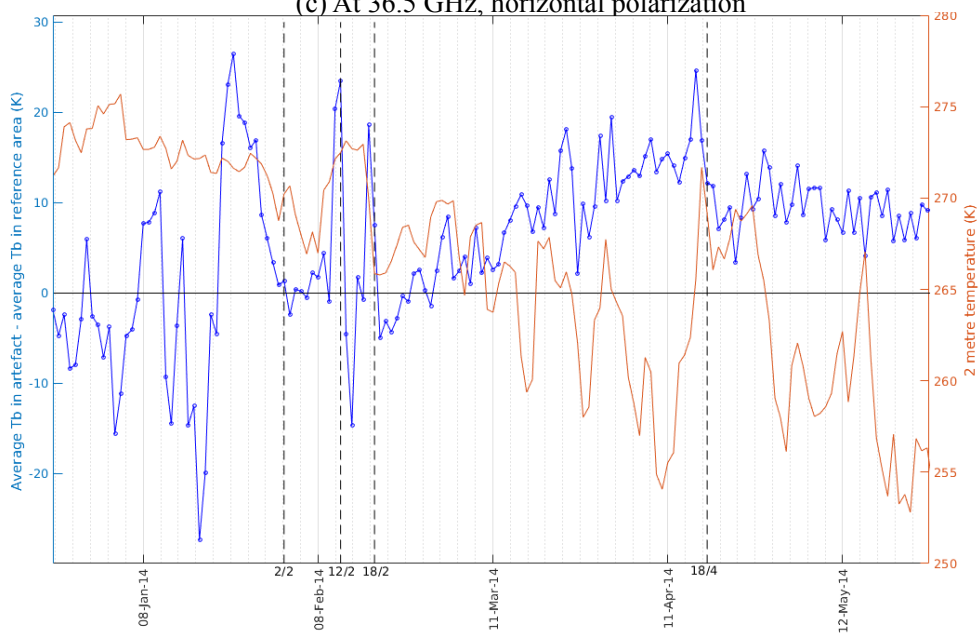
The difference between the average brightness temperature within the artefact and that within the reference area at each channels in both polarizations are plotted in Figure 3.11. The plots for the absolute averages at the two sites are included in Appendix A.3. We can see that for all the six cases the differences fluctuate. In particular, since the beginning of March the differences are steadily positive for the 18.7 and 36.5 GHz channels in both polarizations, meaning that the average brightness temperatures are consistently higher within the artefact than in the reference area. The differences at 89.0 GHz fluctuate around zero, and the absolute averages in the artefact and that in the reference area follow similar trends (Appendix A.3). This could be related to the errors observed in the Bootstrap retrieval, as the algorithm uses the brightness temperature in the 18.7 and 36.5 GHz channels to estimate ice concentration. In addition, all trends have peaks and troughs that follow the fluctuations in 2 metre temperature. This is expected as brightness temperature is a function of the physical temperature, with a multiplication factor of the emissivity. That the magnitudes of the rises and falls in brightness temperature and in 2 metre temperature do not match indicates that the emissivity at each frequency is subjected to variations as well, due to surface changes and atmospheric fluctuations.

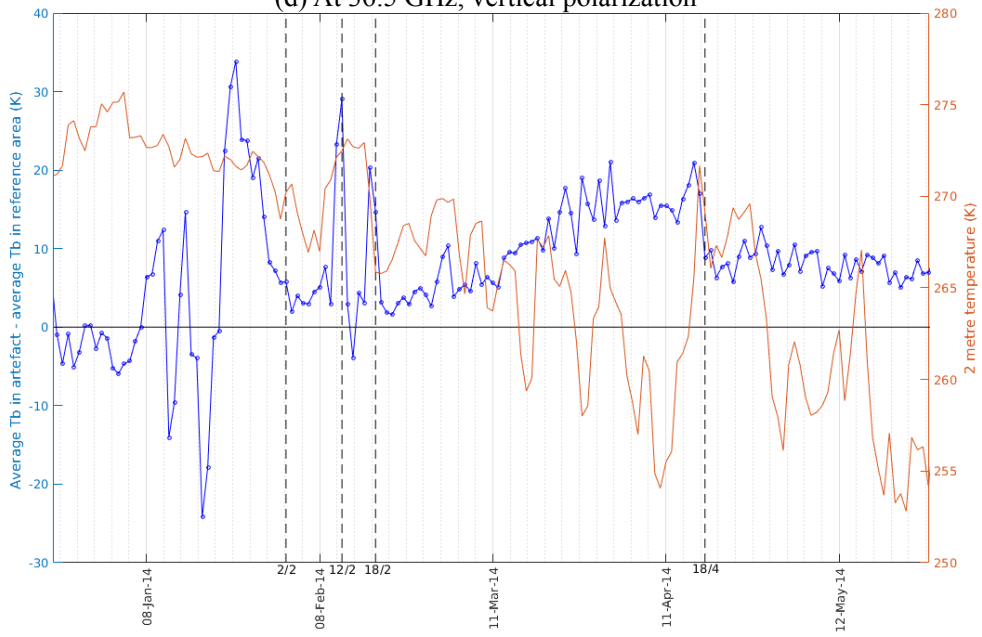(a) At 18.7 GHz, horizontal polarization
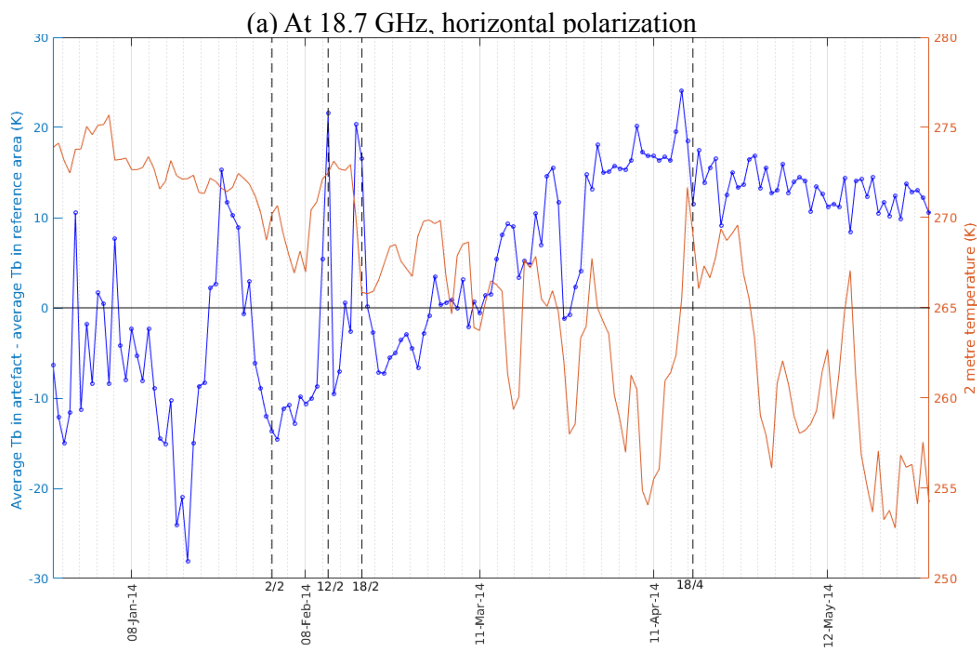
(b) At 18.7 GHz, vertical polarization
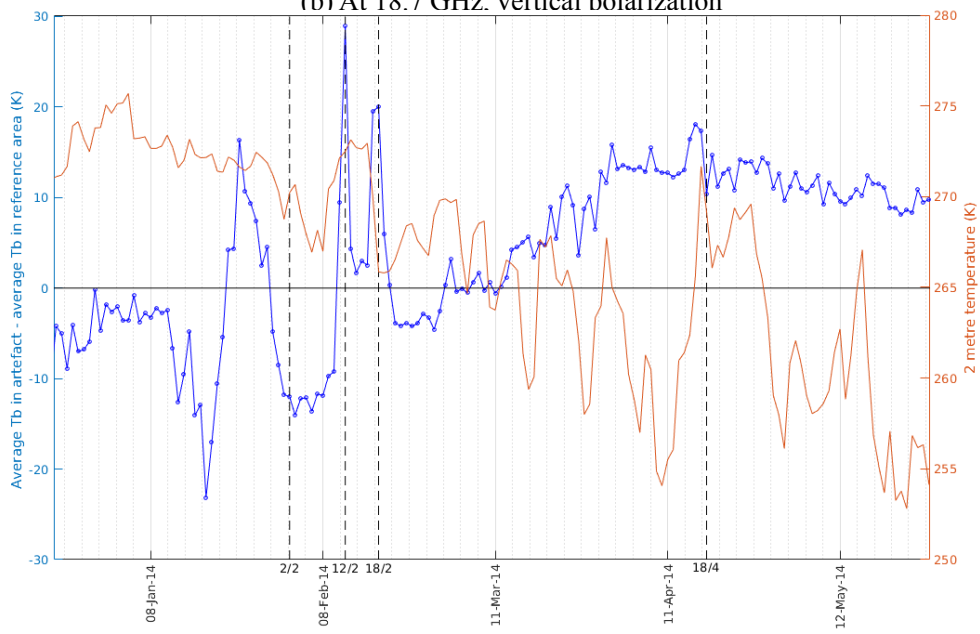
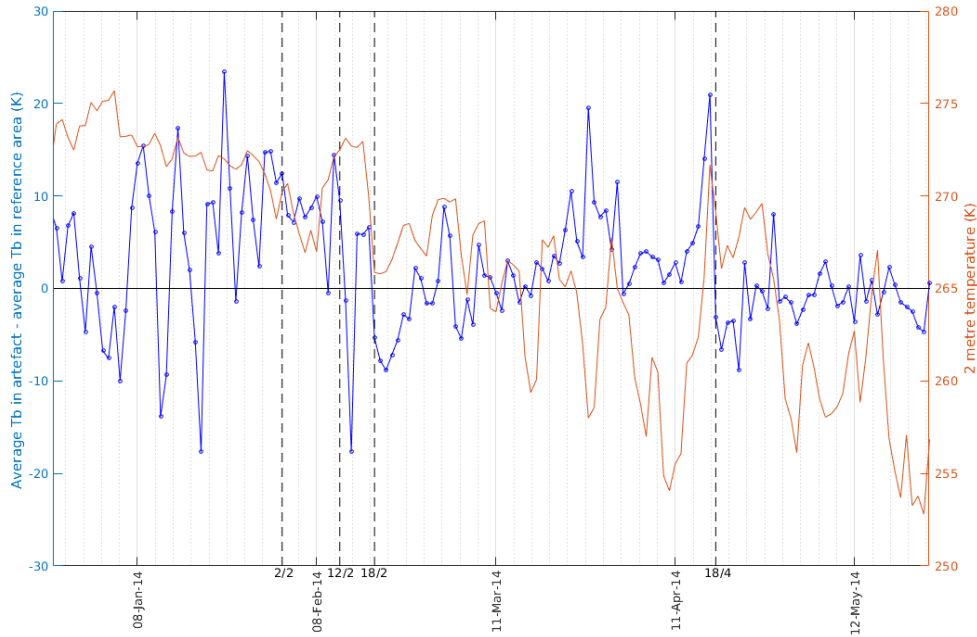(c) At 36.5 GHz, horizontal polarization

(d) At 36.5 GHz, vertical polarization

(e) At 89.0 GHz, horizontal polarization

35

(f) At 89.0 GHz, vertical polarization

Figure 3.11 Time series of the difference ($T_{B\ avg,\ artefact} - T_{B\ avg,\ reference}$) in average brightness temperature between the artefact and the reference area (indicated in Figure 3.2) at various channels during January to May 2014. H and V stand for horizontal and vertical polarization, respectively. Horizontal black solid line on each graph indicates 0 K on the left axis. Dashed vertical lines indicate the key dates listed in Table 3.2.

3.4.2   Effect of weather filters

To better understand the effect of the weather filters on ice concentration retrieval and their potential contribution to the occurrence of the artefact, the Bootstrap filter and the weather filters, GR(36.5/18.7) and GR(23.8/18.7), in the ASI algorithm were manipulated using built-in switches in the algorithm script. The following six cases were investigated and the corresponding time series of the "box-to-frame ratio" were plotted (Figure 3.12).

1.   All filters on (Figure 3.12(a))

This is the original plot of the "box-to-frame ratio", using ASI algorithm with Bootstrap filter and the two weather filters. As noted before, there is a rapid drop and return during the first half of February 2014, followed by a drop from unity that persisted until mid-April 2014.

2.   Bootstrap filter off; both weather filters on (Figure 3.12(b))

The Bootstrap filter was turned off for this iteration, while both weather filters were kept on. We see a smaller drop in the beginning of February 2014, and another smaller drop during March and April. During mid-February, when the artefact was not observed on the ASI ice concentration maps, the ratio returned to around unity.

On the corresponding ice concentration maps derived in this case, the size of the artefact is notably smaller when compared to Case 1 (Figure 3.14(b)). There is no significant amount of spurious ice in the images (Figure 3.13(b)).

3.   Bootstrap filter off; both weather filters off (Figure 3.12(c))

In the case that all filters were turned off, the "box-to-frame ratio" fluctuates between 0.9 to 1.3, without any significant drops throughout the years of 2013 and 2014. We see no artefact on the ASI ice concentration maps throughout the studied period (Figure 3.14(c)). However, there are huge amounts of spurious ice occur on the open ocean (Figure 3.13(c)). This is expected as cloud influence becomes obvious without the application of any filters.

4.   Bootstrap filter off; GR(23.8/18.7) filter on; GR(36.5/18.7) filter off (Figure 3.12(d))

There is a noticeable drop of 0.2 in the ratio in the beginning of February 2014, and a slight negative deviation from unity between March and April 2014. On the ice concentration maps derived, the artefact only occurred on three occasions (9 February, 2 March, 3 March) from February to April 2014, and in these occasions the sizes of the artefact are considerably smaller than those in Case 1 (Figure 3.14(d)). Significant amounts of spurious ice on the open ocean persisted during the period (Figure 3.13(d)).

5.   Bootstrap filter off; GR(23.8/18.7) filter off; GR(36.5/18.7) filter on (Figure 3.12(e))

The time series of the ratio resembles the shape in Case 2. As in Case 2, the size of the artefact observed is noticeably smaller than that in Case 1 (Figure 3.14(e)). Spurious ice on open oceans is negligible (Figure 3.13(e)).

6.   Bootstrap filter on; both weather filters off (Figure 3.12(f))

The time series of the ratio resembles the shape in Case 1. The sizes of the artefact are comparable to those in Case 1 (Figure 3.14(f)). We can see some spurious ice, but in smaller amounts than those in Case 3 and 4 (Figure 3.13(f)).

Table 3.3 Summary of the effect of the Bootstrap filter and the weather filters on the occurrence of the artefact

Case	Filters			Number of occurrence of the artefact*	Spurious ice on open ocean**
	Bootstrap	GR(23.8/18.7)	GR(36.5/18.7)		
1	On	On	On	68	Negligible
2	Off	On	On	60	Negligible
3	Off	Off	Off	0	Extensive
4	Off	On	Off	3	Extensive
5	Off	Off	On	60	Negligible
6	On	Off	Off	66	Regional

*Number of occurrence of the artefact is counted during the period of 1 February to 30 April 2014 (Total number of days: 89).
**The appearance of spurious ice on open ocean, beyond (north of) the ice extent of the day is determined by visual inspection.

Two cases have been neglected, namely the counterparts of Case 4 and 5 with the Bootstrap filter "on". This is because preliminary inspection on the corresponding results at the studied location show no difference to those in Case 4 and 5. Although in both of the neglected cases, spurious ice over open ocean is greatly reduced. This demonstrates the effect of the Bootstrap filter in the ASI algorithm (Section 2.4.2).

We can see that the Bootstrap filter and the GR(36.5/18.7) weather filter contribute the most to the occurrence of the artefact (Table 3.3). When the Bootstrap filter and the GR(36.5/18.7) filter are turned off, the number of occurrence of the artefact reduces drastically from 68 to 3 (only on 9 February, 2 and 3 March) during the studied period, and in the cases that it appears, its size is considerably smaller than when all filters are turned on. In Case 3, where all filters are switched off, the artefact disappears completely, but spurious ice occurs extensively over the open ocean, indicating the importance of the weather filters on ice concentration retrieval.

The results suggest that apart from the Bootstrap filter, the GR(36.5/18.7) weather filter may also have been related to the occurrence of the artefact. Figure 3.15 shows the plots of the maximum gradient ratio GR(36.5/18.7) among the pixels in the artefact (red) and in the reference area (blue). The curve for the artefact is consistently higher than that for the reference area. We note that during the time when the artefact appeared (2 to 12 February and 19 February to 18 April), the maximum GR(36.5/18.7) in the artefact exceeds the threshold value of 0.045 (above which the pixel is set to be ice-free). This could be one of the changes that resulted in the occurrence of the artefact, which we will look into detailedly in Section 3.5.
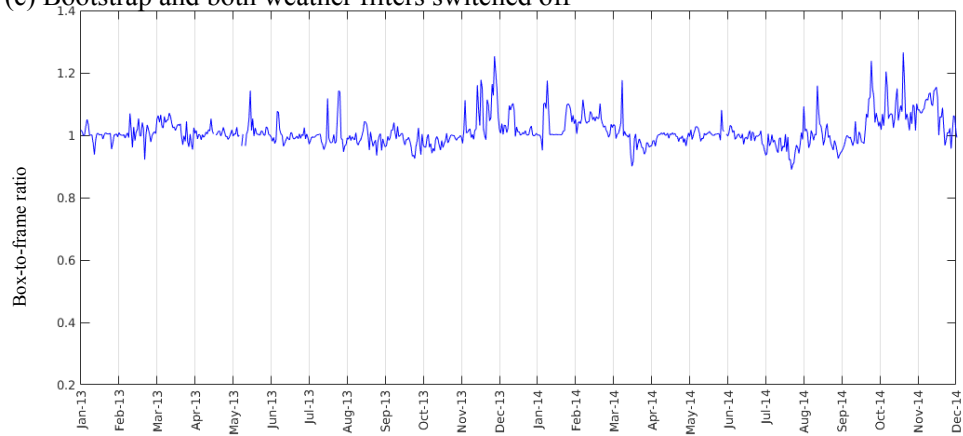
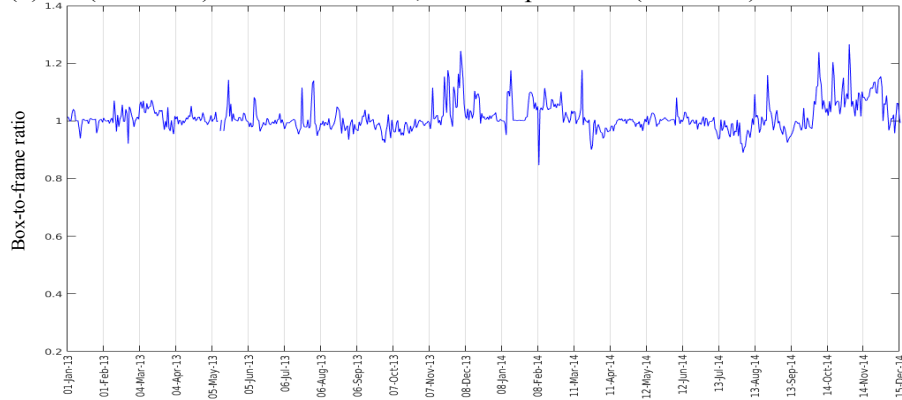(a) Bootstrap and both weather filters switched on
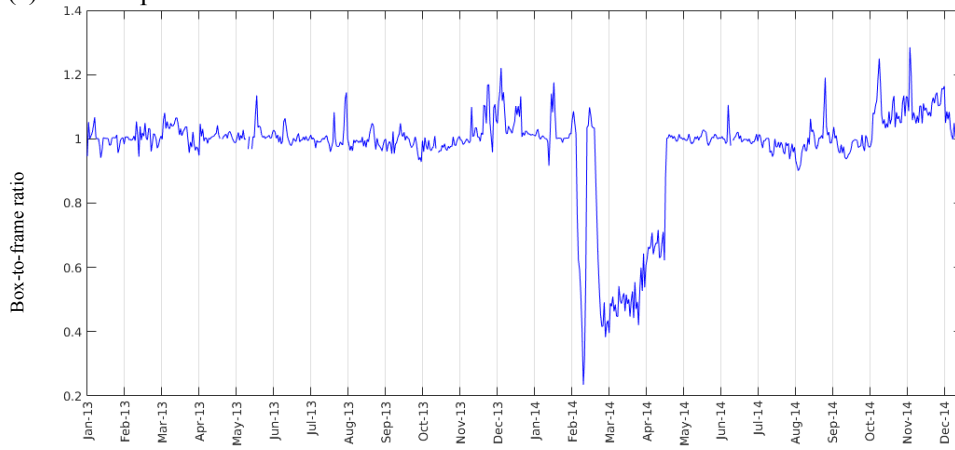
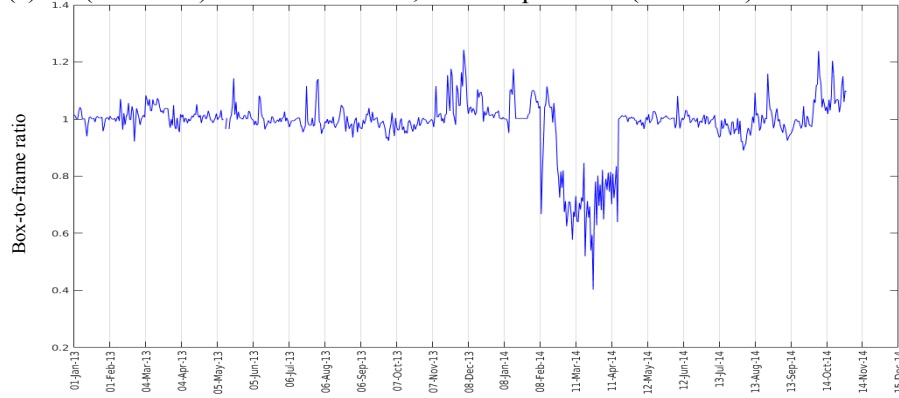(b)Bootstrap filter switched off; both weather filters switched on
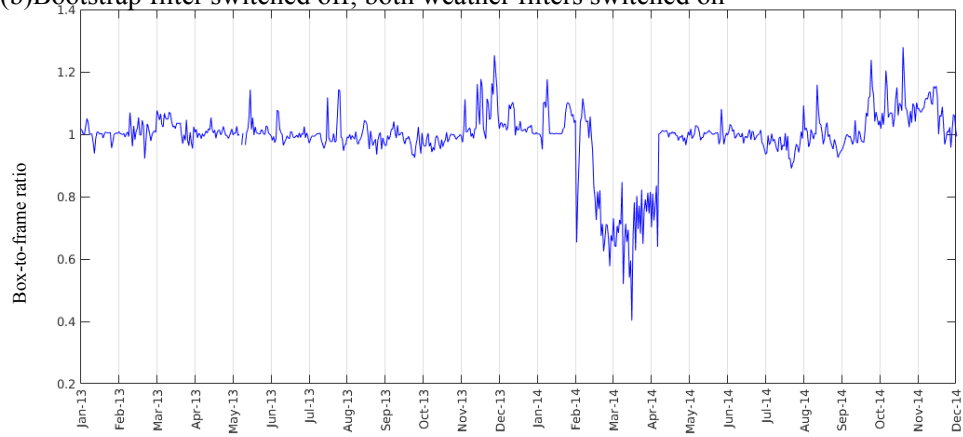
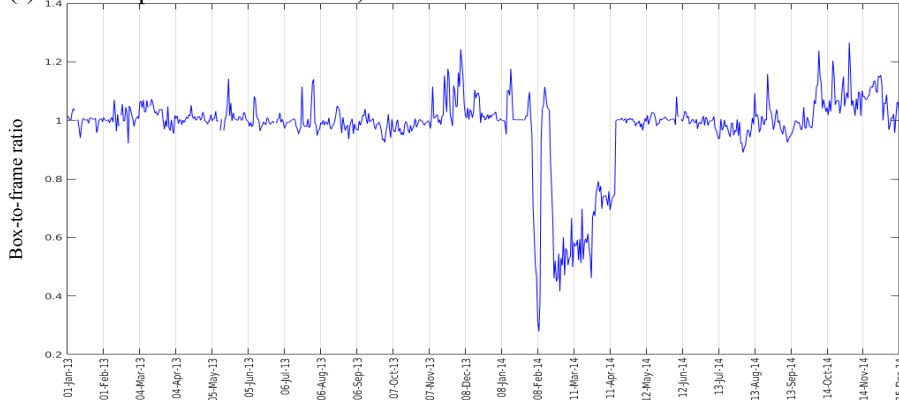(c) Bootstrap and both weather filters switched off

(d) GR(23.8/18.7) filter switched on; Bootstrap and GR(36.5/18.7) filters switch off


(e) GR(36.5/18.7) filter switched on; Bootstrap and GR(23.8/18.7) filters switch off
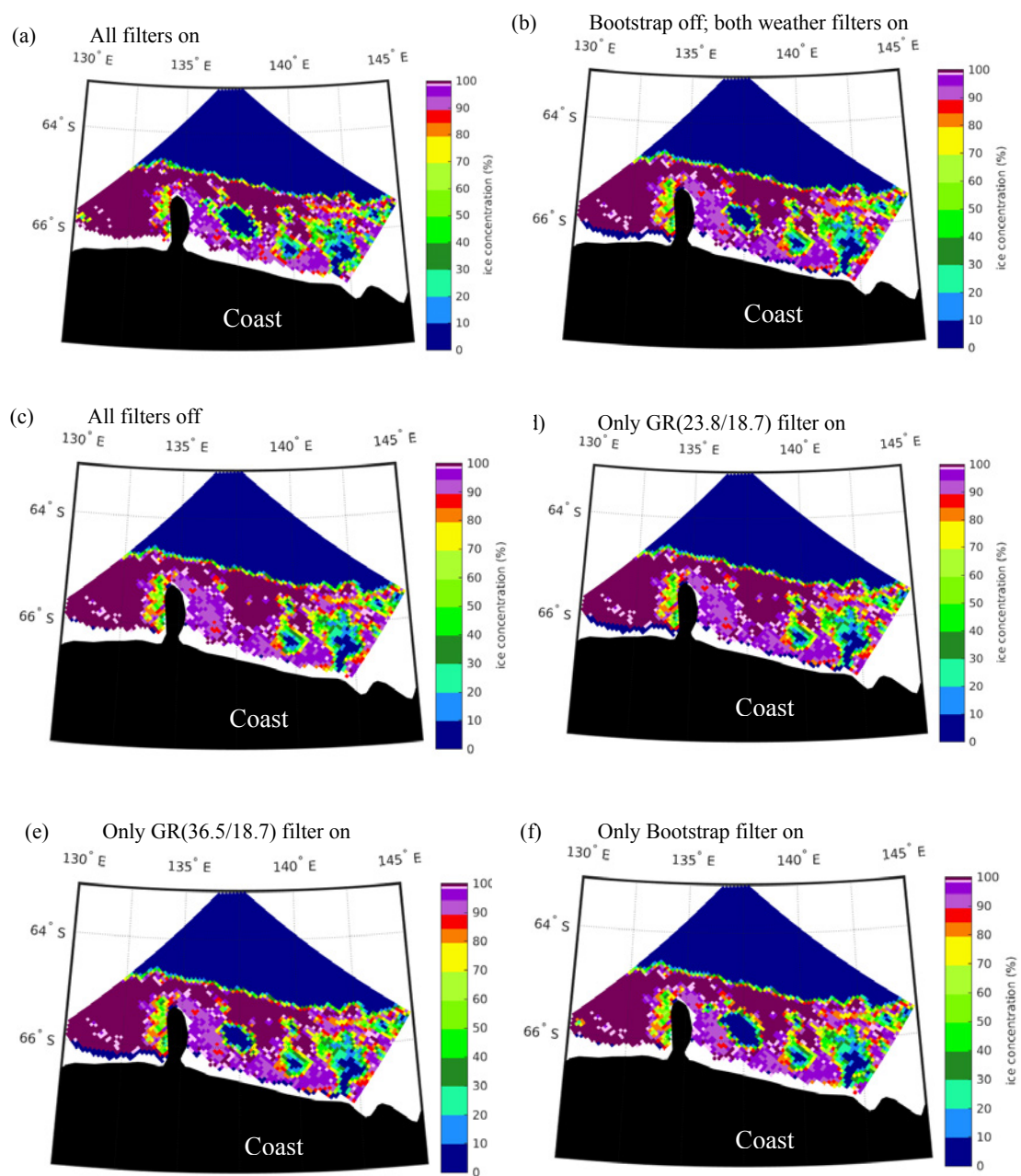

(f) Bootstrap filter switched on; both weather filters switch off

Figure 3.12   Time series of the box-to-frame ratio at the artefact in the case of: (a) Bootstrap filter and both weather filters on; (b) Bootstrap filter off but both weather filters on; (c) all filters off; (d) only GR(23.8/18.7) filter on; (e) only GR(36.5/18.7) filter on; and (f) only Bootstrap filter on.
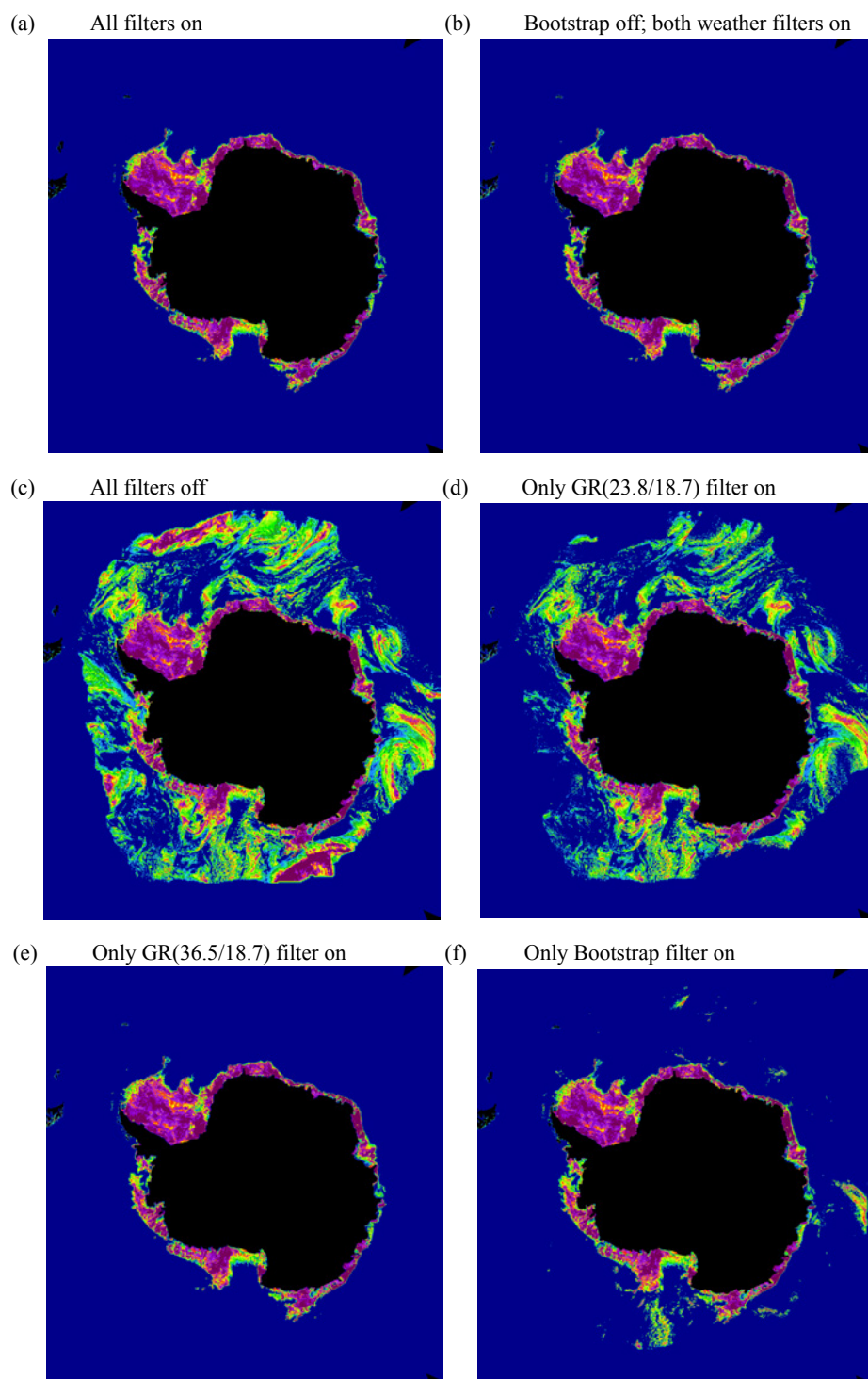
Figure 3.13   Examples of ASI ice concentration maps (on 15 March 2014) of the whole Antartica in the case of: (a) Bootstrap filter and both weather filters on; (b) Bootstrap filter off but both weather filters on; (c) all filters off; (d) only GR(23.8/18.7) filter on; (e) only GR(36.5/18.7) filter on; and (f) only Bootstrap filter on.

Figure 3.14   Examples of ASI ice concentration maps (on 15 March 2014) of the studied area in the case of: (a) Bootstrap filter and both weather filters on; (b) Bootstrap filter off but both weather filters on; (c) all filters off; (d) only GR(23.8/18.7) filter on; (e) only GR(36.5/18.7) filter on; and (f) only Bootstrap filter on.
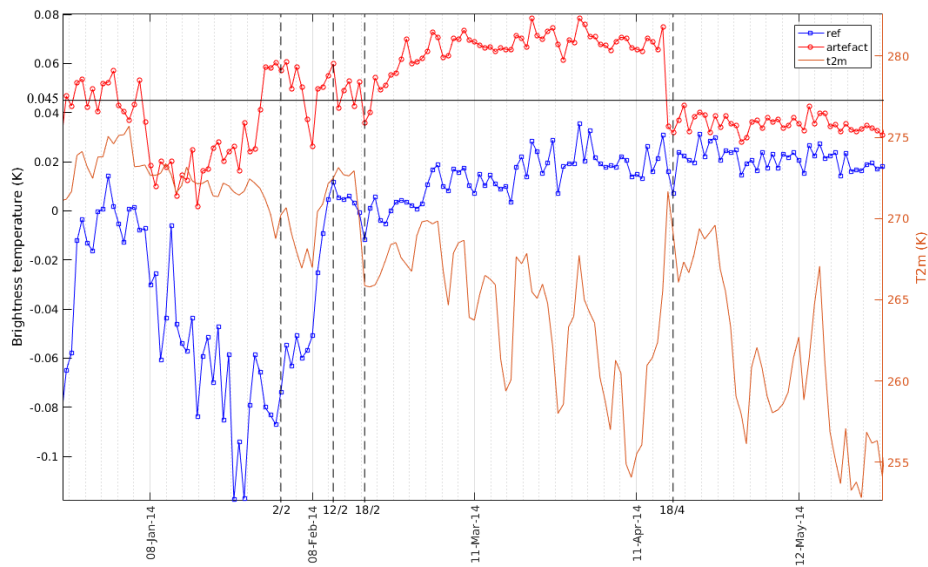
Figure 3.15 Time series of the maximum gradient ratio GR(36.5/18.7) among the pixel in the artefact (red circles) and in the reference area (blue squares) during January to May 2014 (Section 3.5.1). Horizontal black solid line indicates the threshold of 0.045 used by the GR(36.5/18.7) filter in the ASI algorithm. Orange curve shows the 2 metre temperature of the area on the right axis. Dashed vertical lines indicate the key dates listed in Table 3.2.

3.4.3 2 metre temperature (T2m)

The calculated box-to-frame ratio is plotted together with the time series of ECMWF T2m (Section 3.2) at the location of the artefact (Figure 3.16). Starting from 27 January 2014, there was a consistent drop from 272 K to 268 K until 2 February, when the artefact first appeared. T2m then fluctuated below 271.2 K, until 10 February when it raised above 271.2 K. On 14 February it reached 273 K. From 11 to 17 February, the sudden increase in ASI algorithm-derived ratio coincides with a rise in temperature above 271.2 K, which is a common value of the melting point of sea ice. This suggest melt-refreeze process of snow may be related to the occurrence of the artefact. After 17 February there was a significant drop in T2m, and it remained fluctuating below 271.2 K, with a minimum of 254 K recorded on 10 April. From then the temperature steadily raised to 272K on 17 April, after which it decreased and fluctuated below 271.2 K.

43
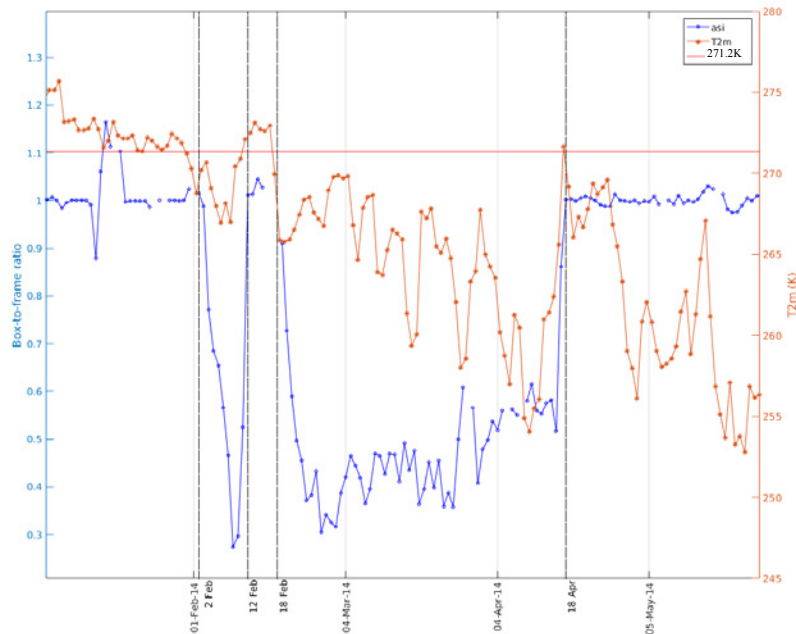
Figure 3.16   Time series of box-to-frame ratio (blue circles; left axis) and that of the 2 metre temperature (orange asterisks; right axis) at the artefact during January to May 2014. Horizontal red line shows 271.2 K on the right axis. Dashed vertical lines indicate the key dates listed in Table 3.2.

3.4.4   Snow and precipitation effect

Snowfall is common in Antarctica, as a result from the passage of synoptic storms, such that newly formed sea ice usually acquires snow cover within days. Allison (1993) observed from a cruise expedition that sea ice thicker than 15 cm always had a snow cover. ERA-Interim reanalysis data from ECMWF (Dee et al., 2011) indicates that there were significant increases in snowfall on 29 January, 10 February, and 16 April (Figure 3.17), the latter two cases coinciding with rises in air temperature, and in both cases the disappearance of the artefact has followed. These snowfall events would cause an accumulation of snow cover on ice. When the environmental conditions (e.g., air temperature, wind pattern) change, snow cover metamorphoses and causes changes in emissivity of the surface (Section 2.3.3).

3.4.5   10 metre wind

For 10 metre wind data, since one grid (0.75°×0.75°) is sufficient to cover the area of the artefact, the grid overlapping the artefact was identified. The wind components in this grid are plotted in a time series, together with the 2 metre temperature, as shown in Figure 3.18.

44
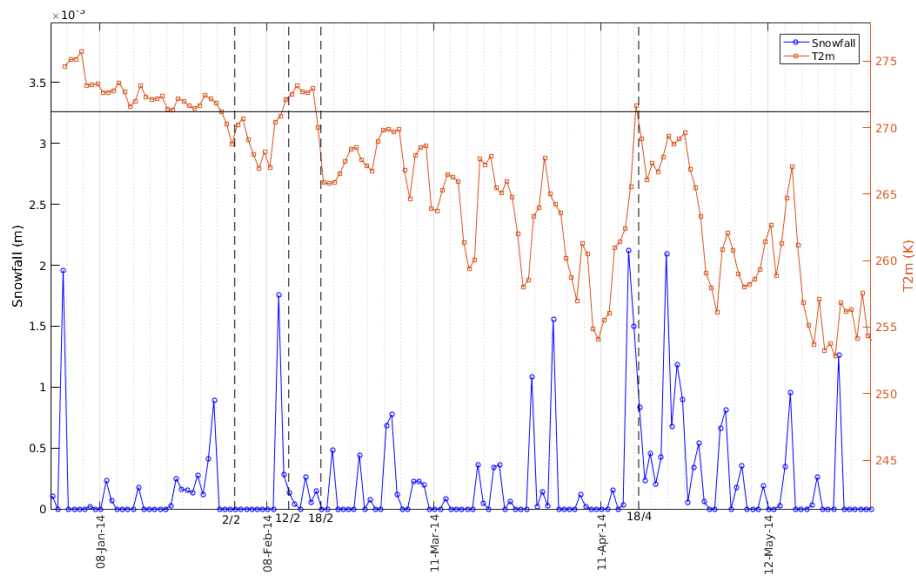
Figure 3.17   Time series of snowfall (blue circles) and 2 metre temperature (orange squares) at the artefact during January to May 2014. Horizontal black solid line indicates the temperature of 271.2 K on the right axis. Dashed vertical lines indicate the key dates listed in Table 3.2.
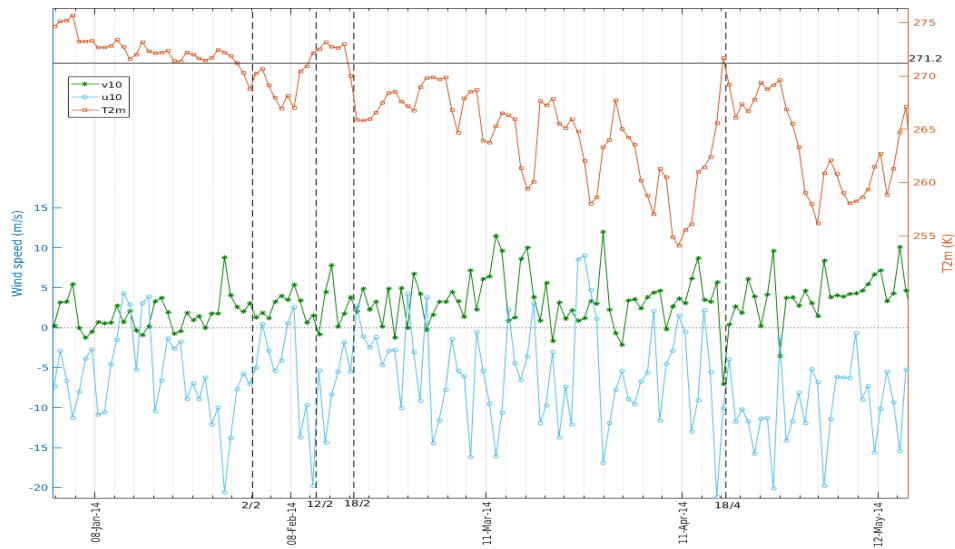

Figure 3.18   Time series of the U component (light blue circles) and the V component (green asterisks) of 10 metre wind, and 2 metre temperature (orange squares) at the artefact during January to May 2014. Horizontal black dotted line shows zero on the left axis. Horizontal black solid line indicates the temperature of 271.2 K on the right axis. Dashed vertical lines indicate the key dates listed in Table 3.2.

45

3.4.6   Bathymetry

The bathymetry map (Figure 3.19) and the vertical profiles (Figure 3.20) of the studied area were created. In Figure 3.9, the magenta contour lines representing 60% ASI ice concentration, used to outline the approximate location and extent of the artefact on 9 February 2014. Figure 3.20 shows the vertical profiles from 67°S to 64°S, along the longitude lines from 136°E to 138°E at 0.5° intervals. Red double-headed arrows show the approximate extent of the artefact as observed on the image of 9 February 2014.

We observe that the artefact is centred at a trough, just north of 66°S, of maximum depth of about 1000 m, surrounded by elevated bed of depth from 0 to 200 m. The northern side of the trough is bounded by a steep continental slope that advances southward towards the east. As the trough widens towards the east, the artefact extends towards the south (the coast). From Figure 3.19, channels connecting the troughs to the open ocean can be observed.
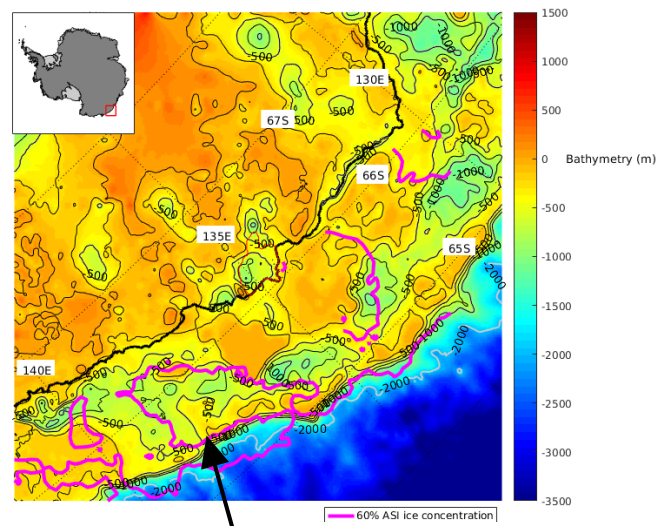
Figure 3.19   Bathymetry of the studied area. Black contour lines are at 250 m intervals from 0 to -1000 m. Thick black line represents the coast. Pink lines represents the contour of ASI ice concentration of 60% on 9 February 2014, and black arrow indicates the position of the artefact on that day.
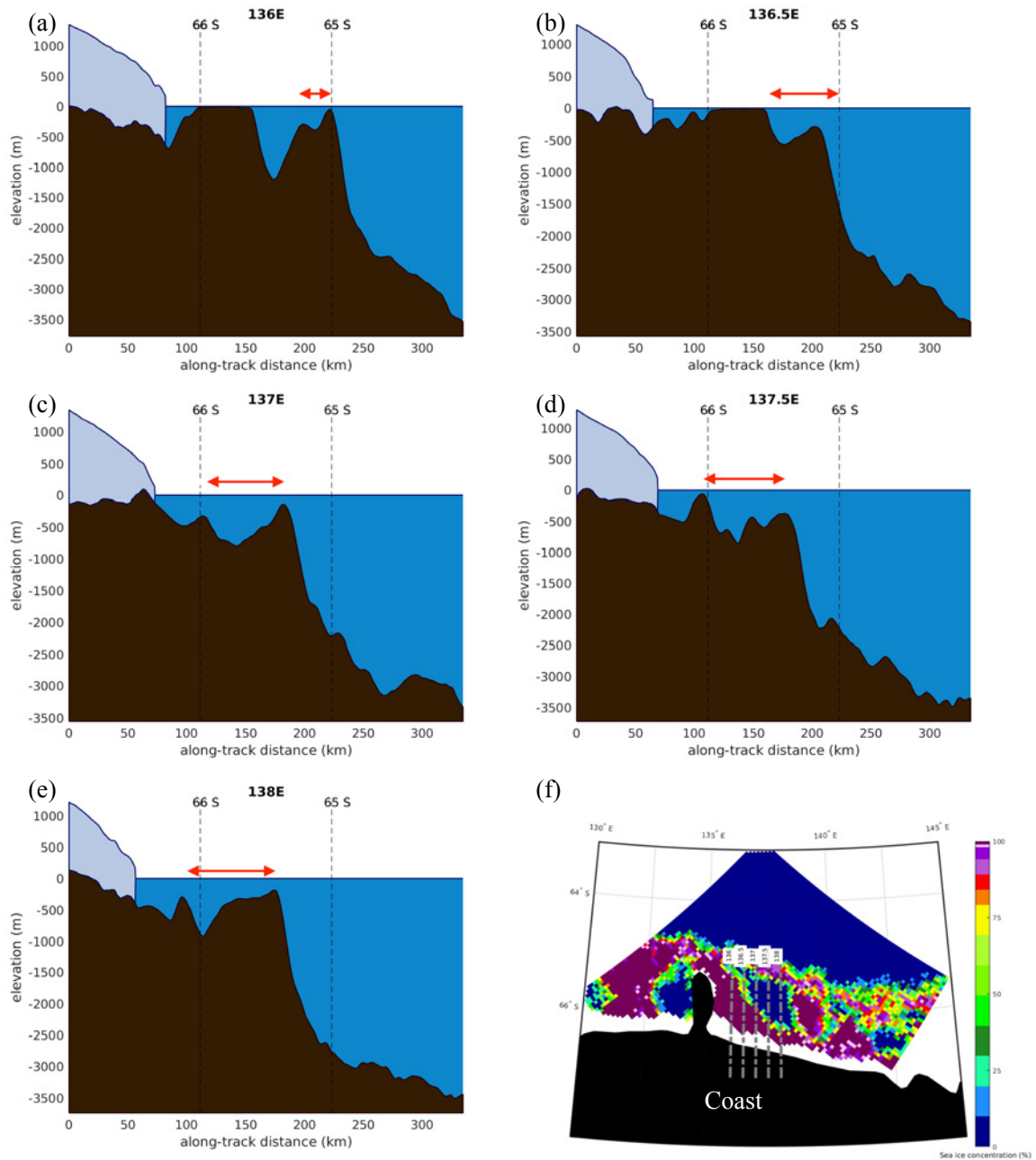
Figure 3.20 (a) to (e): Bed profiles of the studied area between 64°S to 67°S, along the longitudinal lines (a) 136°E, (b) 136.5°E, (c) 137°E, (d) 137.5°E, and (e) 138°E. Blue color represents open water; light blue the Antarctic ice sheet; and black the Earth's crust. Double-headed red arrows show the extent of the artefact on each profile on 9 February 2014.

(f) Ice concentration map on 9 February 2014. Grey dashed lines show the tracks along which the profiles (a) to (e) are drawn.

3.5   Discussion

We have seen that there exists contradictions between the visible images from MODIS and the ice concentration retrieved by the ASI and Bootstrap algorithm using the AMSR-2 dataset, and Bootstrap algorithm using the SSM/I dataset. We also observe that other algorithms such as NTA and OSISAF Bristol/Bootstrap hybrid algorithm, in some cases, underestimate ice concentration with respect to visible image and ASI ice concentration. The occurrence of the artefact is of profound significance. For instance, surface heat flux from ocean to air would be significantly overestimated in region of artefact where retrieved ice concentration data indicates open water, but in reality is covered by sea ice, which acts as a physical barrier that hinders heat exchange. It could also undermine the validity of ice concentration maps in operational uses, such as ship navigation. As we are not certain if the artefact discovered is a single occurrence, or if there exists other similar artefacts, it is important to understand what could have caused such phenomenon.

Potential causes of the artefact

The specific events and factors that have led to the artefact might not be trivial, as there was no available *in situ* data, neither from field measurement nor ship observation, of the sea ice in the area during that period. Thus there is no "ground truth" to validate the satellite data with. Nevertheless, the MODIS images could serve as a reference to the actual phenomenon happening in the area; over the studied time period, we see no polynya in the MODIS images at the studied location, where the ASI ice concentration maps from the studied period (February to April 2014) are showing open water pixels (Figure 3.1).

Alternative ice concentration dataset were also studied. Incidentally, the Bootstrap ice concentration maps using AMSR-2 data also show the artefact at the same location in 2014 (Figure 3.8), as well as underestimation (but no erroneous open water pixels) of ice concentration at the location from February to May 2013 (Figure 3.9). Bootstrap maps from the National Snow and Ice Data Center (NSIDC) using SSM/I dataset also present the artefact in 2014, but the maps created by the NASA Team algorithm and the OSISAF Bristol/Bootstrap hybrid algorithm, using the same SSM/I dataset, do not show any open water artefact, although a general underestimation with respect to the ASI algorithm is observed. We also note that the three alternative datasets (Bootstrap SSM/I from NSIDC, NTA SSM/I from NSIDC, and Bristol/Bootstrap hybrid SSM/I from OSISAF) do not have the sufficient resolutions to resolve the real polynyas along 140°E and along 142.5°E (Figure 3.10). Lastly, this study is limited to the specific studied location, other regions in Antarctica have not been investigated.

In addition, other physical parameters were studied in an attempt to formulate possible reasons to the occurrence of the artefact. There are several factors that would affect the microwave signature of sea ice. Such factors could contribute individually and/or interdependently to the artefact observed.

3.5.1   Snow cover

Snow on sea ice could have significant and prompt effects on microwave signature, particularly during melting and refreezing. Markus and Cavalieri (2006) pointed out that snow wetted during the day frequently refreezes during the night. Such refreezing leads to increase in grain sizes (Colbeck, 1982) and reduces emissivity at 36.5 GHz relative to 18.7 GHz by enhanced scattering within the frozen top layer of snow cover (Onstort et al., 1987; Mätzler, 1994). This would lower the gradient ratio GR(36.5/18.7), used in a weather filter in the ASI algorithm. On the other hand, upon the melting or wetting of snow, both the 18.7 and 36.5 GHz channels have emissivity that approaches unity (that of a blackbody), and the gradient ratio GR(36.5/18.7) approaches zero, before becoming positive (Markus and Cavalieri, 2006). This gradient ratio is positive for water but near zero or negative for ice, and is primarily used to filter out cases of high cloud liquid water by setting a threshold higher than which the pixel will be regarded as totally ice-free (Spreen et al., 2008). Thus, when the snow cover on ice is wetted either by flooding of seawater and/or by melting, GR(36.5/18.7) will increase. If it exceeds the threshold, the filter will be triggered and the pixel will be reported as ice-free by the ASI algorithm, even though it is actually snow-covered ice. Moreover, flooding can also occur at the snow-ice interface (Section 3.5.1.1), which would not affect the appearance of the snow layer from a top-view, and would appear in MODIS images as snow/ice covered.

Figure 3.15 supports this speculation. The threshold of GR(36.5/18.7) in the ASI algorithm is set at 0.045, above which the pixel will be regarded as ice-free. The time series of GR(36.5/18.7) shows that during most part of the period from mid-February to mid-April 2014, the maximum value for the reference area is below the threshold, while the maximum within the area of the artefact is for most of the period above the threshold, most notably and consistently between 18 February and 18 April. This indicates that some pixels in the artefact area have above-threshold values of GR(36.5/18.7), and are therefore represented as open water pixels. Thus the increase in GR(36.5/18.7), possibly caused by wetted snow, could be a reason that the artefact is observed during the period.

49

3.5.1.1 Possible causes of snow wetting

A main reason for snow wetting is the melting of surface snow. Although the time series for 2 metre temperature (Figure 3.16) shows that the air temperature was at times below-freezing throughout the studied period, it is possible for snow metamorphism to occur at below-freezing temperature, in which the snow crystals change shape due to the absorption of solar radiation by snow (Colbeck, 1989; Launiainen and Cheng, 1998). This could affect the microwave signals from the surface. Fresh snow cover, which has high air content, also acts as an insulator to trap heat and can warm up the subsurface snow/ice layers due to its low thermal conductivity (Pomeroy and Brun, 2001). Haas et al. (2001) noted that at sub-zero temperatures, which were typical at the studied location during the studied period, subsurface snow melting is sufficient to foster extensive snow metamorphism, and to form a surface ice layer when the wetted snow refreezes.

Another possible reason for snow wetting is flooding of the surface by sea water. As snow accumulates on the surface, its mass can submerge the underlying ice into the water; subsurface melting can also lead to ice submergence, due to increased brine volumes and therefore higher bulk densities (Haas et al., 2001).

3.5.2   Temperature

Since brightness temperature is a function of physical temperature, changes in surface temperature would also cause fluctuations in microwave signal. Moreover, induced melting and refreezing of snow on ice due to variation in air temperature could cause changes in emissivity and thus brightness temperature, as discussed before.

In the time series of 2 metre temperature, appearance of the artefact coincides with drops in temperature while its disappearance with rises in temperature approaching the melting point (Figure 3.16). These provide necessary conditions for melt-refreeze process to have occurred during the episode of the appearance and the disappearance of the artefact. Melt-refreeze process is a valid cause for the variation in the gradient ratio GR(36.5/18.7) as mentioned in Section 3.5.1.1.

3.5.3   Bathymetry

From Figures 3.19 and 3.20, we see that the artefact is located at a bathymetric trough. While the trough widens towards the east, the artefact extends towards the south (the coast). It is possible that water influx from the open ocean emerge through cracks on sea ice and caused flooding of the snow cover on top. This would be enhanced if the weight of snow cover is sufficient to decrease the freeboard of the ice (i.e. submerging it into water).

The bathymetry of the area appears to be correlated with the location of the artefact. One postulation is that the rising slope at the southern wall of the trough would guide the water influx upwards, and the uneven bedform may induce turbulence on the incoming water flow, thereby thinning the sea ice thermodynamically from the bottom, making the region more susceptible to surface flooding caused by the weight of snow cover. When there is sufficient snow cover accumulated on ice, it will weigh down the ice, such that flooding of the snow cover becomes possible. However, to investigate the existence of such phenomenon, ocean current measurements and modelling in the area are required.

3.5.4 Wind effect

From Figure 3.18, the V component of 10 metre wind fluctuates above zero, indicating a dominant northward component of the wind in the area, which is mostly due to offshore katabatic wind. The U component shows greater variations, and is biased to the negative (east to west). This is due to the westward deviation of the offshore katabatic wind by Coriolis force. However, there is no observable pattern in the wind speed components during the key events (refer to Table 1). Still, it is likely that there is an indirect contribution from wind or interdependent effects with other parameters. Wind can bring changes to air temperature and redistribute snow cover in an area, both of which would affect the melt-refreeze process of snow cover on ice. When the wind is onshore, it carries warmer air over the open ocean to the coast, near where the artefact is located. In contrary, offshore katabatic wind is usually dry and cold. Accelerated by the topography inland from the coast, katabatic wind can bring down the air temperature in the area of the artefact. Moreover, wind could increase snow cover by bringing snow flakes from nearby snowfall events, and could redistribute the snow cover that is already on the ice.

4   Possible solutions and further work

In this section, some possible solutions to remove the artefact from the ASI derived images are discussed (Section 4.1). Further work is proposed to help improve our understanding on the occurrence of the artefact, and to devise detection scheme for identifying other artefact occurrence (Section 4.2).

4.1   Solutions to remove the artefact

4.1.1   Localized solution

As a first solution to the occurrence of the artefact, the affected pixels were replaced with an alternative dataset using the ASI algorithm without Bootstrap and GR(36.5/18.7) weather filters. An area of 28×34 pixels was identified (Figure 4.1(a)), in which the artefact occurred during February to April 2014. This area is decided by visual inspection on the images from selected dates when the extent of the artefact is among the largest observed, so as to avoid including the surrounding non-artefact pixels, while making sure that the artefact itself is included in the area throughout the whole period. The pixels in the box from the alternative dataset were compared to their respective counterparts in the original ASI dataset, and the highest value of the two was kept at the corresponding pixel. From this, a new dataset was created and inserted to the dataset of the whole Antarctica. In this way, the artefact is essentially "patched up" using a dataset that is not compromised by potential surface effects on the 18.7 and 36.5 GHz channels.

As pointed out in Section 3.4.2, with the two filters turned off in the new dataset, the artefact appeared 3 times (9 February, 2 and 3 March) throughout the studied period, compared to 68 times in the original images with the filters on. In most of the cases, the new dataset bares higher similarities to the MODIS images than the original dataset does. Figure 4.1 shows some examples of the ice concentration maps at the location before and after the correction, with MODIS images included as reference. We can see that the corrected pictures show better agreement with the corresponding MODIS pictures around 137.5°E 66°S, where the artefact is located before correction. The correction scheme is applied to all 89 original ASI dataset from February to April 2014, and the alternative datasets are created and stored.

From Table 3.3, we can see that when all the filters are switched off (Case 3), no appearance of the artefact is recorded during the study period. However in this case spurious ice frequently occurs along the ice edge, which could undermine the validity of the ice concentration evaluated in

the marginal ice zone. Therefore in this correction scheme, the GR(23.8/18.7) is kept on as a compromise to remove the artefact while maintaining certain degree of weather filtering.
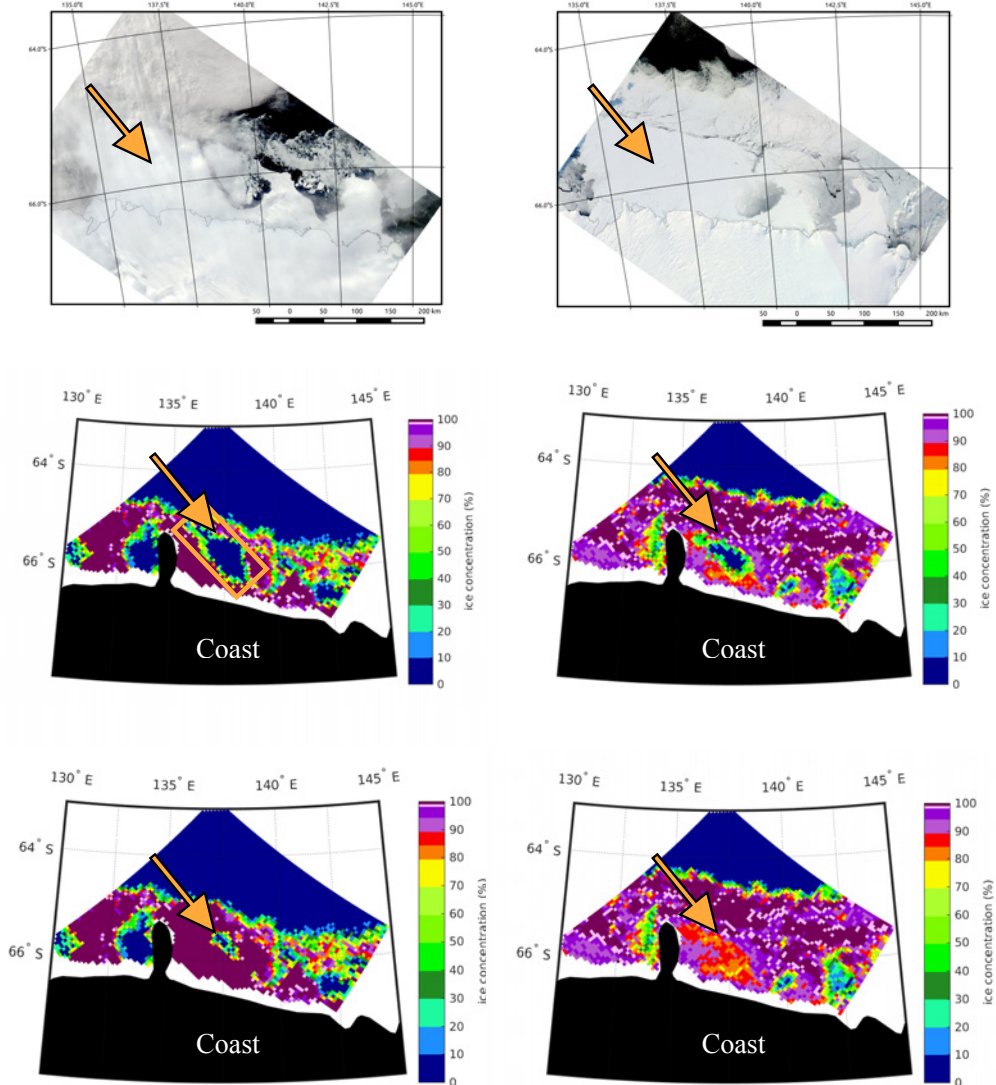
Figure 4.1 Comparisons between MODIS images (*top* row) and ASI ice concentration maps before (*middle* row) and after (*bottom* row) correction, from (a) 9 February 2014; (b) 10 April 2014. Orange box in the second picture of column (a) shows the approximate location of the corrected area.

4.1.2 Proposed solution

Here a more general solution that would also be applicable to potential artefacts in other locations is proposed. This solution has not been implemented in this study due to the limited time for the thesis project. In the following we will see the outline of this solution.

As discussed in Chapter 3, both high cloud liquid water and possible cases of surface wetting may trigger the GR(36.5/18.7) filter. There are three possible scenarios for the filter to be triggered:

1. High cloud liquid water above open ocean

Due to the presence of the high cloud liquid water, the brightness temperature difference at 89 GHz will be smaller, i.e. closer to that of ice. In this case, ice concentration will be reported as above zero in open ocean. The GR(36.5/18.7) filter will be triggered and the ice concentration will be corrected to zero.

2. High cloud liquid water above ice

Due to the higher emissivity of ice over water, the microwave signal from the ice surface dominates that from cloud liquid water, such that the GR(36.5/18.7) filter would not be triggered by cloud liquid water over sea ice. At low ice concentrations, emission from the surface may have similar signal to that from high cloud liquid water over ocean, such that the filter can be triggered. This could potentially set pixels with ice concentration in the range of 1 to 20% to 0%, but the GR(36.5/18.7) filter should have no effect on pixel of ice concentration above 20%, as evident from Figure 2 in Gloersen and Cavalieri (1986).

3. Wetting of ice surface

As pointed out in Section 3.5, e.g., surface wetting could cause changes in emissivity that leads to GR(36.5/18.7) exceeding its threshold in the weather filter. This could result in pixels with non-zero ice concentration being filtered out. The filter is wrongly applied. This solution will attempt to eliminate such cases.

High cloud liquid water cases in the marginal ice zones could potentially be confused with surface wetting cases. High clouds are moving, while surface melting is a local event, so it is expected that a pixel will not have the GR(36.5/18.7) filter turned on by high cloud for a long period, and such cases could be attributed to surface wetting. Moreover, high cloud liquid water

over ice should not affect the retrieval of ice concentration. A pixel of relative high ice concentration within the ice pack should not change to a very low value within a day, which is what happened in the case of the artefact. Thus a potential correction scheme may rely on the ice concentration history of a pixel. Based on the above considerations, the following solution is proposed to decide if the GR(36.5/18.7) filter and the Bootstrap filter should be turned off for a certain pixel. This method aims to create an new dataset in addition to the original retrieval by ASI algorithm.

Step 1: Install a flag (Flag A) in the ASI algorithm script that indicates if GR(36.5/18.7) is above 0.045 (the threshold value) at each pixel (1: above; 0: below).

In the original ASI algorithm, whether a pixel has the weather filters applied is not recorded. Since it is found that the occurrence of the artefact is related to the Bootstrap filter and the GR(36.5/18.7) filter in the ASI algorithm, and that switching off both filters can effectively remove the artefact in most cases, Flag A will be used to decide if the filters should be switched on or off for a pixel.

Step 2: Set a limit using the ice extent of the previous day plus a one-pixel margin

The solution will only be applied within the limit, which consists mostly of the marginal ice zone and the land beyond. Outside this limit is open ocean, where the GR(36.5/18.7) filter and the Bootstrap filter are needed to reduce atmospheric effect.

Step 3: Decide if a pixel will have the filters switched on or off when creating an alternative dataset of the present day.

Before retrieving the ice concentration of the present day, the algorithm will read the ice concentration data from the original datasets of the past seven days. For each pixel, if

(1) Flag A reads "1" for the present day, and

(2) the ice concentration of this pixel is above 80% *in the alternative datasets* for at least four of the past seven days,

then the GR(36.5/18.7) filter and the Bootstrap filter should be switched off for this pixel, as it is suspected that there is surface wetting on the present day. This is repeated for all pixels in the dataset, and the pixels that satisfy the above conditions will be marked by Flag B (1: filters to be switched on; 0: filters to be switched off).

*Step 4: Create the alternative dataset of the present day.*

The ASI algorithm will be run again for the present day, with GR(36.5/18.7) filter and the Bootstrap filter switched off for the pixels that have Flag B reading "0", and switched on for those reading "1". An new dataset will be created as the alternative dataset of the present day.

This method makes the following assumptions:

(1)   Surface wetting on ice will cause GR(36.5/18.7) to increase beyond its threshold value, which requires further confirmation;

(2)   High cloud liquid water over ice has negligible effect on the ice concentration retrieval by ASI algorithm. This can be inferred from the results from Gloersen and Cavalieri (1986), where they showed that applying the GR(36.5/18.7) filter had no effect on pixels with ice concentration above 20%.

Furthermore, the work of PhD student J. Lu of the Institute of Environmental Physics, University of Bremen confirms that cloud liquid water above ice has negligible effect on the polarization difference of brightness temperature at 89 Ghz (Figure 4.2; personal communication, August 15, 2016). It shows the simulation results of AMSR-2 brightness temperature at 89 GHz using the Radiative Transfer Model (Wentz and Meissner, 2000). The model computes brightness temperatures based on environmental parameters such as sea surface temperature, sea surface wind speed, water vapor and cloud liquid water. For each calculation, one parameter is changed within its range, while other parameters are kept at their reference values: 270 K for surface temperature; 250 K for ice; zero for wind speed, water vapor, and cloud liquid water. The green curves show that polarization difference at 89 GHz varies negligibly with cloud liquid water in the range of 0 to 0.8 kg/m^2 is within 10 K over first-year and multiyear ice, while the variation is much larger over water.

(3)   Switching off the Bootstrap filter and the GR(36.5/18.7) filter in the ASI algorithm will eliminate the misidentification of an ice-covered pixel as an open water pixel, which is suggested by the results from this study (see Chapter 3).

(4)   A pixel with a history of relative high ice concentration (> 80%) within the ice pack should not change abruptly into an ice-free pixel within a day.
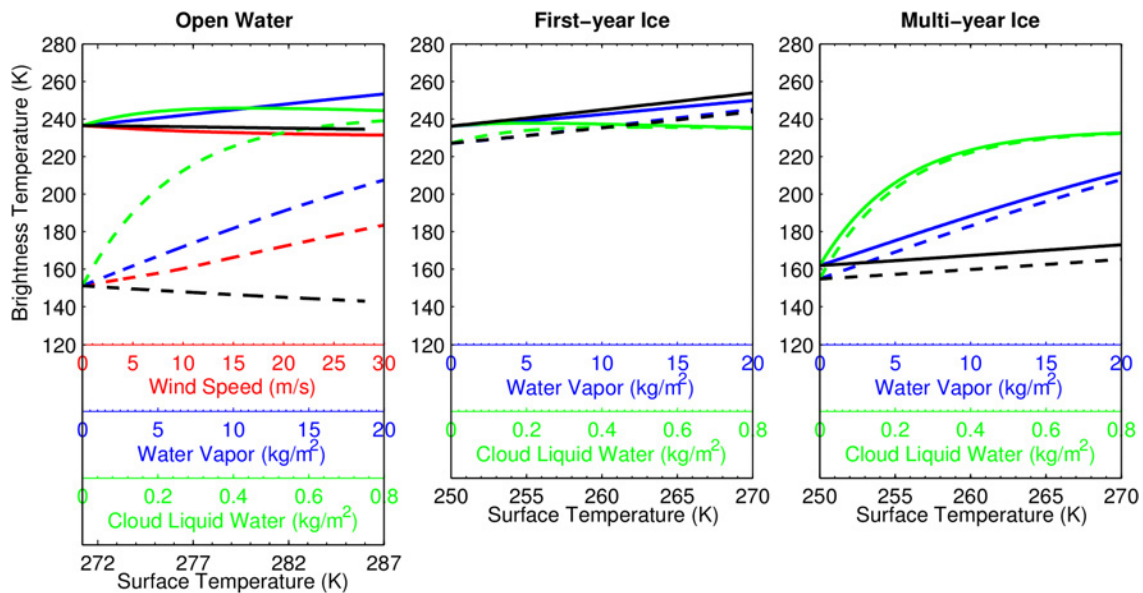
Figure 4.2 Simulated brightness temperature at 89 GHz from radiative transfer model. Dashed and solid lines are at horizontal and vertical polarization, respectively. Colours of the curves correspond to the parameters on the horizontal axis of the same colour. Figure courtesy of J. Lu of the Institute of Environmental Physics, University of Bremen.

Further investigations are needed to derive an ideal correction scheme. For example, the following parameters are subjected to adjustment when the method is implemented:

(1)   The threshold value for GR(36.5/18.7) above which the flag in Step 1 will be set to "1", currently set at 0.045, the same value as the threshold value used in the ASI algorithm;

(2)   The number of previous days to be included as the "history" of a pixel in Step 3, currently suggested to be seven;

(3)   The minimal number of days that a pixel will have high ice concentration out of the previous days in Step 3, criterion (2), currently suggested to be four;

(4)   The threshold for ice concentration in Step 3, criterion (2), currently suggested to be 80%.

(5)   Instead of the ice concentration history of the previous days, it is also possible to use the history of several brightness temperature swath files within the previous one or two days.

4.2   Further work

Preliminary study on other ice concentration retrieval algorithms has indicated that the artefact occurrence is only limited to some algorithms (Section 3.3.2). This motivates a thorough investigation of other popular algorithms and comparisons of their results with those from ASI and

Bootstrap algorithms, in order to identify any other occurrence of the artefact. The difference between the retrieved ice concentrations of various pairs of algorithms should be studied. Maps of ice concentration difference between two algorithms could be plotted. It is expected that algorithms would produce slightly different results among themselves, but these inter-algorithm variations should be consistent in time and in scale. Any sudden appearance of localized difference between algorithm indicates inconsistency which could potential be an artefact. In this proposed investigation one would look for such cases to identify other artefacts, and would carry out similar analyses as in this thesis to improve our understanding on the subject.

5　Conclusions

Accurate classification between ice and ocean and estimation of ice concentration are essential in climate studies for calculations on heat fluxes, gas exchange, ice formation, etc. This thesis consists of an investigation on an artefact of open water area observed on the ASI sea ice concentration maps during the studied period of February to April 2014, at a location where MODIS visual images show ice cover. Using a case-specific definition of a "box-to-frame" ratio, together with visual inspection, we can conclude that the studied episode in 2014 was the sole occurrence in the ASI AMSR-E/AMSR-2 data from 2002 to 2016, during which the ASI algorithm has been used to retrieve ice concentration from AMSR-E and AMSR-2 data. Bootstrap AMSR-E/AMSR-2 data shows the artefact during the studied period, and also shows underestimations of ice concentration during February to May 2013. Bootstrap SSM/I data from NSIDC shows the artefact during the studied period, but not in 2013; while NTA SSM/I and OSISAF SSM/I data do not show the artefact. Results from Bootstrap, NTA, and OSISAF algorithms shows underestimations with respect to that from the ASI algorithm and MODIS images. Further investigations are needed to understand such phenomenon. Analyses of brightness temperature, 2 metre temperature, snowfall, bathymetry, and wind were carried out to identify possible explanation for the occurrence of the artefact. It reveals that the Bootstrap filter and the gradient ratio GR(36.5/18.7) filter, used for weather filtering in the ASI algorithm, have created the artefact. During the studied period, we observe that GR(36.5/18.7) at the studied area has exceeded its threshold value at some pixels of the ASI ice concentration data, which leads to the pixel being set to 0% ice concentration. We also observe that throughout the studied period, the Bootstrap ice concentration was consistently low at the location of the artefact, which would also lead to the pixel being set to 0%. Moreover, we see that the location of the artefact correlates to the bathymetry of the region; and that the occurrence of the artefact, and its disappearance, are closely related to changes in air temperature, which suggests a linkage to surface melt-refreeze processes. We speculate that surface wetting could have led to the pixels being misinterpreted by the ASI algorithm as open water.

A basic correction of directly replacing the erroneous data points as a post-processing effort by switching of the Bootstrap filter and the GR(36.5/18.7) filter in the ASI algorithm at the corrupted pixels have been presented. This correction is essential for climate studies. For instance, if the uncorrected dataset is used for calculating ocean-to-air heat flux at the location of the artefact, the result for each erroneous open water pixel would be higher than when the corrected dataset is

used. A general method to detect and remove potential artefacts at other locations has been proposed, by comparing the present day ice concentration data with its history, with the assumption that a pixel with a history of relative high ice concentration (> 80%) within the ice pack should not change abruptly into an ice-free pixel within a day. Due to the limited time for this thesis, this method has not been implemented. Adjustments to certain variables used in the solution are needed upon implementation. Further investigation is needed to devise a complete solution to detect and correct other possible artefacts.

6 References

Abdalati, W. & Steffen, K. (1995). Passive microwave-derived snow melt regions on the Greenland Ice Sheet. *Geophys. Res. Lett.*, *22*(7), 787-790. http://dx.doi.org/10.1029/95gl00433

Allison, I., Brandt, R. E., & Warren, S. G. (1993). East Antarctic sea ice: Albedo, thickness distribution, and snow cover. *Journal of Geophysical Research: Oceans*, *98*(C7), 12417-12429.

Anderson, M. R. (1997). Determination of a melt-onset date for Arctic sea-ice regions using passive-microwave data. *Annals of Glaciology*, *25*, 382-387.

Arrigo, K. R., & van Dijken, G. L. (2003). Phytoplankton dynamics within 37 Antarctic coastal polynya systems. J. Geophys. Res., 108, 3271, doi:10.1029/2002JC001739.

Brucker, L., Cavalieri, D. J., Markus, T., & Ivanoff, A. (2014). NASA Team 2 sea ice concentration algorithm retrieval uncertainty. IEEE Transactions on Geoscience and Remote Sensing, 52(11), 7336-7352.

Cavalieri, D. J., Crawford, J. P., Drinkwater, M. R., Eppler, D. T., Farmer, L. D., Jentz, R. R., & Wackerman, C. C. (1991). Aircraft active and passive microwave validation of sea ice concentration from the Defense Meteorological Satellite Program Special Sensor Microwave Imager. *J. Geophys. Res,* 96(C12), 21989-22008.

Colbeck, S. C. (1982). An overview of seasonal snow metamorphism. *Rev. Geophys.*, *20*(1), 45. http://dx.doi.org/10.1029/rg020i001p00045

Colbeck, S. C. (1989). Snow-crystal growth with varying surface temperatures and radiation penetration. *J. Glaciol.*, 35(119), 23-29.

Comiso, J. C. (1995). SSM/I sea ice concentrations using the bootstrap algorithm (Vol. 1380). National Aeronautics and Space Administration, Goddard Space Flight Center.

Haas, C., Thomas, D., & Bareiss, J. (2001). Surface properties and processes of perennial Antarctic sea ice in summer. *Journal Of Glaciology*, *47*(159), 613-625. http://dx.doi.org/ 10.3189/172756501781831864

Comiso, J. C. (2000). updated 2015. Bootstrap Sea Ice Concentrations from Nimbus-7 SMMR and DMSP SSM/I-SSMIS, Version 2. Boulder, Colorado USA. NASA National Snow and Ice Data Center Distributed Active Archive Center. doi: http://dx.doi.org/10.5067/J6JQLS9EJ5HU. Accessed on 1 March 2016.

Comiso, J. C., Cavalieri, D. J., Parkinson, C. L., & Gloersen, P. (1997). Passive microwave algorithms for sea ice concentration: A comparison of two techniques. *Remote sensing of Environment,* 60(3), 357-384.
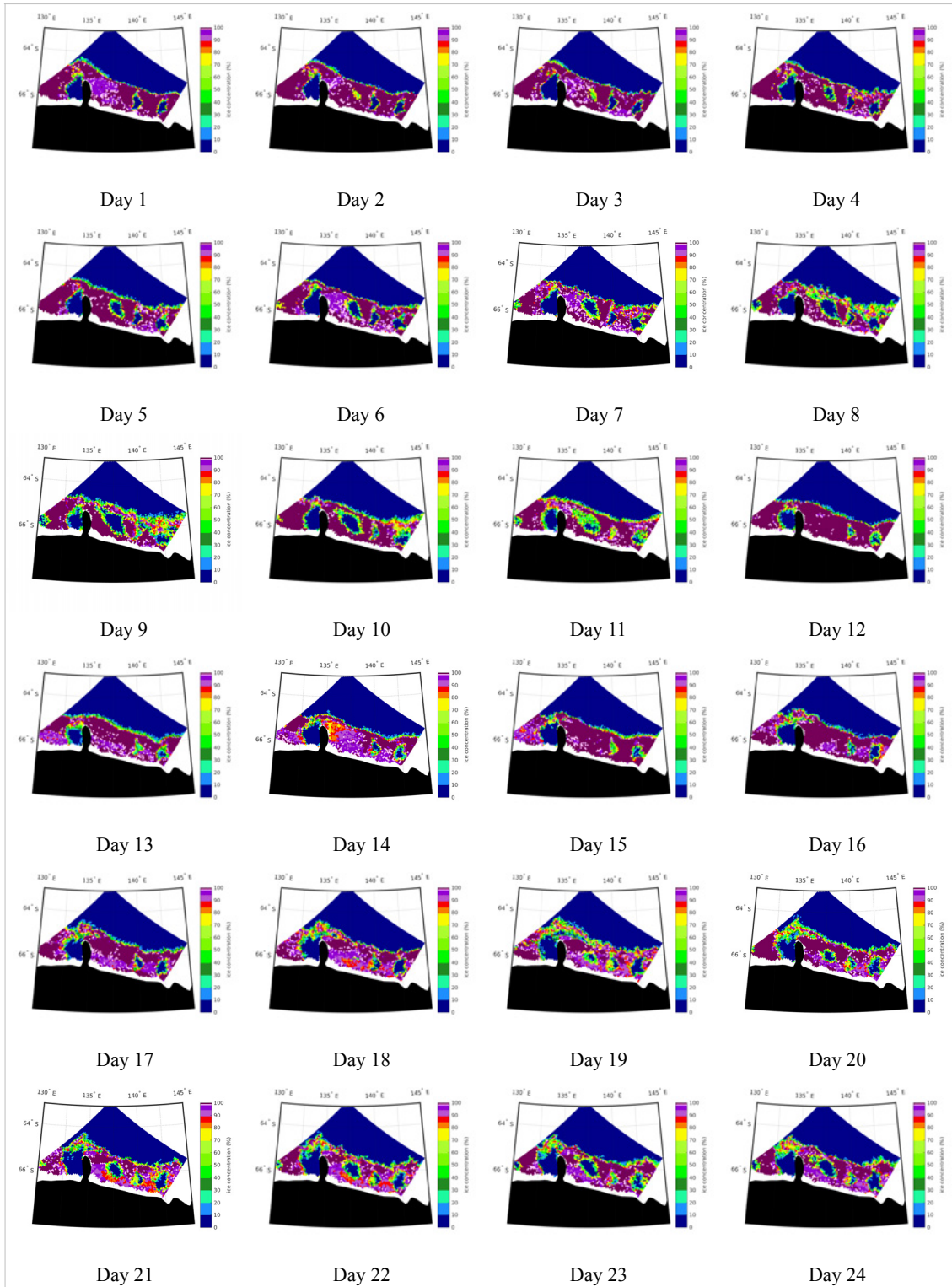
Fretwell, P., Pritchard, H. D., Vaughan, D. G., Bamber, J. L., Barrand, N. E., Bell, R., Bianchi, C., Bingham, R. G., Blankenship, D. D., Casassa, G., Catania, G., Callens, D., Conway, H., Cook, A. J., Corr, H. F. J., Damaske, D., Damm, V., Ferraccioli, F., Forsberg, R., Fujita, S., Gim, Y., Gogineni, P., Griggs, J. A., Hindmarsh, R. C. A., Holmlund, P., Holt, J. W., Jacobel, R. W., Jenkins, A., Jokat, W., Jordan, T., King, E. C., Kohler, J., Krabill, W., Riger-Kusk, M., Langley, K. A., Leitchenkov, G., Leuschen, C., Luyendyk, B. P., Matsuoka, K., Mouginot, J., Nitsche, F. O., Nogi, Y., Nost, O. A., Popov, S. V., Rignot, E., Rippin, D. M., Rivera, A., Roberts, J., Ross, N., Siegert, M. J., Smith, A. M., Steinhage, D., Studinger, M., Sun, B., Tinto, B. K., Welch, B. C., Wilson, D., Young, D. A., Xiangbin, C., and Zirizzotti, A. (2013). Bedmap2: improved ice bed, surface and thickness datasets for Antarctica, The Cryosphere, 7, 375-393, doi:10.5194/tc-7-375-2013

Gloersen, P., & D. J. Cavalieri, D. J. (1986). Reduction of weather effects in the calculation of sea ice concentration from microwave radiances. *J. Geophys. Res., 91*(C3), 3913–3919, doi:10.1029/JC091iC03p03913.

Grenfell, T. C. (1992). Surface−based passive microwave studies of multiyear sea ice. *Journal of Geophysical Research: Oceans*, *97*(C3), 3485-3501.

Ivanova, N., Johannessen, O. M., Pedersen, L. T., & Tonboe, R. T. (2014). Retrieval of Arctic sea ice parameters by satellite passive microwave sensors: A comparison of eleven sea ice concentration algorithms. *IEEE Transactions on Geoscience and Remote Sensing*, 52(11), 7233-7246.

Killworth, P. D., (1983). Deep convection in the World Ocean. Rev. Geophys., 21, 1–26, doi: 10.1029/RG021i001p00001.

Launiainen, J. & B. Cheng. (1998). Modelling of ice thermodynamics in natural water bodies. *Cold Reg. Sci.Technol.*, 27(3),153-178.

Markus, T., & Cavalieri, D. J. (1998). Snow depth distribution over sea ice in the Southern Ocean from satellite passive microwave data. *American Geophysical Union*, 19-39.

Markus, T., & Cavalieri, D. (2006). Interannual and regional variability of Southern Ocean snow on sea ice. *Annals Of Glaciology*, *44*(1), 53-57. http://dx.doi.org/10.3189/172756406781811475

MATLAB and Statistics Toolbox Release 2016a, The MathWorks, Inc., Natick, Massachusetts, United States.

Maykut, G. A. (1978). Energy exchange over young sea ice in the central Arctic. *J. Geophys. Res.*, *83*, 3646–3658.

Mätzler, C. (1994). Passive microwave signatures of landscapes in winter. *Meteorl. Atmos. Phys.*, 54(1-4), 241-260. doi:10.1007/bf01030063

Mätzler, C., Aebischer, H., & Schanda, E. (1984). Microwave dielectric properties of surface snow. *IEEE journal of oceanic engineering,* 9(5), 366-371.

Meissner, T., & Wentz, F. (2012).The emissivity of the ocean surface between 6 - 90 GHz over a large range of wind speeds and Earth incidence angles. *IEEE TGRS,* vol. 50(8), pp 3004.
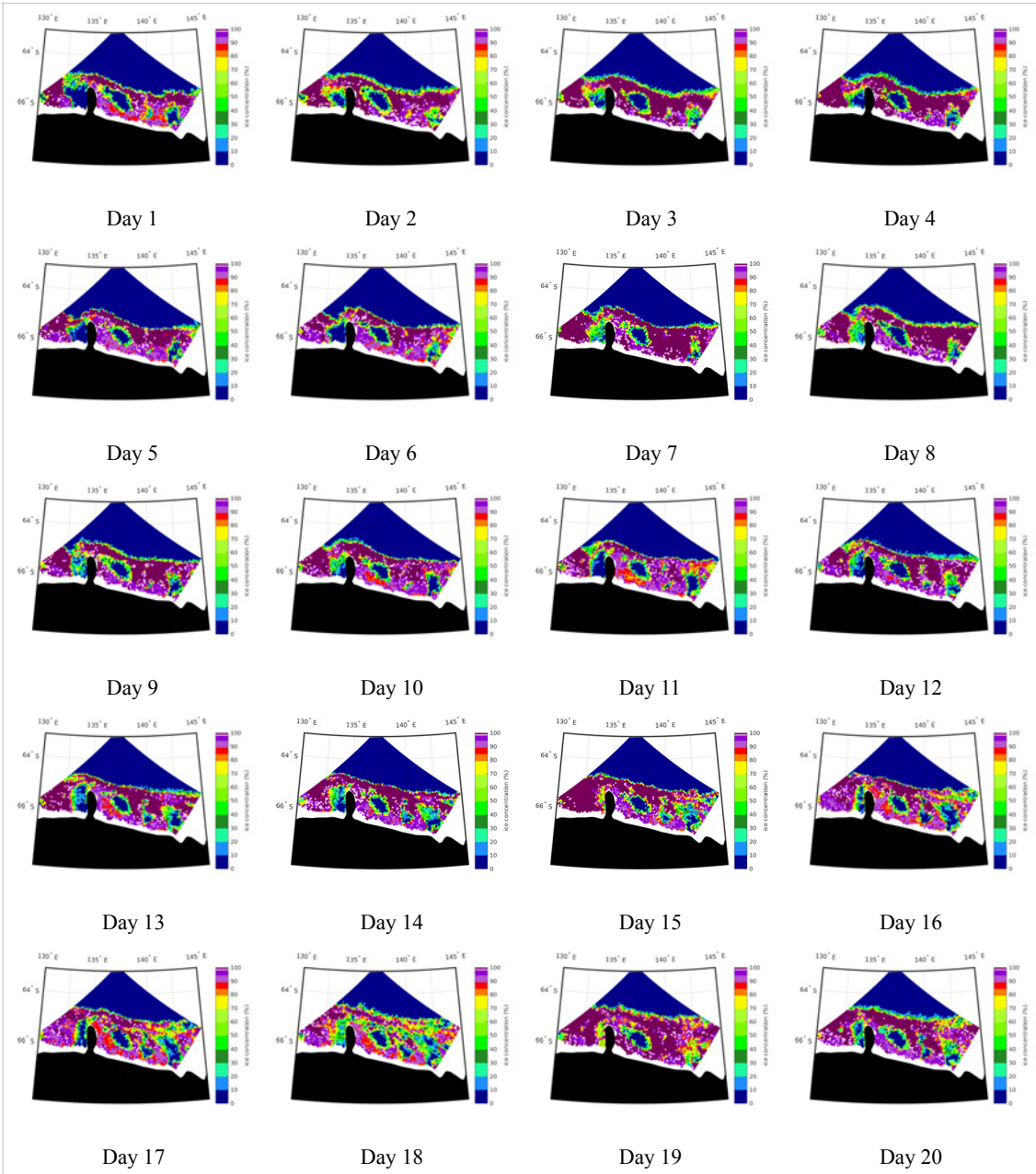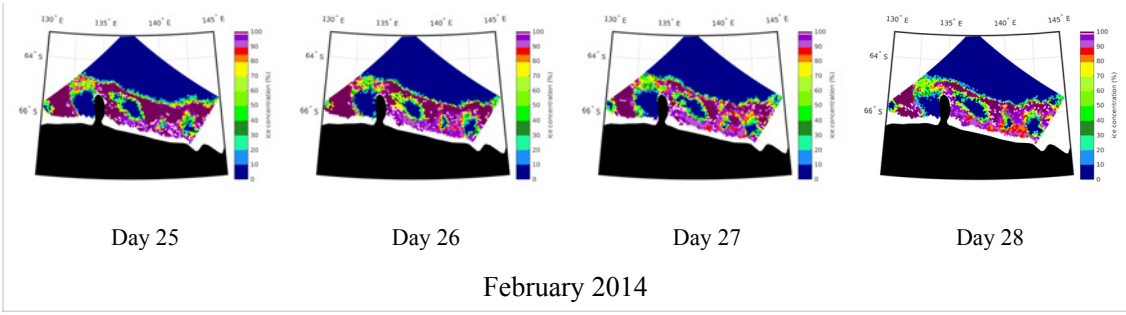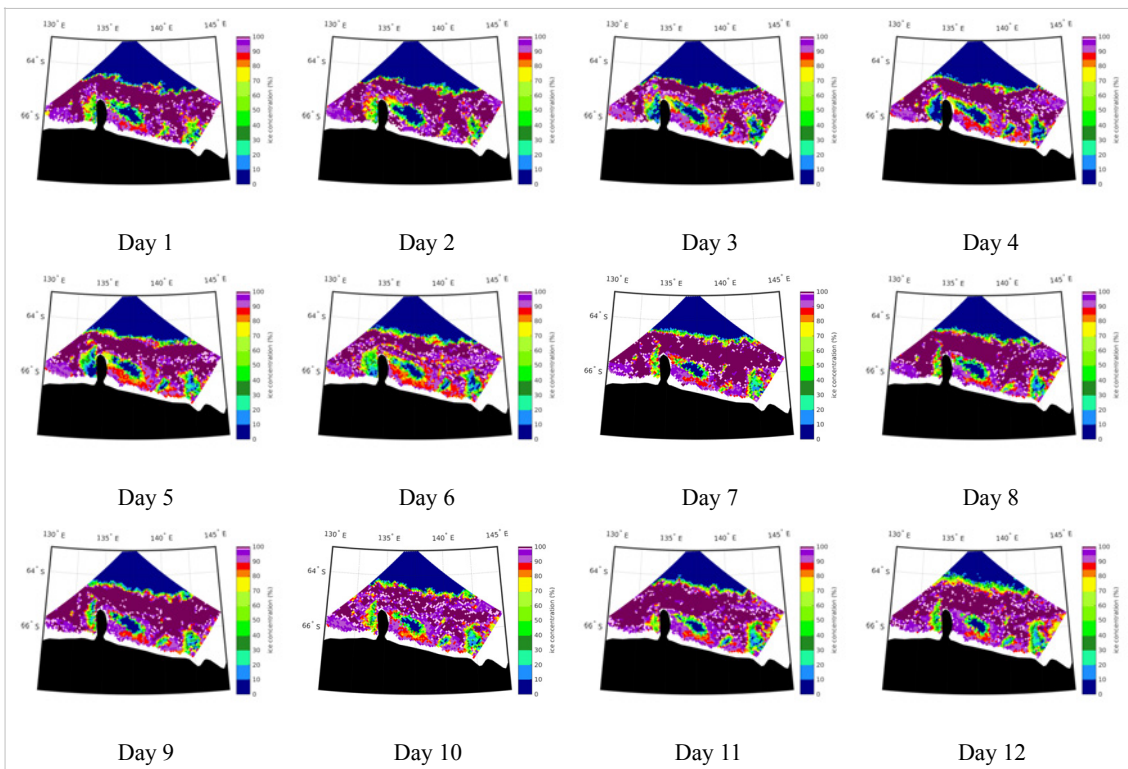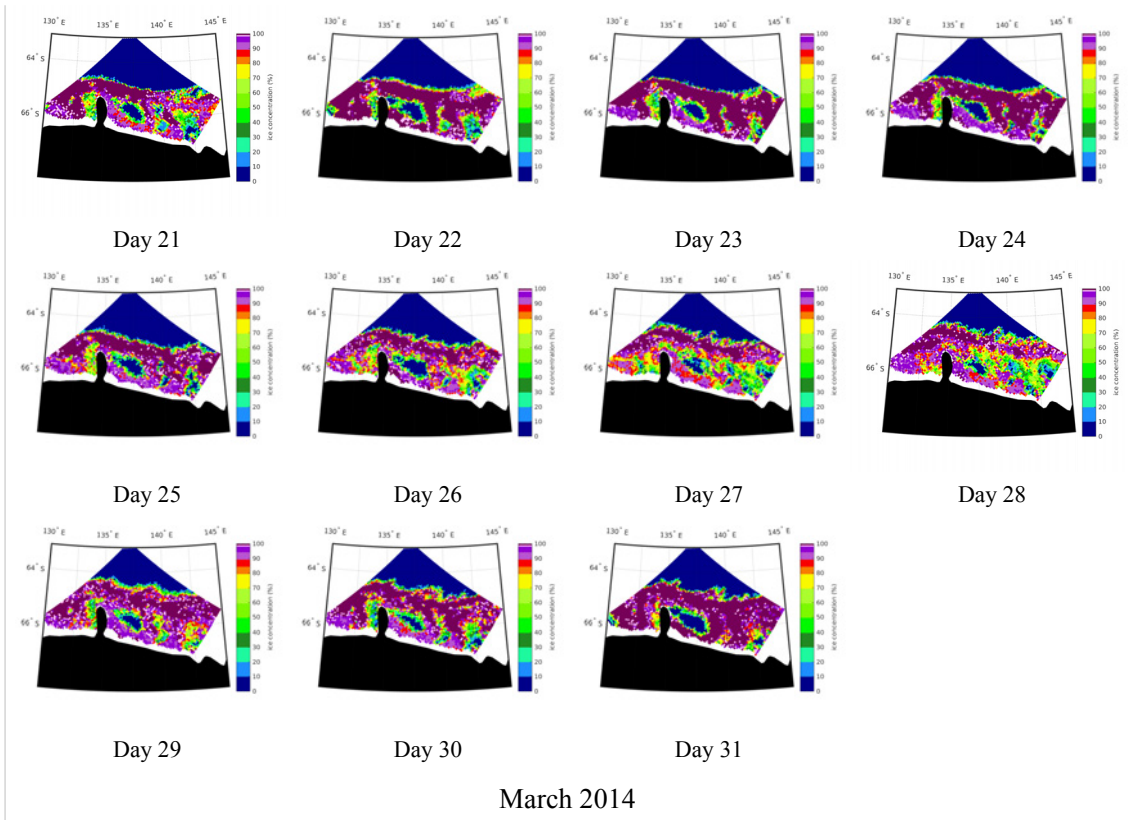
Miller, L. A., & DiTullio, G. R. (2007). Gas fluxes and dynamics in polynyas. Polynyas: Windows to the World's Oceans, W. O. Smith, Jr. and D. G. Barber, Eds., Elsevier, 163–191.

Nihashi, S., & Ohshima, K. I. (2015). Circumpolar mapping of Antarctic coastal polynyas and landfast sea ice: relationship and variability. Journal of climate, 28(9), 3650-3670.

Ohshima, K. I., Fukamachi, Y., Williams, G. D., Nihashi, S., Roquet, F., Kitade, Y., ... & Hindell, M. (2013). Antarctic Bottom Water production by intense sea-ice formation in the Cape Darnley polynya. Nature Geoscience, 6(3), 235-240.

Onstott, R. G., Grenfell, T. C., Matzler, C., Luther, C. A., & Svendsen, E. A. (1987). Evolution of microwave sea ice signatures during early summer and midsummer in the marginal ice zone. *J. Geophys. Res.,* 92(C7), 6825. doi:10.1029/jc092ic07p06825

Pomeroy, J. W., & Brun, E. (2001). Physical properties of snow. *Snow ecology: A interdisciplinary examination of snow-covered ecosystems*, 45-126.

Tamura, T., Ohshima, K. I., & Nihashi, S. (2008). Mapping of sea ice production for Antarctic coastal polynyas. Geophys. Res. Lett., 35, L07606, doi:10.1029/2007GL032903.

Tonboe, R., Lavelle, J., Pfeiffer, R. H., & Howe, E. (2016). Product User Manual for OSI SAF Global Sea Ice Concentration.

Untersteiner, N. (1968). Natural desalination and equilibrium salinity profile of perennial sea ice. Journal of Geophysical Research, 73(4), 1251-1257.

Wentz, F. J., & Meissner, T. (2000). Algorithm theoretical basis document (ATBD) version 2 AMSR ocean algorithm. RSS Tech. Proposal 121599A-1, Remote Sensing Systems, 59 pp.

Williams, G. D., Bindoff, N. L., Marsland, S. J., & Rintoul, S. R. (2008). Formation and export of dense shelf water from the Adélie Depression, East Antarctica. J. Geophys. Res., 113, C04039, doi:10.1029/2007JC004346.

WMO sea-ice nomenclature. (1971). *Journal Of Hydrology*, *14*(3-4), 354. http://dx.doi.org/ 10.1016/0022-1694(71)90048-5

Woodhouse, I. (2006). Introduction to microwave remote sensing (p. 59). Boca Raton: Taylor&Francis.

Worby, A. P. & Allison, I. (1991). Ocean-atmosphere energy exchange over thin, variablem concentration Antarctic pack ice. *Annals of Glaciology*, *15*(1), 184-190.

A   Appendix

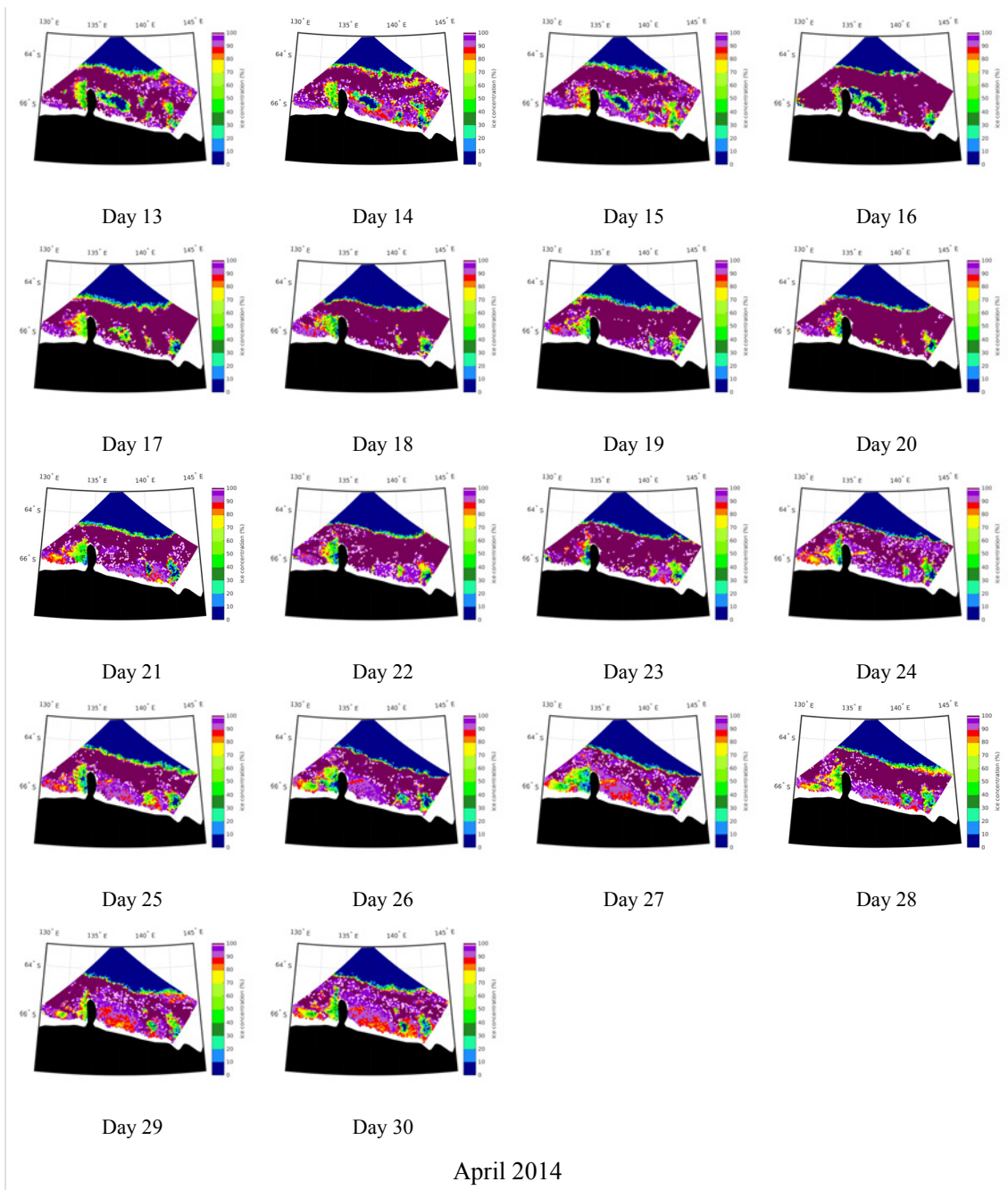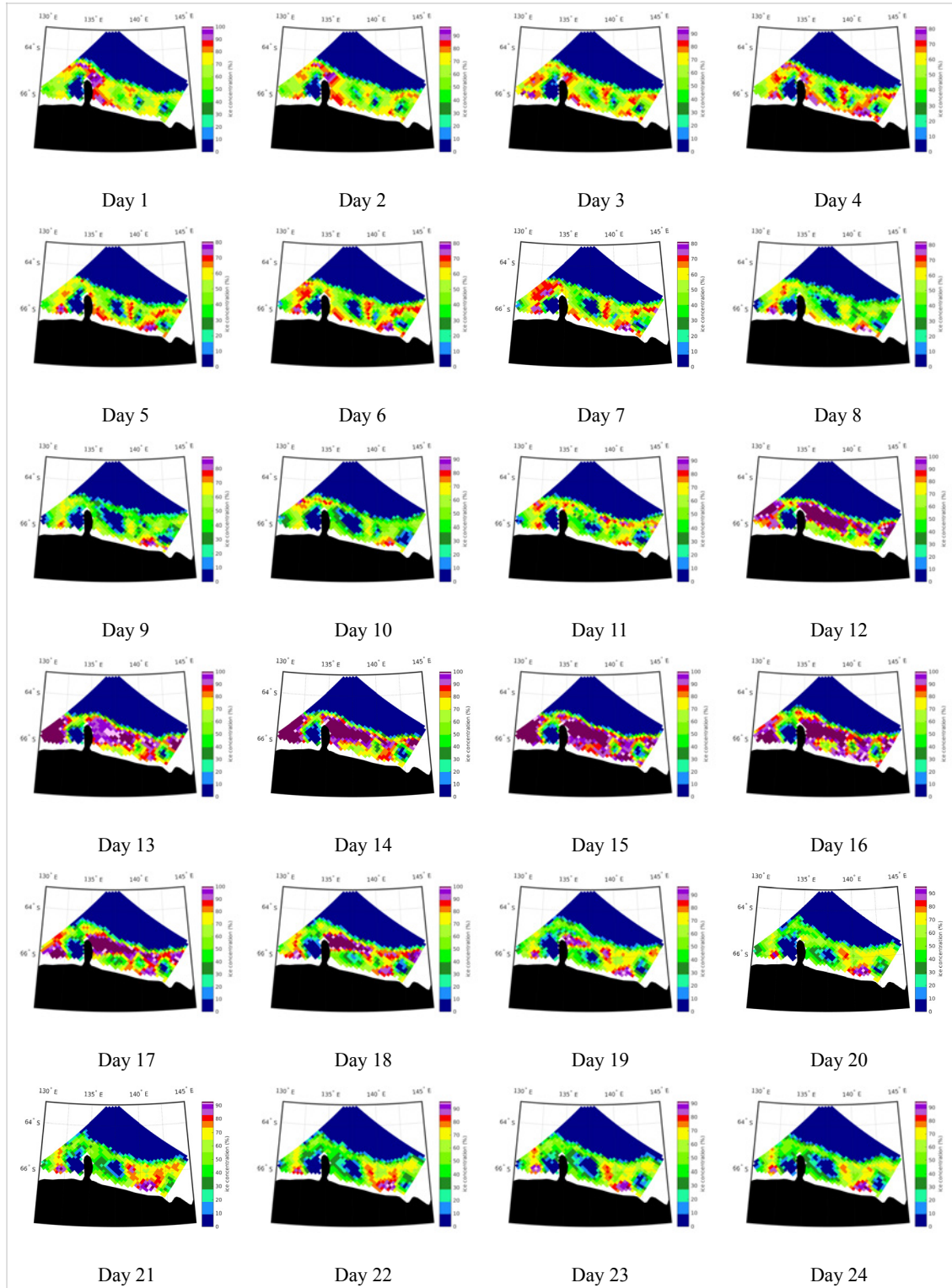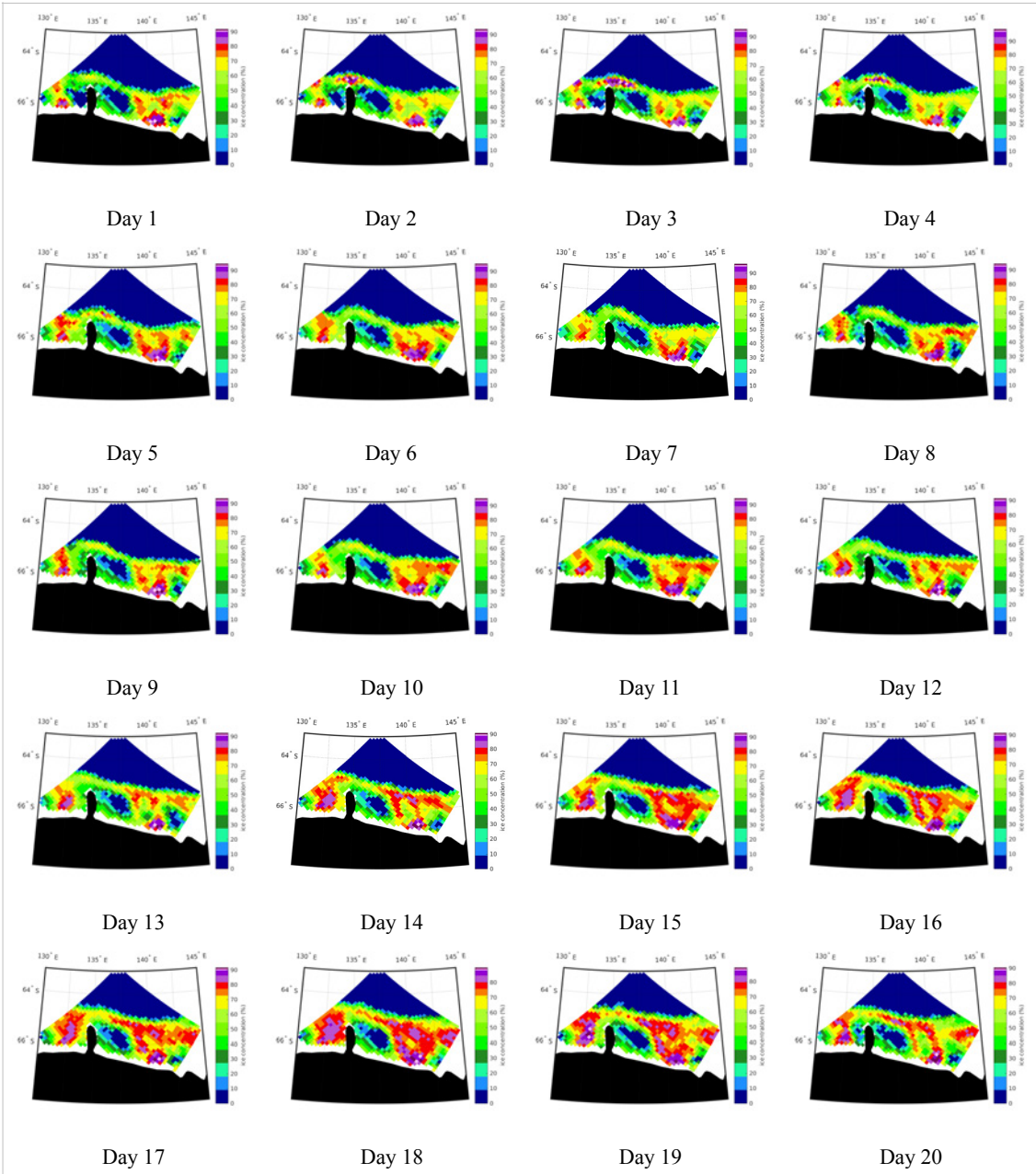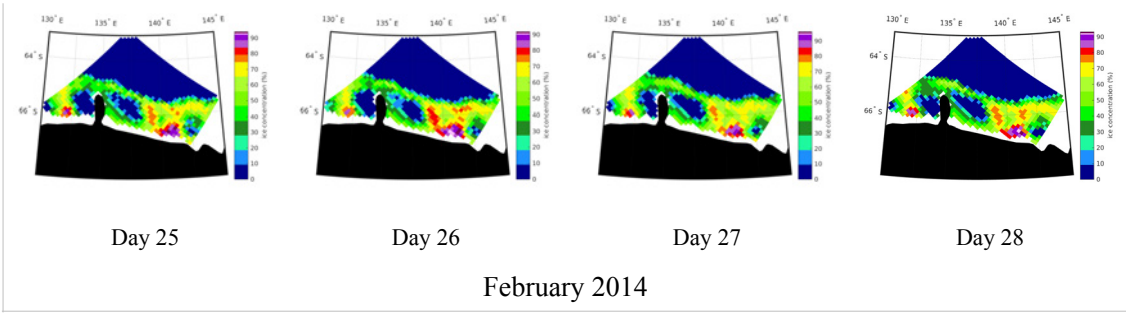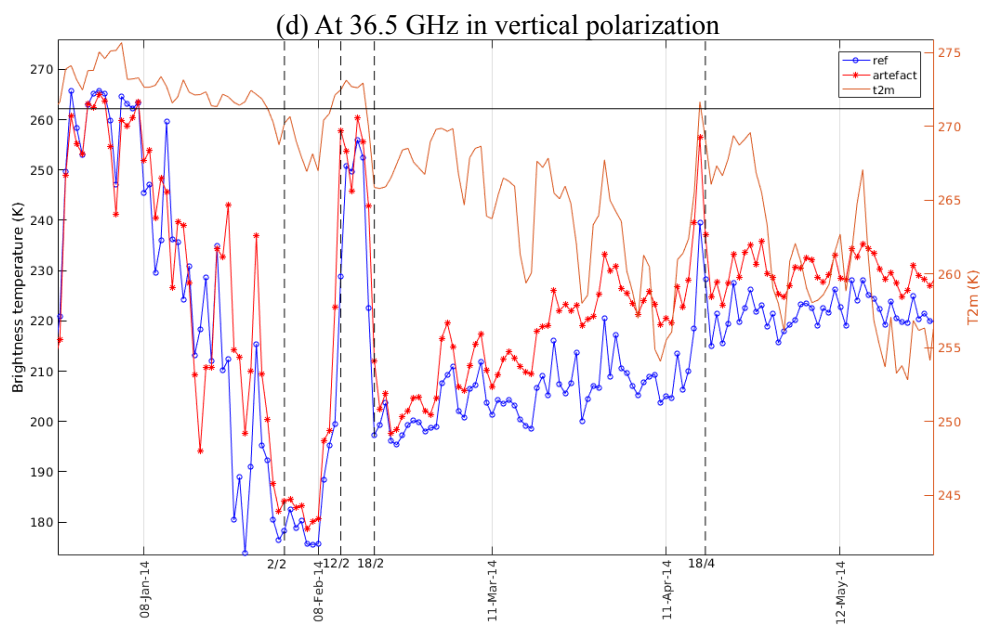## A.1   Daily ASI ice concentration maps from February to April 2014

Day 1   Day 2   Day 3   Day 4

Day 5   Day 6   Day 7   Day 8

Day 9   Day 10   Day 11   Day 12

Day 13   Day 14   Day 15   Day 16

Day 17   Day 18   Day 19   Day 20

Day 21   Day 22   Day 23   Day 24

Day 25   Day 26   Day 27   Day 28

February 2014

Day 1   Day 2   Day 3   Day 4

Day 5   Day 6   Day 7   Day 8

Day 9   Day 10   Day 11   Day 12

Day 13   Day 14   Day 15   Day 16

Day 17   Day 18   Day 19   Day 20

Day 21   Day 22   Day 23   Day 24

Day 25   Day 26   Day 27   Day 28

Day 29   Day 30   Day 31

March 2014

Day 1   Day 2   Day 3   Day 4

Day 5   Day 6   Day 7   Day 8

Day 9   Day 10   Day 11   Day 12

Day 13   Day 14   Day 15   Day 16

Day 17   Day 18   Day 19   Day 20

Day 21   Day 22   Day 23   Day 24

Day 25   Day 26   Day 27   Day 28

Day 29   Day 30

April 2014

Figure A.1   Daily ASI ice concentration maps from February to April 2014

A.2   Daily Bootstrap ice concentration maps from February to April 2014

Day 1	Day 2	Day 3	Day 4
Day 5	Day 6	Day 7	Day 8
Day 9	Day 10	Day 11	Day 12
Day 13	Day 14	Day 15	Day 16
Day 17	Day 18	Day 19	Day 20
Day 21	Day 22	Day 23	Day 24

Day 25   Day 26   Day 27   Day 28

February 2014

Day 1   Day 2   Day 3   Day 4

Day 5   Day 6   Day 7   Day 8

Day 9   Day 10   Day 11   Day 12

Day 13   Day 14   Day 15   Day 16

Day 17   Day 18   Day 19   Day 20

Day 21   Day 22   Day 23   Day 24

Day 25   Day 26   Day 27   Day 28

Day 29   Day 30   Day 31

March 2014

Day 1   Day 2   Day 3   Day 4

Day 5   Day 6   Day 7   Day 8

Day 9   Day 10   Day 11   Day 12

70

Day 13	Day 14	Day 15	Day 16
Day 17	Day 18	Day 19	Day 20
Day 21	Day 22	Day 23	Day 24
Day 25	Day 26	Day 27	Day 28
Day 29	Day 30		

April 2014

Figure A.2   Daily Bootstrap ice concentration maps from February to April 2014

A.3   Time series of AMSR-2 brightness temperatures

The average brightness temperature within the artefact and that within the reference area at each channels (18.7, 36.5, 89.0 Ghz) in both polarizations. On each graph, orange solid curve shows the 2 metre temperature at the location of the artefact and horizontal black solid line indicates the temperature of 271.2 K on the right axis.

(a) At 18.7 GHz in horizontal polarization

(b) At 18.7 GHz in vertical polarization

(c) At 36.5 GHz in horizontal polarization

(d) At 36.5 GHz in vertical polarization

73

(e) At 89.0 GHz in horizontal polarization

(f) At 89.0 GHz in vertical polarization
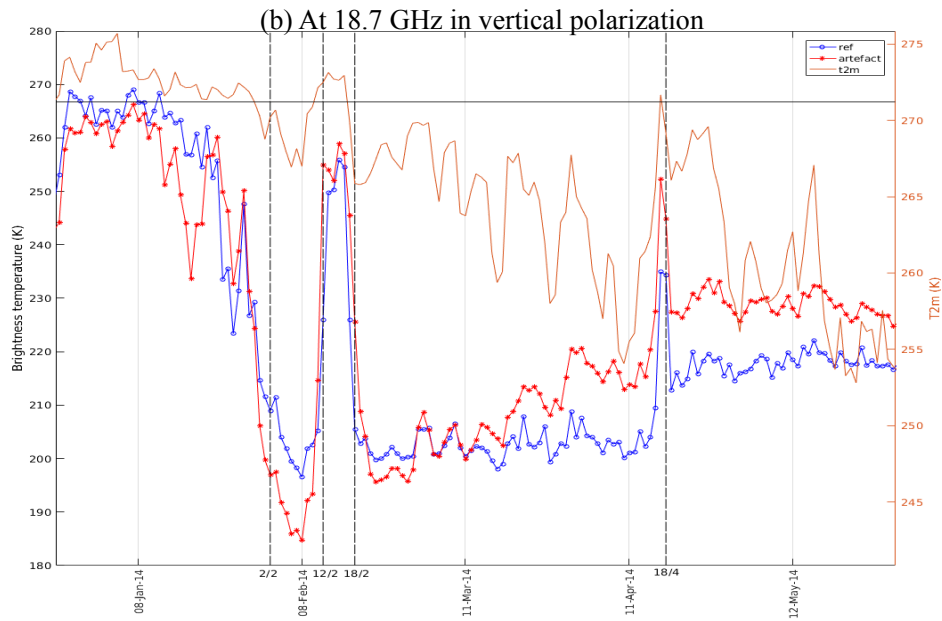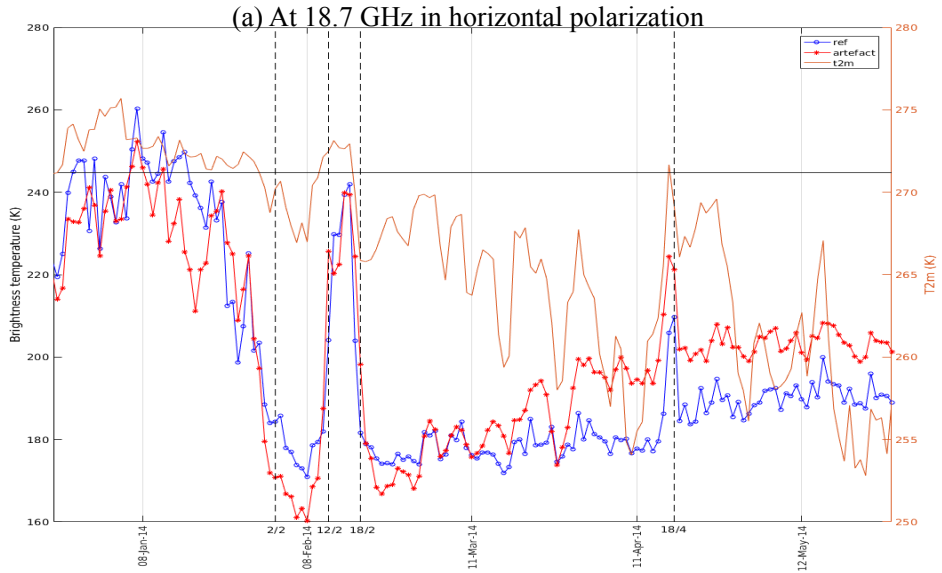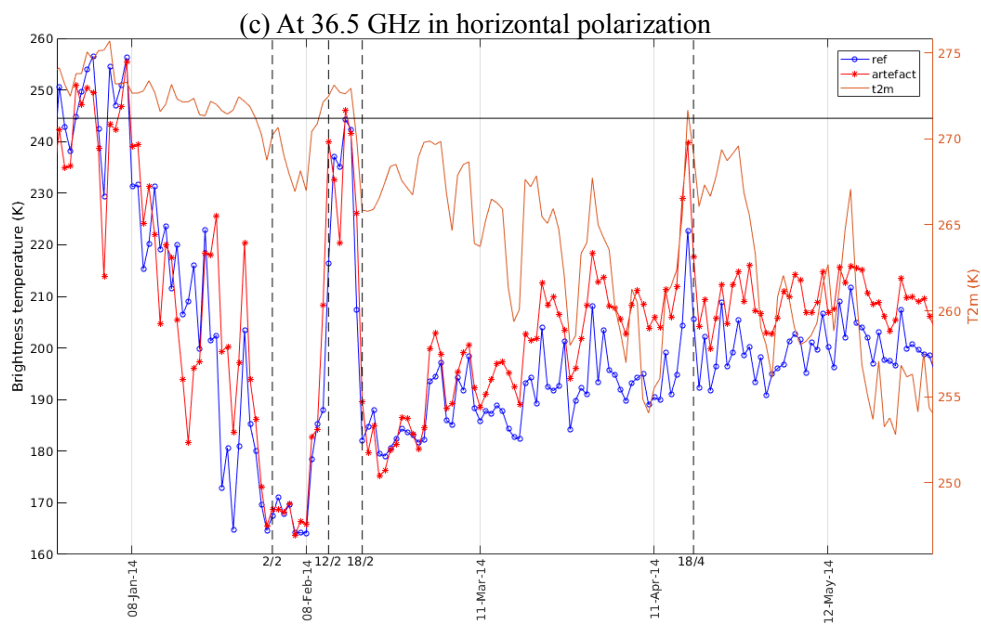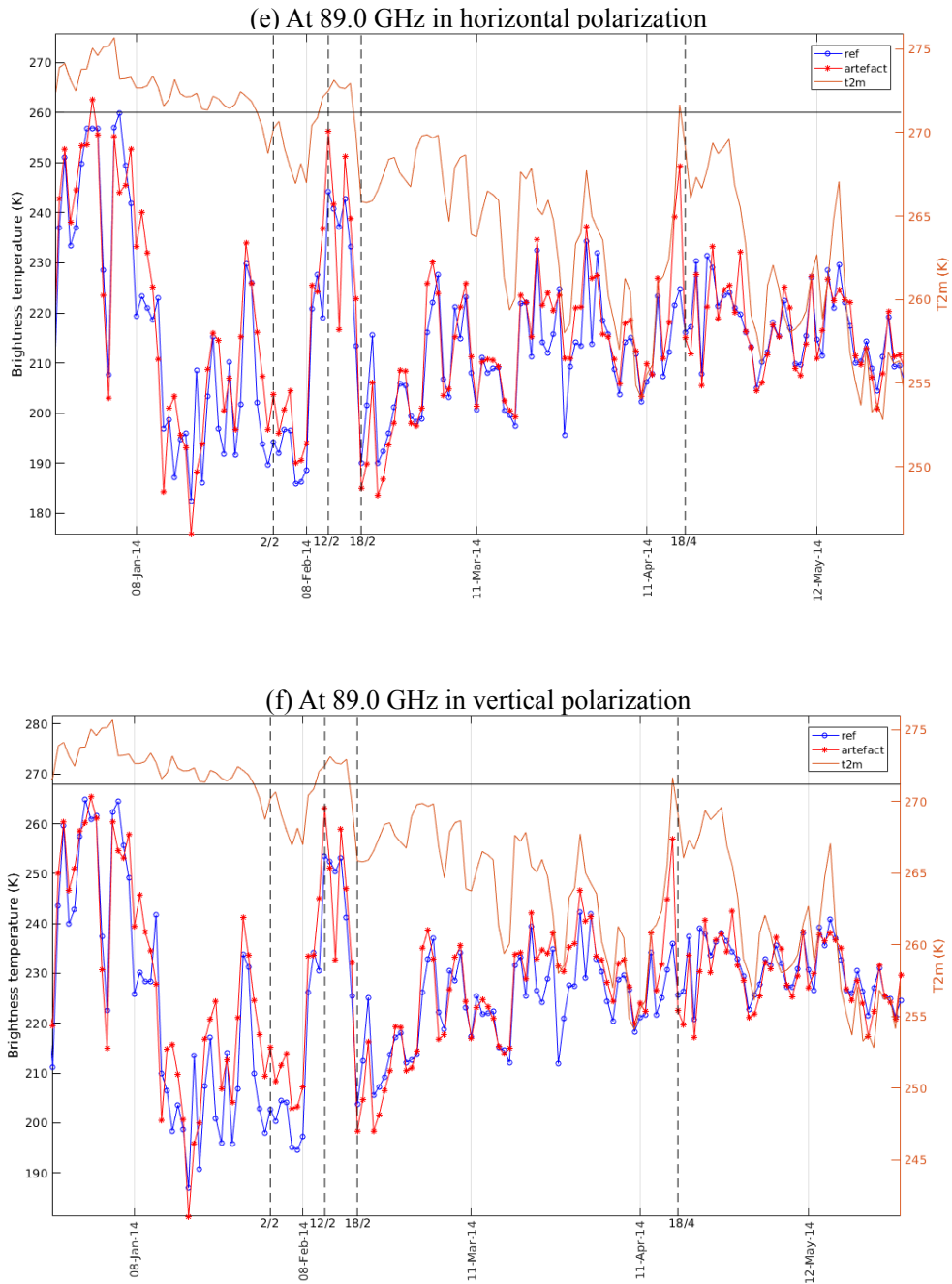
Figure A.3   Time series of AMSR-2 average brightness temperature within the artefact (blue circle) and within the reference area (red asterisks; location indicated in Figure 3.2) at 18.7, 36.5, and 89.0 GHz in horizontal and vertical polarization during January to May 2014.

List of Figures

List of Tables

List of abbreviations

AABW   Antarctic bottom water

AMSR-E   Advanced Microwave Scanning Radiometer for Earth Observing System

AMSR-2   Advanced Microwave Scanning Radiometer 2

ARTIST   Arctic Radiation and Turbulence Interaction Study

ASI   ARTIST Sea Ice (algorithm)

DMSP   Defense Meteorological Satellite Program

ECMWF   European Centre for Medium-Range Weather Forecasts

ERA   ECMWF Reanalysis

GCOM-W1   Global Change Observation Mission-Water

GR   Gradient ratio

IUP   Institute of Environmental Physics, University of Bremen

MODIS   Moderate Resolution Imaging Spectrometer

NASA   National Aeronautics and Space Administration

NSIDC   National Snow and Ice Data Center

NTA   NASA Team Algorithm

OSISAF   Ocean and Sea Ice Satellite Application Facility

SMMR   Scanning Multichannel Microwave Radiometer

SSM/I   Special Sensor Microwave Imager

SVA   Svendsen et al. algorithm

T2m   2 metre temperature

UTC   Coordinated Universal Time

WMO   World Meteorological Organization

Acknowledgement

THE PRESENT RESEARCH WORK HAS BEEN (PREPARED TO BE) PUBLISHED IN:

....
....
....
....
....